

Composition and Interface Engineering of Organic-Inorganic Hybrid Perovskites to Improve Photovoltaic Performance and Stability

THÈSE N° 9071 (2018)

PRÉSENTÉE LE 30 NOVEMBRE 2018

À LA FACULTÉ DES SCIENCES DE BASE

LABORATOIRE DE PHOTONIQUE ET INTERFACES

PROGRAMME DOCTORAL EN CHIMIE ET GÉNIE CHIMIQUE

ÉCOLE POLYTECHNIQUE FÉDÉRALE DE LAUSANNE

POUR L'OBTENTION DU GRADE DE DOCTEUR ÈS SCIENCES

PAR

Kyung Taek CHO

acceptée sur proposition du jury:

Prof. P. J. Dyson, président du jury
Prof. M. K. Nazeeruddin, Prof. M. Graetzel, directeurs de thèse
Prof. E. Palomares, rapporteur
Prof. S. Ahmad, rapporteur
Prof. M. CHERGUI, rapporteur



ÉCOLE POLYTECHNIQUE
FÉDÉRALE DE LAUSANNE

Suisse
2018

Thesis Abstract

Faced with the growing demands for energy in modern society, organic-inorganic metal halide perovskite materials have recently fascinated the photovoltaics (PV) research community due to a combination of their high quality optoelectronic properties and their ease in the fabrication proceed. As a result, solar cells employing the perovskite materials have been researched exponentially on their way and now the power conversion efficiency (PCE) of perovskite solar cells have been improved over 23% since the first report showing the PCE of 3% in 2009.

In this thesis, I investigate compositional modification of perovskite materials and optimization of the charge transporting materials to produce high efficiency, stable and reproducible perovskite solar cells. First of all, after the reasonable performance was achieved, we have innovated a new approach of interface engineering in a perovskite layer to boost efficiency of devices. Engineering a compositional gradient with formamidinium bromide (FABr) at the rear interface between a pristine mixed perovskite ((FAPbI₃)_{0.85}(MAPbBr₃)_{0.15}) film and a hole transporting material (spiro-OMeTAD) demonstrated that charge collection is improved and charge recombination is reduced at the interface, which leads to a striking enhancement in open-circuit voltage (V_{OC}). This result shed light on the importance of the passivation engineering on the rear surface of perovskite layers.

However, beyond the improvement of efficiency, a long-term stability under moisture and continuous illumination is still remained as another challenge for market deployment of the perovskite solar cells. To develop the stability, we have developed the engineering by the surface growth of a two-dimensional (2D) perovskite, the crystal structure of A_2BX_4 , on top of a bulk three-dimensional (3D) perovskite ABX_3 film. It is well-known that the 2D perovskite has the superior stability, but suffered because of their low efficiency in the application of photovoltaics. The formation of a distinct 2D perovskite on top of the 3D perovskite ($CS_{0.1}FA_{0.74}MA_{0.13}PbI_{2.48}Br_{0.39}$) layer was proved by investigation of structural and optical properties of the stack. This embodying two different type of perovskite layer in one film had never been shown. Finally, this innovative approach led to the PCE of 21% and enhanced stability sustaining 85% of the initial value after 800 hours under full illumination. Thus, my approach of coating 2D perovskite layer make the perovskite solar cells more effective and stable for commercialization.

Besides, to avoid the toxic chemical the lead free perovskite ($CS_2AgBiBr_6$) was explored as photovoltaics and the further improvement can be expected. The last results presented in this thesis are related to optimization of the electron transporting layer (ETL) and hole-transporting materials

(HTM) for efficient perovskite solar cells. It is shown that the ETL and the HTMs are playing a significant role in realizing efficient and stable perovskite solar cells.

Keywords

Perovskites

Solar cell

Optimization

Spin-coating

Anti-solvent dripping

Sequential step method.

Mixed perovskite

Passivation

Gradient perovskite

Open circuit voltage

Power conversion efficiency

Low dimensional perovskite

Stability

Lead-free perovskite

Hole transporting materials

Metal oxide conductive layer

Résumé de la Thèse

Face à la demande croissante d'énergie dans la société moderne, les matériaux à base de pérovskite composés d'halogénures métalliques organiques et inorganiques ont récemment fasciné la communauté de la recherche photovoltaïque (PV) en raison de la combinaison de leurs propriétés optoélectroniques de haute qualité et de leur facilité de fabrication. En conséquence, les cellules solaires utilisant les matériaux à base de pérovskite ont fait l'objet de recherches exponentielles. Aujourd'hui, l'efficacité de conversion de la puissance des cellules solaires à pérovskite a été améliorée de plus de 23% depuis le premier rapport montrant une efficacité de 3% en 2009.

Dans cette thèse, j'étudie la modification de la composition des matériaux à base de pérovskite et l'optimisation des matériaux de transport de charge afin de produire des cellules solaires à haute efficacité, stables et reproductibles. Tout d'abord, une fois que les performances raisonnables ont été atteintes, nous avons innové une nouvelle approche d'ingénierie d'interface dans une couche de pérovskite afin de renforcer l'efficacité des périphériques. L'ingénierie d'un gradient de composition avec du bromure de formamidinium (FABr) à l'interface arrière entre une pérovskite mélangée immaculée ((FAPbI₃)_{0.85}(MAPbBr₃)_{0.15}) et un matériau de transport de trous (spiro-OMeTAD) a démontré que la collecte de charge est améliorée et que la recombinaison de charge est améliorée. Réduit à l'interface, ce qui conduit à une amélioration frappante de la tension en circuit ouvert (V_{OC}). Ce résultat a mis en lumière l'importance de l'ingénierie de passivation sur la surface arrière des couches de pérovskite.

Toutefois, au-delà de l'amélioration de l'efficacité, il reste encore une stabilité à long terme sous l'humidité et un éclairage continu, constituant un autre défi pour le déploiement sur le marché des cellules solaires à pérovskite. Pour développer la stabilité, nous avons développé l'ingénierie par croissance en surface d'un pérovskite à deux dimensions (2D), la structure cristalline de A_2BX_4 , par-dessus un film en vrac ABX_3 à trois dimensions (3D) de pérovskite. Il est bien connu que la pérovskite 2D possède une stabilité supérieure, mais souffre de son faible rendement dans l'application de la photovoltaïque. La formation d'une pérovskite 2D distincte au-dessus de la couche de pérovskite 3D (Cs_{0.1}FA_{0.74}MA_{0.13}PbI_{2.48}Br_{0.39}) a été prouvée par l'étude des propriétés structurales et optiques de l'empilement. Cette incarnation de deux types différents de couche de pérovskite dans un film n'avait jamais été montrée. Enfin, cette approche innovante a permis d'obtenir une PCE de 21% et une stabilité accrue, maintenant 85% de la valeur initiale après 800 heures sous pleine illumination. Ainsi, mon approche de revêtement de la couche de pérovskite 2D rend les cellules

solaires à pérovskite plus efficaces et plus stables pour la commercialisation.

En outre, pour éviter les produits chimiques toxiques, la pérovskite sans plomb ($\text{Cs}_2\text{AgBiBr}_6$) a été explorée sous forme photovoltaïque et une amélioration supplémentaire est à prévoir. Les derniers résultats présentés dans cette thèse concernent l'optimisation de la couche de transport d'électrons (ETL) et des matériaux de transport de trous (HTM) pour des cellules solaires à pérovskite efficaces. Il est démontré que les ETL et les HTM jouent un rôle important dans la réalisation de cellules solaires pérovskites efficaces et stables.

Mots clés

Perovskites

Photovoltaïque

Optimisation

Spin-coating

Gouttes anti-solvant

Méthode par étapes séquentielles.

Pérovskite mixte

Passivation

Perovskite pente

Tension en circuit ouvert

Efficacité de conversion de puissance

Perovskite de bas dimension

La stabilité

Pérovskite sans plomb

Matériel de transport de trou

Couche conductrice d'oxyde métallique

Acknowledgement

First of all, I appreciate my thesis director, Prof. Mohammad Khaja Nazeeruddin and co-director, Prof. Michael Grätzel, allowing me to perform researching and get valuable experience in EPFL (École Polytechnique Fédérale de Lausanne).

Prof. Mohammad Khaja Nazeeruddin

I would like to thank you for your continued encouragements, scientific guidance, your patience and your thrust. You gave me total freedom in choosing my research topic and waited with your trust. I am deeply grateful for that and I think I can do all of the work owing to that. It is a real pleasure to study under you!

Prof. Michael Grätzel

I also thank you for serving as my thesis co-advisor, Prof. Michael Grätzel. It is an honor to study with you because you are a very eminent scientist and you always welcome me whenever I visit you.

Dr. Sanghyun Paek.

You are my super-affinity and dearest collaborator. Thanks for your scientific collaboration and support. And of course, our work and publications have not been accomplished without you.

Dr. Yonghui Lee.

I would like to thank for your help in having been my experimental coach. I could obtain results with your feedback.

Dr. Giulia Grancini

Thanks for all your scientific advices and for all the great moments we spent together. I am really thank you for helping me.

Dr. Cristina Roldán-Carmona, Dr. Paul Gratia, Dr. Kasparas Rakstys, and Dr. Sadig Aghazada, and Dr. Zimmermann Iwan

Thanks for great helps from starting time in Sion. It was such a good time for discussions, scientific support, many laughs and fun activities.

Géraldine Gfeller

Thank you a lot for all the administrative assistance and your kindness .

Humphry-baker Robin

I acknowledge your technical help about technical supporting and expertise.

Manuel Tschumi

Thanks for your technical help about laboratory facilities. I hope you feel better soon.

Dr. Emad Oveisi

Thanks for assistance and introduction into X-ray diffraction

Prof. Hyo Joong Lee

Thanks for many advices and kind words for a year of your visit.

Stephane Voeffray and Robin Deleze

I would like to thank you for your helps and implementing my many asks.

Laurent Seydoux and Annabelle Coquoz

I acknowledge you from the chemical store.

Dr. Pascal Alexander Schouwink

Thanks for assistance and introduction into X-ray diffraction

Heidi Francelet and Anne Lene Odegaard

I would like to thank for helpful administrative assistance.

Dr. Hobeom Kim and Dr. Heena Yang

Thanks you for all our fun evenings in Sion and for being a great friend.

Dr. Gain Kim and other Korean colleagues

Thanks for being such a nice friend, always present and willing to spend time even when you are tired of me.

Garcia Benito Inés, Huckaba Aron Joel, Kanda Hiroyuki, Abuhelaiqa Mousa Abdulla, Drigo Nikita, Fedorovskiy Alexander, Igei Cansu, Klipfel Nadja Isabelle Desiree, Queloz Valentin Ianis Emmanuel, Sutanto Albertus Adrian, Shirzadi Erfan, Xia Rui, and Prof. Peng Gao, Dr. Zhang Yi

I sincerely acknowledge my colleagues in GMF for having a great fun time and nice atmosphere in the lab and office. I also would like to thank for your cooperation and support. In particular, I keep in mind your welcome and having nice dinners with you.

My family (Chin Suk Cho, Hyang Ran Yoo and Hai Jin Cho) and friends.

I would also like to acknowledge my parents for their strong support and thanks for being my amazing fiends, specially Jaehoon Ryu, throughout the duration of my PhD studies.

My thesis committee members

I would like to thank you for having accepted to review my thesis. I would be pleasure to your valuable feedback.

All my collaborators and my co-authors

Thanks for your help, your scientific advices, and your collaboration.

To me.

Finally, I am here at this moment. During PhD life, I was thinking all will be well if I work hard and bright future will come if I graduate with many papers. As a result, I am quite proud of me and my products. I am done well. Now I am not sure what I will do and which way I will choose on my future. I don't think this way of researching forever is the best I can. But, don't be scare and worry. I can do well whatever I decide to do, if I do like I did in PhD course.

From Kyung Taek Cho.

A handwritten signature in black ink, enclosed within a circular scribble. The signature appears to be 'K. Cho'.

Sion, Switzerland

August 2018

Table of Contents

Thesis Abstract	3
Résumé de la Thèse	5
Acknowledgement	7
List of Figures	17
List of Tables	21
Chapter 1. Introduction	23
1.1. Introduction of perovskite	24
1.2. Photovoltaics	28
1.3. History and kinds of solar cells	37
1.4. Photovoltaics with perovskites	41
1.5. Conclusions and outlook	42
Chapter 2. Fabrication of PSCs	43
2.1. Introduction	44
2.2. Construction of complete perovskite solar cell	45
2.3. Optimization of each part	46
2.4. Conclusion	54
2.5. Outline of next chapters	55
Chapter 3. FABr passivation	57
3.1. Abstract	58
3.2. Introduction	58
3.3. Results and Discussion	59
3.4. Conclusion	70
3.5. Experimental section	70
Chapter 4. PEAI Passivation	73
4.1. Abstract	74

4.2. Introduction	74
4.3. Results and discussion	75
4.4. Conclusions	88
4.5. Experimental methods.....	89
Chapter 5. Lead-Free Perovskite.....	93
5.1. Abstract.....	94
5.2. Introduction	94
5.3. Results and discussion	96
5.4. Conclusion	103
5.5. Experimental section.....	104
Chapter 6. HTMs Investigation I.....	107
6.1. Abstract.....	108
6.2. Introduction	108
6.3. Results and discussion	109
6.4. Conclusions	114
6.5. Experimental method and Charaterization.....	114
Chapter 7. HTMs Investigation II.....	117
7.1. Abstract.....	118
7.2. Introduction	118
7.3. Results and Discussion	119
7.4. Conclusion	130
7.5. Experimental section.....	130
Chapter 8. ETL Investigation	133
8.1. Abstract.....	134
8.2. Introduction	134
8.3. Results and discussion.....	135

8.4. Conclusion	141
8.5. Experimental Section	142
Chapter 9. Conclusion	145
Reference	149
Curriculum Vitae	159

List of Figures

Figure 1.	Scheme of perovskite structure for different section	26
Figure 2.	Illustration of sphere model in ideal cubic perovskite.	26
Figure 3.	The formation of bonding orbital and anti-bonding orbital from two H atom orbitals and the splitting of an energy state	30
Figure 4.	Schematic about the splitting of the atoms and an example of conduction band valence band, and the band gap.	30
Figure 5.	An energy diagram of band structure.	30
Figure 6.	A simplified two dimensional intrinsic Si crystal structure.	32
Figure 7.	Band diagram of an intrinsic and extrinsic Si	33
Figure 8.	A simple electrons and holes model in p-n junction.	33
Figure 9.	Sun light spectrum and energy diagram in p-n junction diode	36
Figure 10.	p-n diode under forward bias and under reverse bias	36
Figure 11.	p-n diode under illumination.	36
Figure 12.	Illustrations of the three perovskite solar cells architectures.	44
Figure 13.	Scanning electron microscopy (SEM) images of compact TiO ₂ layer surface.	48
Figure 14.	J-V curves depending on the thickness of mesoporous TiO ₂ layer.	48
Figure 15.	Sequential (two-step) spin-coating procedure.	52
Figure 16.	SEM images of top surface of perovskite films by using one step process.	52
Figure 17.	One step processing by solvent engineering.	52
Figure 18.	Schematic and energy diagram of a passivated perovskite solar cell.	60
Figure 19.	Estimated bandgap edge position of various perovskites.	60
Figure 20.	Illustration of a method and change of morphology	62
Figure 21.	Cross-sectional SEM images of the complete perovskite solar cells.	62

Figure 22.	<i>J-V</i> curves and IPCE of as-prepared and passivated PSCs.	62
Figure 23.	Stability of J_{SC} , V_{OC} , FF and PCE and XRD analysis of pristine and passivated.	64
Figure 24.	Cross-sectional SEM images and corresponding EDX mapping images	64
Figure 25.	Energy dispersive X-ray spectroscopy (EDS) spectra of perovskite films.	65
Figure 26.	Optics spectra of perovskite films.	66
Figure 27.	Photo-physical properties and photovoltaic performance with simple mixing method.	68
Figure 28.	XRD patterns and photovoltaic performance of the perovskite films.	69
Figure 29.	Characterization of CFMPIB, L-CFM/P, and PEA_2PbI_4 perovskite.	76
Figure 30.	XRD comparison by the heating time on L-CFM/P.	76
Figure 31.	XRD spectra of a CFMPIB+PEAI perovskite film by simple mixing.	77
Figure 32.	Comparison of photoluminescence emission spectra of CFMPIB and L-CFM/P perovskites.	79
Figure 33.	Steady-state PL spectra of CFMPIB, L-CFM/P, and PEA_2PbI_4 perovskite films	79
Figure 34.	XRD measurement at fixed incident X-ray angle of 0.3° , 2° , and 5°	80
Figure 35.	Morphologies of the perovskite film and PSCs with CFMPIB and L-CFM/P.	81
Figure 36.	Comparison on roughness of perovskite films from typical AFM measurement.	81
Figure 37.	Cross-sectional SEM images of the complete devices fabricated with CFMPIB and L-CFM/P.	82
Figure 38.	Energy level diagram and photovoltaic performance of PSCs with CFMPIB and L-CFM/P	83
Figure 39.	Open circuit impedance spectra with clear differences toward the low frequency range	83
Figure 40.	Time-resolved PL decays of CFMPIB and L-CFM/P perovskite films at different excitation densities from 10^{15} to 10^{17} carriers/cm ³ .	85
Figure 41.	Time integrated Photoluminescence signal for the two perovskite as indicated in the legend as a function of the injected carrier density.	86
Figure 42.	IPCE spectrums and integrated J_{SC} from IPCE.	86
Figure 43.	Statistics of V_{OC} , J_{SC} , FF, and PCE of devices	86
Figure 44.	<i>J-V</i> curves of devices based on SnO ₂ with CFMPIB and L-CFM/P perovskite	87

Figure 45.	Dark storage stability of devices with CFMPIB and L-CFM/P. All of cells are stored in dark and measured in ambient atmosphere.	87
Figure 46.	PCE tracking from J-V measurement for 300 h of unencapsulated devices	88
Figure 47.	J-V curve of a homogeneous perovskite mixture of CFMPIB+PEAI device	88
Figure 48.	Cartoon of the Crystal structure and XRD and SEM of lead-free Cs ₂ AgBiBr ₆ double perovskite.	97
Figure 49.	Double perovskite layer optimization and optimization of infiltration of double perovskite solution into mesoporous TiO ₂ .	97
Figure 50.	Absorption spectrum plotted in the form of Tauc plot, for an indirect bandgap, of the Cs ₂ AgBiBr ₆ thin film deposited on glass.	98
Figure 51.	scheme of corresponding energy level diagram and photovoltaic performance with various HTMs.	99
Figure 52.	Device statistic on optimized layers, power conversion efficiency of solar cells	101
Figure 53.	J-V curve for solar cells using antisolvent treatment and PTAA as HTM	101
Figure 54.	IPCE spectrum of Cs ₂ AgBiBr ₆ perovskite solar cells with PTAA	101
Figure 55.	Statistical distribution of photovoltaic parameter for perovskite solar cells performance with different HTMs	102
Figure 56.	<i>J-V</i> curves of forward and reverse scan showing no hysteresis	102
Figure 57.	Molecular structures of synthesized ZnPcs.	110
Figure 58.	Synthesis of phthalonitrile precursors of ZnPcs.	110
Figure 59.	Example of cyclotetramerization reaction.	110
Figure 60.	UV-vis spectra of BI25 (3.11x10 ⁻⁶ M), BL07 (6.05x10 ⁻⁶ M) and BL08 (4.73x10 ⁻⁶ M) in THF solution.	111
Figure 61.	Cyclic voltammograms of ZnPcs-based HTMs.	111
Figure 62.	Cross-sectional SEM image of perovskite solar cell using BL08 as HTM and Energy level diagram of PSCs with different HTMs.	112
Figure 63.	J-V curves of perovskite solar cells using BI25, BL07 and BL08 as HTMs	113
Figure 64.	Chemical structures of HT-ZnPc, HBT-ZnPc, and TB-ZnPc	120
Figure 65.	UV-vis spectrum and Thermogravimetric analysis of ZnPcs	120
Figure 66.	UV-vis absorption (solid line) and emission (dashed line) spectra and Energy band diagram of ZnPcs.	121

Figure 67.	Effect of addition of pyridine on the UV-vis absorption	121
Figure 68.	SEM cross-section image of a typical device, and JV curves and EQE of PSCs.	122
Figure 69.	J-V curve and EQE measured for one of the highest efficient cells	124
Figure 70.	EQEs of ZnPc-based perovskite solar cells and UV-vis absorption spectra of the corresponding ZnPc thin films on glass substrates	125
Figure 71.	Statistics of average values obtained for perovskite solar cells	126
Figure 72.	Steady-state fluorescence spectra and time resolved decay at interface between perovskite and HTMs.	126
Figure 73.	Lateral conductivity of the doped HTMs and top surface morphologies of HTLs.	128
Figure 74.	2D GIWAXS images of ZnPcs	129
Figure 75.	Illustration of the solar cells architectures fabricated with rGO in each layer	135
Figure 76.	High-resolution XPS C1s spectra for GO and rGO.	136
Figure 77.	Cross-sectional FE-SEM of different PSCs.	136
Figure 78.	<i>J-V</i> curves of the best performing devices for each architecture described in Figure 75	137
Figure 79.	SEM top view of perovskite and spiro-OMeTAD layers without and with rGO	138
Figure 80.	The schematic image for energy level alignment with rGO	138
Figure 81.	Statistics of the efficiency distribution for devices	139
Figure 82.	<i>J-V</i> characteristics and PL decays of the solar cells with Li treatment	140
Figure 83.	PL spectra of the m-TiO ₂ based sample treated with Li and with rGO in the TiO ₂ matrix	141

List of Tables

Table 1.	Determination or expectation of perovskite structure by a tolerance factor.	27
Table 2.	Decay lifetime from PL fitting in Figure 40	85
Table 3.	Photovoltaic parameters of devices based on the different HTMs	100
Table 4.	Summary of photovoltaic characteristics extracted from J-V curves of perovskite solar cells employing BI25, BL07 and BL08 as HTMs.	113
Table 5.	Optical and electrochemical characteristics of the compounds	122
Table 6.	Photovoltaic parameters of representative ZnPc-based PSCs	123

Chapter 1. Introduction

(Organic and inorganic hybrid perovskite, illuminating new path of solar cells)

1.1. Introduction of perovskite

Organic–inorganic hybrid perovskite materials have emerged dramatically in recent photovoltaic history with a rapid increase of the number of publications. This perovskite materials looked like “Game-changer” in photovoltaic market field because their high performance from perovskite solar cells followed up the other different kind of previous solar cells. Even all of development have accomplished since 2009, when organic-inorganic hybrid perovskite materials were used first. In addition, their low fabricating cost is more attractive to many researchers and investors.

Before entering photovoltaic and materials, we here need to scan briefly about original and general properties about perovskites themselves. Perovskite type crystals, discovered first in 1839 as calcium titanium oxide mineral (CaTiO_3) and named for a finder of Lev Perovski, have indicated now all of same type crystals as ABX_3 with ideal perovskite structure. In ABX_3 , the perovskite crystal structure can accommodate a wide variety of cations (A, and B) and anions (X) within sustaining same structure, which allows the development of the uncountable perovskite type crystal structures. As these results, various novel and surprising researches also have been unraveled.

The one kind of perovskite structures can be a high temperature superconductor described as a distorted oxygen deficient multi layered cuprate perovskite structure.¹ This compound shows superconductive property between alternating multi-layer planes. Recently, organic-inorganic hybrid perovskite has been employed in solar cells as light absorber yielding high power conversion efficiency (PCE) exceeding 23%.² This value is comparable to established multi crystal Silicon (Si) solar cells. Inorganic perovskites are investigated as optoelectronics due to their bright and stable photoluminescence as nanoparticles.³ Additionally, the perovskite oxide family are utilized in catalysis and electro-catalysis as an attractive path.⁴ With the flexible electronic structure, the perovskite oxide compounds are found in various solid states devices, such as ion diffuser for gas sensor and fuel cells, and solid-state ferroelectric devices, and superconductor.

1.1.1 Perovskite crystal structure

In ideal ABX_3 perovskite compounds, perovskite crystals are abided by the charge equation for neutrality.

$$q_A + q_B = -3q_X$$

For examples, the first perovskite CaTiO_3 show us $q_A = +2$, $q_B = +4$ and $q_X = -2$. Organic-inorganic hybrid perovskite we studied deeply show $q_A = +1$, $q_B = +2$ and $q_X = -1$. If some crystals can be

sustained by following the composition with perovskite structure, the crystals can be named perovskite.

The ideal perovskite structure (ABX_3) is a cubic cell having body centered B in 6-fold coordination, surrounded by an octahedral 6 X as face centered, and the A at the corner positioned of the cubic cell (Figure 1). Or we can represent body centered A in a cuboctahedral cage of 12 X and 6 B at the corner position.

Goldschmidt tolerance factor.^{5,6}

In the perovskite cubic structure, the relative ion size is quite important to keep stability of crystal structure. So, a slight change of the ion size will lead distortion and buckling in the structure. For example, a rebellion of big cations or anions will break the cubic structure of perovskite.

The Goldschmidt tolerance factor developed by Victor G. Goldschmidt is a good tool to check the crystal structure stability and distortions. It is induced from a close-packed sphere model. The tolerance factor takes into account that three types of spheres, A, B, and X, in a perovskite-structure have contact each other.

Since ionic radii are known very precisely, the predictions can be calculated well. Although organic inorganic hybrid perovskites sometimes can be constructed from mixed organic cations and anions, which indicate the size of mixed cations and anions cannot be determined precisely, the factor is fairly reasonable to predict the properties of hybrid perovskites. The anion-cation sphere in the ideal cubic perovskite and the lattice parameter are shown in Figure 2. The green line (a) is the sum of diameters of X anion and B cation, $2(r_X + r_B)$. At the same time, the sum of the diameters of anion and A-cation, $2(r_X + r_A)$ is same to the diagonal line of the green line (a) length plane. Thus, we can induce the below equation for ideal cubic perovskite.

$$r_A + r_X = \sqrt{2}(r_B + r_X) = a\sqrt{2}$$

Here, the Goldschmidt tolerance factor is introduced as τ , which is simply the ratio of the above equation's left side and right side.

$$\tau = \frac{r_A + r_X}{\sqrt{2}(r_B + r_X)} = 1 \text{ (for ideal cubic perovskite)}$$

By changing the radii ions, the tolerance factor is also modified and we can figure out what happen on the structure like Table 1.

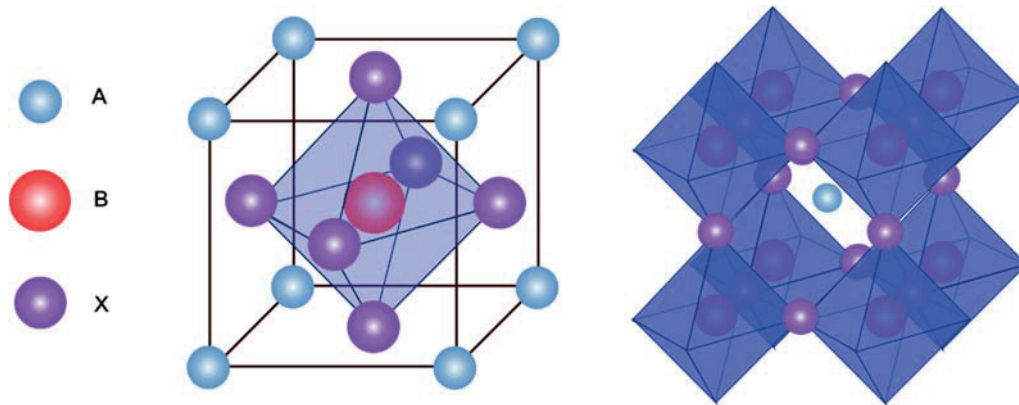


Figure 1 Scheme of perovskite structure for different section (B cation centered and A cation centered).

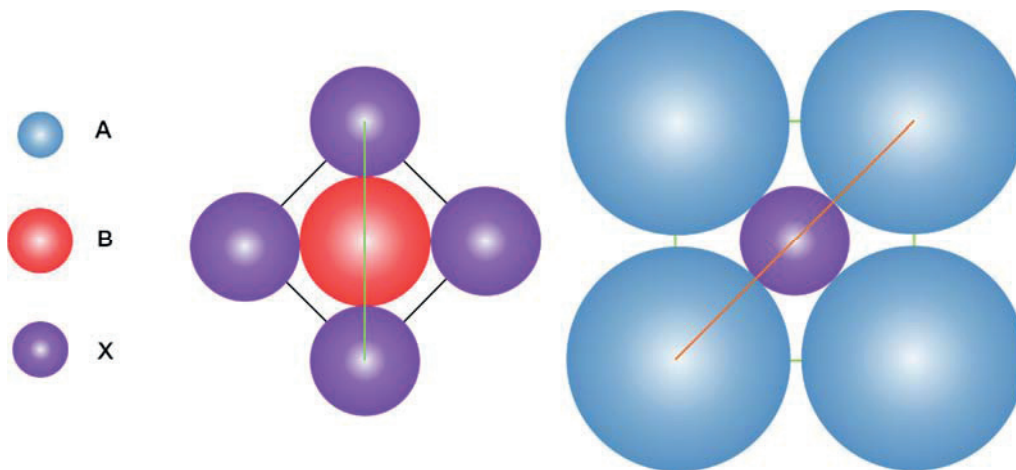


Figure 2 Illustration of sphere model in ideal cubic perovskite. First one is cross-section of center of perovskite unit cell. Second one is side view of face of perovskite unit cell.

Table 1 Determination or expectation of perovskite structure by a tolerance factor.

Tolerance factor	Possible Structures	Explanation
$\tau > 1$	Hexagonal or Tetragonal	A-cations are too large to fit
$0.9 < \tau < 1.0$	Cubic	Ideal size of ions
$0.71 < \tau < 0.9$	Orthorhombic or Rhombohedral	A-cations are too small to fit.
$\tau < 0.71$	Possible close-packed structures corundum structure (disordered arrangement of cations) ilmenite structure (ordered arrangement within sheets) K Nb O ₃ structure (sheetwise ordered arrangement)	A-cations are similar to B-cations.

In organic-inorganic hybrid perovskite, the tolerance factor is a quite good tool for expectation and comparison with empirical results. When we moved to mixed perovskite, we replace and change the elements in perovskite structure. At that time, we can determine which elements or ions will be too small or large to fit in perovskite structure.

1.2. Photovoltaics.

As our world is developing and our society has civilized currently, the energy consumed by people is also increasing dramatically. In statistics, global energy production in this year has already become two times more than thirty years ago and many future expectations indicate even more increase for energy demands will occur. Here, the main point is that over 80% of the global energy consumed comes from the fossil fuels and nuclear sources at the moment. This situation should be discussed for the future. The first main problem of fossil fuels is they are producing massive carbon by-products emission, causing severe climate change and air pollution. Nuclear energy also has the possible danger by accident occurred, as we can see the accident of Chernobyl and Fukushima Daiichi nuclear disaster. In addition, these energy sources cannot be used infinitely and will be depleted because of their limited amount in earth. Therefore, we need to use clean renewable energy. As one of clean energy sources solar energy is a very attractive alternative, acting as a sustainable and practical answer to the challenge of meeting the growing global energy demand. In specific, we can get the solar energy everywhere on earth and the amount of solar energy received by sun light on earth for only one hour is sufficient to power required in the entire planet for one year.

1.2.1 Semiconductors⁷

Among various ways to utilize infinite solar energy, solar cells are the high priority option because these devices can convert the solar energy into electric energy directly. We call this process photovoltaics (hereafter PV). In our present world, where we can do most of activities and operate machines with the electricity, solar cells are perfect to satisfy our demands. And how do solar cells work? For understanding the principle of solar cells, we need to know the physics of semiconductor because solar cells are typically made of different types of semiconductors and work by the special properties of semiconductors.

The semiconductor is the solid material that has electrical conductivity values between a conductor and an insulator, and this conductivity is generated under specific conditions. These conditions can

be various depending on the kind of semiconductors. Before explaining the difference of conductivity we need to start from basic and understand the band gap theory. Every atom has a nuclear in center and electrons in atomic orbitals having intrinsic discrete energy level for each of them. If two atoms come together to form a molecule, the atomic orbitals of each atoms and electrons in that orbitals should overlap. And then by Pauli exclusion principle the overlapped orbitals will split into new discrete molecular orbitals, such as bonding orbital and anti-bonding orbitals, which have different energies as shown in Figure 3a. The electrons existing in atomic orbitals before bonding will fill from the bottom of molecular orbitals (Figure 3a) For a solid having crystal lattice, since an infinite number of regular arranged atoms are required to compose a crystal, the separated orbitals are also generated infinitely and get so close together that the discrete energy level become continuous energy bands. This result is shown schematically in Figure 3b, where the r_0 represents the equilibrium interatomic distance in the crystal.

Let us imagine again atoms containing many electrons in a solid. For example, the atom has electrons up through the $n = 3$ energy level. When atoms are brought closer together, the outermost electrons in the $n = 3$ shell will begin to interact initially, and the electrons in the $n = 2$ shell may begin to interact and finally, the electrons in the $n = 1$ level may interact. The splitting discrete energy from different shells are resulted in Figure 4a. If the equilibrium interatomic distance is r_0 , we can think two bands that the electrons may occupy and forbidden energy gap between separated bands. This explanation is the simplified energy-band theory of single-crystal materials. The actual band is much more complicated than this one. This formation of bands is mostly a feature of the valence electrons in the atoms because valence electrons are relatively weakly bound rather than inner electrons (core shell electrons) and are the electrons involved in chemical reactions. For example, in a silicon crystal, the four remaining $n = 3$ valence electrons interact and show the band splitting of silicon like Figure 4b. The higher band is called conduction band and lower band is called valence band. Almost energy states in valence band are filled with electrons and conduction band is normally sustained empty.

Thus, every solid has energy band structure. Energy band structures are varied depends on kinds of atoms and chemical compounds, and these models facilitate the understanding about the inborn properties of each solids. For the electrical conductivity, a metal is defined when a material show the electric current under electric field. It indicates electrons can move freely, thus the valence electrons in the metal can escape easily from atoms and covalent bonds. As a perspective of band theory, that means electrons in valence band should be transferred to empty states of conduction band, and

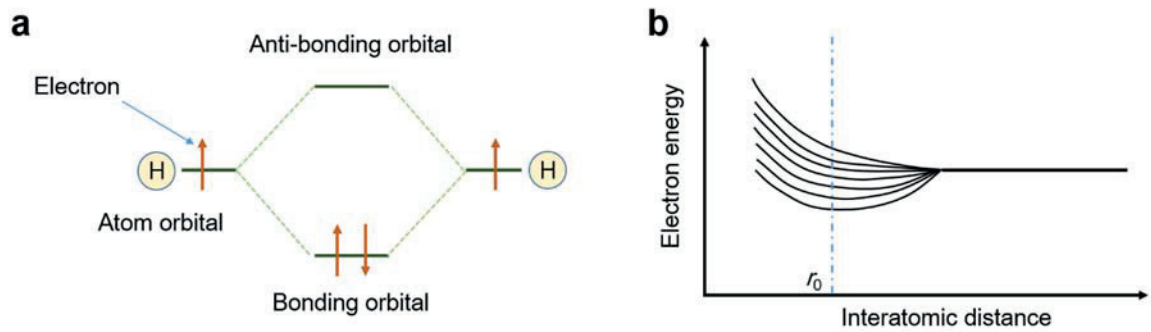


Figure 3 a) the formation of bonding orbital and anti-bonding orbital from two H atom orbitals and H_2 electron configuration. The two electrons occupy one bonding orbital at lower energy, and one antibonding orbital are empty. b) The splitting of an energy state when regularly arranged atoms with closing distance and the formation of a band from the infinite separated energies.

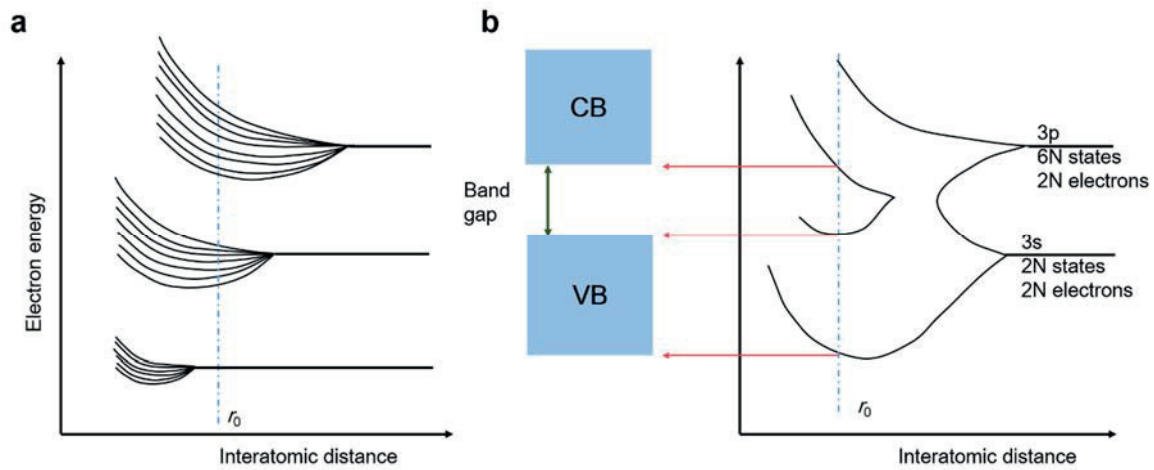


Figure 4 a) Schematic about the splitting of the atoms having electrons up to $n=3$ level and the formation two band. b) The splitting of the 3s and 3p energy states in a silicon crystal and the formation of conduction band valence band, and the band gap.

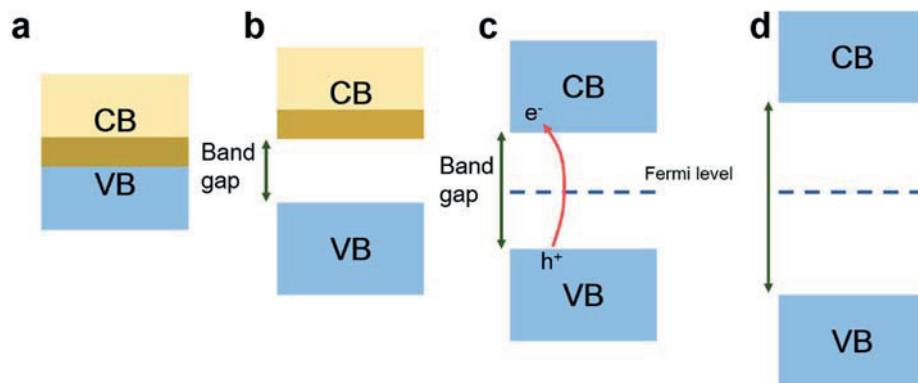


Figure 5. An energy diagram of band structure in a) a conductor, b) another possible conductor, c) a semiconductor, and d) an insulator.

then electrons can move freely in conduction band. In Figure 5a and b. (metals) it is shown two ways for explaining high electric conductivity, either no energy gap or small energy gap between valence and conduction band. For the former, conduction band is overlapped with valence band, where electrons don't need external energy to jump from valence band to conduction band. And for the latter, a small band gap is existed and the electron filled up from the bottom exceed the valence band and begin to enter the empty states of conduction band. In addition, a significant number of electrons are thermally excited into empty levels, allowing to conduct electricity.

Unlike metals, semiconductors are described as materials having a band gap, where additional external energy is necessary to excite electrons from the valence band to the conduction band. Thus, to have high electrical conductivity, valence electrons in semiconductors should be excited from the valence band into the conduction band by obtaining additional energy exceeding the bandgap energy. Here, in photovoltaics, it is the energy of photons. That is the reason why the semiconductor is used in solar cells. Finally, insulators is solid materials that do not have any electrical conductivity because the bandgap in insulators is so large that electrons are not promoted to the conduction band.

1.2.2 Doping: N-type and P-type semiconductors.

In semiconductors, we can alter characteristics greatly by doping technique of additional elements into the semiconductors crystals. We call the pure semiconductor, if constructed by one kind of atom, an intrinsic and the doped semiconductor an extrinsic material, respectively.

We can examine the extrinsic case more carefully. For explaining easily, a typical semiconductor Si is considered. Now a phosphorus (P) atom replaces one of the Si atoms in the lattice as shown in Figure 6. The P atom, which is at the right side of Si on the periodic table, has an extra proton and an extra electron. Since the proton is bound to a nucleus, the extra electron can be left freely after 4 valence electrons of P atom form 4 covalent bonds as shown in Figure 6b. In the band theory, it can be considered additional electron will fill the conduction band. Here, the P atom works as a donor in silicon lattice because it donates an electron to the conduction band. It is also known as a n-dopant and the silicon having n-dopants is called n-type silicon.

Analogously, we can expect about doping an aluminum (Al) atom, which has one fewer electron and proton than Si. So a silicon will have one free electron because this electron is left after 3 valence electrons of Al atom are used to form 3 covalent bands as presented in Figure 6c. Or we can imagine a hole is moving freely from the valence band. In this case Al is known as a p-dopant and we call the silicon have p-dopants p-type silicon.

In both case of n-type and p-type semiconductors, the electric conductivity increases because of the increasing number of available free electrons and holes, respectively. It is interpreted in the energy band diagram of Figure 7. In n-type semiconductors, the probability that the energy states in the conduction band can be occupied by the electrons increase because the number of free electrons grow up. And the Fermi level, indicating the energy level where the probability of exiting electrons is 50 %, in the n-type semiconductor is close to the conduction band by increase of the n-dopant. P-type semiconductors are opposite to n-type ones. The probability of evacuating energy states in valence band by holes increase and thus Fermi level descends to the valence band.

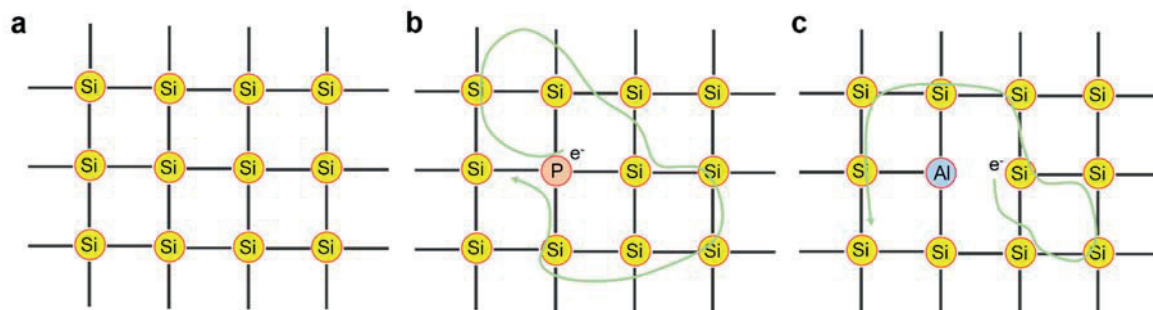


Figure 6. a) A simplified two dimensional intrinsic Si crystal structure. Yellow circles represent the Si nuclear and core shell electrons and the black lines represent the covalent bonding between atoms. b) The representation of a Si lattice n-doped by a phosphorous atom and the remained electron moved freely. c) The representation of a Si lattice p-doped by an aluminum atom and the remained electron looks moving by switching with close electrons.

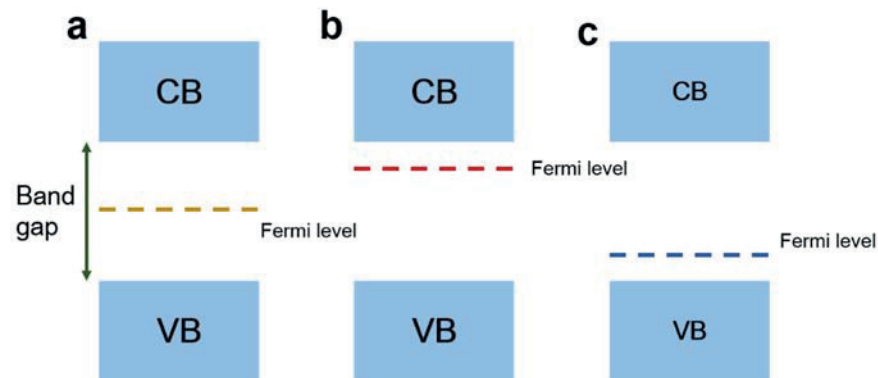


Figure 7. a) Band diagram of an intrinsic Si crystal. b) n-type Si crystal. The Fermi level is just below conduction band. c) Energy diagram of a p-type Si solid. The fermi level is close to valence band.

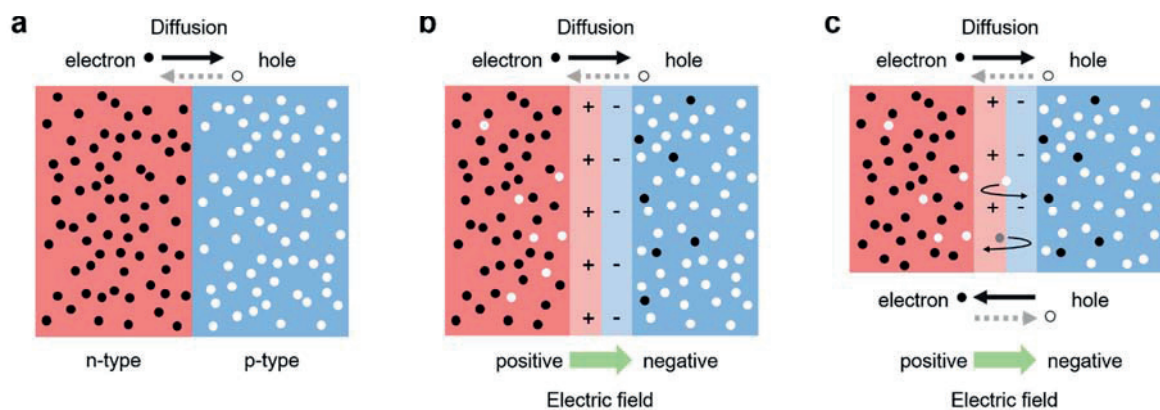


Figure 8. a) n-type and p-type semiconductors are attached together. Electrons and holes can move to each other. b) By diffusion, electrons move from high concentration (n-type) to low concentration (p-type). Oppositely, the hole is diffused from p-type to n-type semiconductor. As a result, the ions at the interface are left behind and a 'built-in' field is established. c) An equilibrium is stabilized between the diffusion and the electric field.

1.2.3. P-N junction.

After doping semiconductors (ex. Silicon) as N-type and P-type, we can join these two materials together. This *p-n* junction is the basic principle for explaining solar cell. As mentioned the n-type semiconductors has large amount of electrons moving freely in materials and the p-type one has large numbers of free holes. Now when these two types of silicon are joined we can expect what happens to the electrons and holes within this junction. Because the large number of electrons are in the n-type Si and the large number of holes are in p-type Si, electrons in n-type Si will start to move to p-type side by diffusion from the difference of concentration as shown in Figure 8a. However, as the electrons diffuse from n-type side to p-type side, electrons are deficient in n-type semiconductor of an equilibrium state, they leave behind the positively charge on n-type Si, especially, at close to the junction interface (Figure 8b). Likewise, on p-type side the negative charge is generated by disappearance of hole, due to the introduction of electrons. This situation causes an electric field at the junction region between n-type and p-type Si from n-type to p-type. As a result, the electrons cannot anymore move from n-type to p-type freely because the electric field attracts them toward the positive side in n-type Si. Thus, a new stable equilibrium state is set up by a balance between the diffusion and the electric field (see Figure 8c). It is the basic concept that is operated in *p-n* junction diodes, transistors and solar cells.

1.2.4. Solar cells.

Solar cells are made of semiconductor materials, typically Si, with a *p-n* junction. When a solar cell is exposed to sunlight, it can generate current and voltage. This is because of the electric field in the *p-n* junction. In detail, the sunlight has normally a lot of photons having various wavelengths like Figure 9a. Within these photons, just ones that have higher energies than a bandgap of Si (> 1.1 eV) used in a solar cell are absorbed to create electron-hole pairs. In other words, the photons having wavelength below 1127 nm are absorbed in Si solar cells. However, if in n-type Si, where is no electric field by the *p-n* junction, electron-hole pairs are generated by the photons, these pairs will stay inside n-type Si and be lost as electrons and holes recombine together. Therefore, the electric field in *p-n* junction is necessary to prevent this recombination of electrons and holes and extract these two charge carriers to opposite directions. The charge carriers generated by incident sunlight are separated by attracting electrons to n-type Si side and holes to p-type Si side, respectively.

p-n diode (no bias, forward bias, and backward bias)

The energy diagram in Figure 9b shows the net thermal equilibrium state and one assumption with

a photon exciting an electrons. In this equilibrium, the Fermi level is constant in which the conduction and valence band bend to connect the Fermi level of n-type and p-type. When a photon having larger energy than a bandgap of a semiconductor is absorbed, an electron is excited to the conduction band and a hole is left in the valence band. However, without any external factor, there is no net current flow.

If we input a potential to the *p-n* junction, it is no longer in an equilibrium and everything in this system will be altered. First we start forward bias by applying a positive voltage to the p-type and a negative voltage to the n-type semiconductor, as shown in Figure 10a. The applied bias across the device is the opposite direction to the electric field in the depletion region. The free electrons in n-type semiconductor are attracted to the positive terminal and the holes in p-type semiconductor are also concentrated to the opposite side. The depletion region becomes thinner and will be negligible as the applied field increase. If the applied voltage is very large, the built-in electric field in the depletion region cannot resist the electron flow from n-type to p-type anymore and the electric current will increase dramatically. In the energy diagram the potential barrier in depletion region does not work.

In contrary, the reverse biased devices shows different results in Figure 10b. The magnitude of the net electric field in the space charge region increase due to the applied voltage. In reverse biased *p-n* junction diode, the free electrons in n-type semiconductor are extracted to the positive terminal and the holes in p-type semiconductor move to the opposite side. As a result, the depletion region becomes wider and the total bias became bigger. At the same time, additional electrons from the negative terminal are injected into the p-type semiconductor. These electrons soon meet large number of holes at the p-type semiconductor and recombine with them. The wider negative ions at p-type semiconductor even oppose the flow of free electrons from going inside. On the other hand, holes from the positive terminal also find large of free electrons at the n-type semiconductor and loss their current. In practice, little amount of electrons and holes can enter this electric field in the wide depletion region and they can move fast to opposite type semiconductor, showing very low electric current density ($\sim\mu\text{A}/\text{cm}^2$).

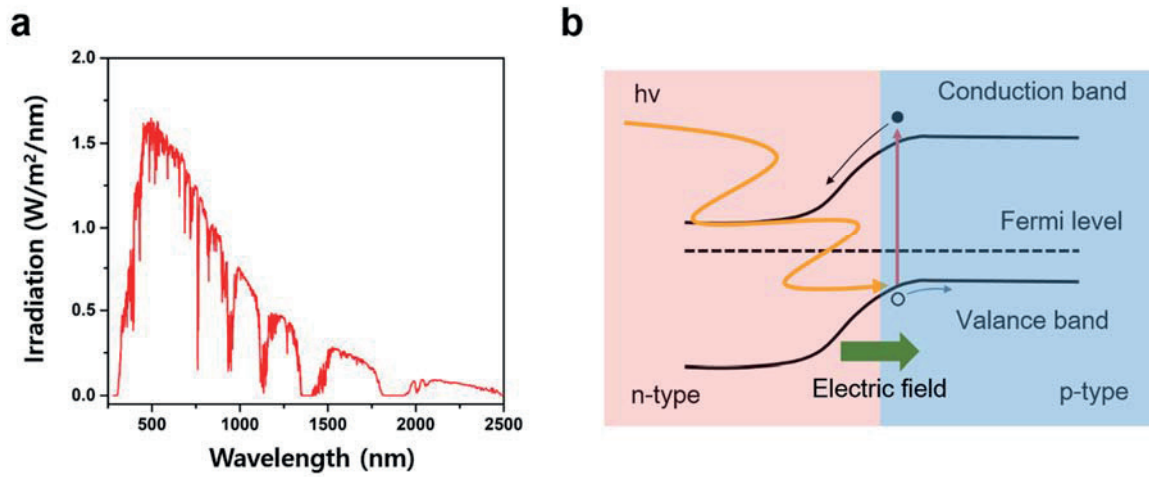


Figure 9. a) Sun light spectrum b) energy diagram in p-n junction diode without any bias and an assumption when a photon is absorbed in the depletion region and excite an electrons.

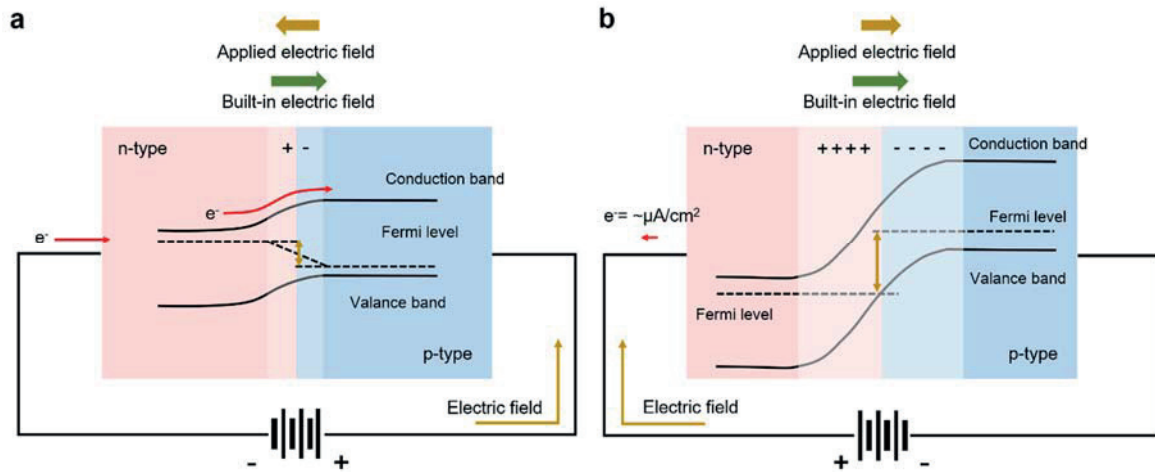


Figure 10. a) p-n diode under forward bias. b) p-n diode under reverse bias.

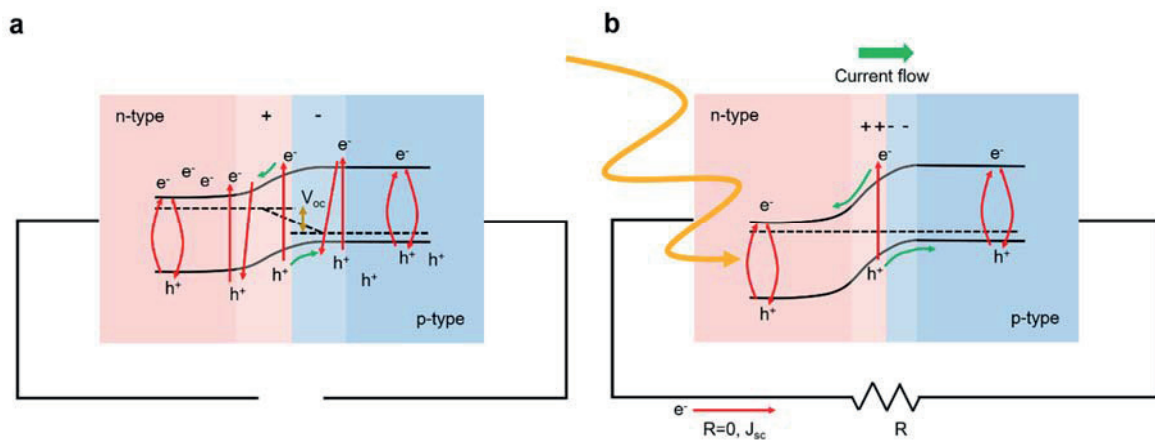


Figure 11. p-n diode under illumination. a) under open circuit and b) under short circuit.

Illumination on p-n junction diode (How a solar cell work)

Now we can understand about p-n junction diodes with bias and under dark. However, solar cells are p-n junction diodes without any bias. So, let us consider when the solar cell is illuminated and how it makes the voltage and current. When photons having sufficient energy larger than band gap are absorbed, additional excitons in n-type and p-type silicon crystals are generated and the charge carriers, such as excited electrons and holes, increase temporarily. Among of these electron-hole pairs, ones which are far from the depletion region having the electric field recombine quickly and loss their energy by heat. However, others excited within and close to the depletion region can be separated by attraction of the electric field. This separation of charges leads to a current flow across the junction, which is indicated the photogenerated current.

When the circuit is open, this process, where the electrons increase in n-type and the holes increase in p-type, leads to forward bias as presented in Figure 11a. The magnitude of the electric field in the depletion region decreases, but does not go to zero or change direction. However, in contrast to forward biased diode, the photocurrent flow to the opposite direction. As the voltage for the forward bias is generated, it grows up to when the forward bias current equals to the photogenerated current. That voltage is open circuit voltage (V_{OC}). And if the circuit is closed and the resistance is zero, thus the voltage is zero, the phtogenerated current flows freely by the electric field (Figure 11b). That current is short circuit current (J_{SC}).

The power generated in solar cells is determined by multiplying the current and the voltage ($V \times J$). When the loaded resistance on the circuit of solar cells is varied, the voltage and the current is also altered simultaneously. At this time the voltage is balanced to the current. In working solar cells, the actual voltage is decreasing from V_{OC} and the matched current is also below J_{SC} . Thus, it can be inferred the maximum power is always lower than the value of $V_{OC} \times J_{SC}$. When the maximum power is taken, the efficiency, which is also known as the power conversion efficiency (PCE), is $(J_{mp} \times V_{mp})/(\text{Input power}) \times 100\%$.

1.3. History and types of solar cells.

For practical commercialization, the high PCE is a key factor for the reduction of installation cost, which means we can generate the electricity with less PV system and reduce the cost of electricity. For these reasons, the development of solar cell efficiency has been done since the birth of photovoltaics, and efficiency records are continually renewed.

Although Si solar cell is a main subject at the first time and many researches is still proceeding to upgrade, other thin-film materials have also been explored with the aim to overcome a limitation of established Si solar cells. Below, I systematically list the state of the art of the most studied geometries of PV materials and compare the limitations of each material and its potential for further improvement and large-scale application. Next, I scan from the beginning.

Silicon

The silicon has a really good band gap size (1.12 eV) for reaching high efficiency because it can absorb the light from about 1100 nm of wavelength to 250 nm. As mentioned above, Si cells are made of p-type and n-type Si substrates, based on a p-n junction. With the simple basement, modifying the device architectures and contacting skill have been developed for improving the efficiency. For examples, the surface passivation of Si and minimizing contact area have been implemented to reduce the contact recombination representing a major source of loss energy. As a result, the record efficiency of the best Si solar cell is 26.1%.² This achievement is also combined with improving the collecting sunlight by texture modification.

Although the Si solar cell seems to be perfect for photovoltaics and a resolution our future energy insufficient problem, it is limited to be commercialized because of a low absorption coefficient. As the absorption coefficient is low, the Si layer in the Si solar cell should be thick to absorb all of light having active wavelength (250 ~1100 nm), where a minimum thickness is normally 100 μm . However, a thick Si layer leads to higher recombination and thus results to reduction of the efficiency. To decrease the recombination, we need very high quality, meaning expensive, of Si wafer composed of monocrystalline. This is the reason why the commercialization is difficult. Multicrystalline Si can be also used to reduce the fabrication cost. Absolutely, electronic properties shown in monocrystalline Si are lost and the efficiency of multicrystalline Si, 22.3%,² is lower than monocrystalline. However, this efficiency is not bad for today. The installation and fabrication cost of Si solar cells are decreasing continuously.

GaAs (Gallium Arsenide)

As the record efficiency is 28.9%,² the GaAs solar cell shows the highest efficiency among a single junction solar cell. This is resulted from the outstanding properties of GaAs material, such as a direct band gap of 1.42 eV and a high optical absorption coefficient. In contrast to Si solar cells, the GaAs solar cells need the optimized thickness of $\sim 2 \mu\text{m}$. In addition, it has high electron mobility and

thermal stability. However, the processing methods need a relatively intensive energy and Ga is rarer than gold, meaning very expensive. Encapsulation and recycling of commercial GaAs is required because Arsenide (As) is the toxic.

CdTe (Cadmium Telluride)

CdTe is the second most used solar cells, next to Si solar cells. CdTe solar cells has already used in some of photovoltaic power station. With the band gap of 1.43 eV and high absorption coefficient, the efficiency of 22.9%² is yielded in the laboratory scale. Although the manufacturing cost is low, the Cd is a toxic element and the Te is scare, comparable to platinum, in the earth and contributes to the material cost. Because the architecture of CdTe solar cells is simple and thin, this solar modules will be researched more and following the Si solar modules' market share.

CIGS (Copper Indium Gallium Selenide)

The CIGS is an abbreviation for Copper Indium Gallium Selenium. And if its chalcopyrite crystal structure is kept, In/Ga ratios can be tuned. Depending on the chemical composition, its band gap changes within 1 and 2.4 eV. Cu(In,Ga)Se₂ is reported so far as the best efficiency of 21.7% with the low-band gap compositions. However, due to the availability of tuning composition, many variation and optimization from many different parameters are followed to improve the efficiency. In addition, controlling deposition and annealing progress is important to avoid detrimental secondary unwanted phases. A key element Indium is also very scare to make it hard to be mass-produced. The difficulties for large panels and a low efficiency, comparing to Si solar cells, let investors losing their interest about this material.

DSSC (dye sensitized solar cells)

From dye sensitized solar cells (DSSC), solar cells meet a different class of devices because of their different power generating way and materials used in devices. DSSC generates power by electrochemistry and emitter is not a normal solid semiconductor, but a molecular organic dye. The photo excited electrons in dye are transported into the titanium oxide (TiO₂) and left holes are extracted and moved by a redox couple electrolyte (typically I⁻/I³⁻). The gap between HOMO (highest occupied molecular orbital) and LUMO (lowest unoccupied molecular orbital) of dye is

considered to the band gap of semiconductor and 1.5 eV is shown in the record DSSC (11.9%).⁸ The main problem of this type cell is coming from liquid electrolyte, introducing a large energy loss and a low ionic diffusion. Although DSSC have been commercialized owing to their relatively low-cost materials and simple fabrication, the success of business is not accomplished by low efficiency and short lifetime. However, DSSC inspired for a new pathway of different solar cells like a revolution.

Organic solar cells

Organic solar cells can include DSSC because the main emitter in DSSC is also an organic dye. The solar cells begin with conductive polymer and inspiration from DSSC. Organic solar cells show the similar highest efficiency of 12.6%² by using a polymer with a ~1.6 eV band gap. Polymer solar cells typically have the blended active polymer composed of donor and acceptor. And the blended polymers layer is positioned between a hole-selective layer and an electron-selective layer.

This heterojunction architecture using mixed polymers is necessitated by poor properties of organic materials, such as low dielectric constant, low charge mobility and low diffusion length. However, this distinct structure limits the efficiency of organic solar cells. Because of disordered heterojunction structure, the high rate of non-radiative recombination is accompanied. Thus, this low efficiency and fast degradation rate under illumination make it hard to commercialize the organic solar cells, although there are attracting attributes of ease manufacturing, low weight, and forming flexible modules.

Quantum dot (QD)

The latest one, except the perovskite solar cells, is quantum dot solar cells. Based on the previous knowledge and experiences from DSSC and organic solar cells, the quantum dot solar cells can be developed rapidly. The device architecture is very similar to the solid states DSSC, where the liquid electrolyte for transporting hole is replaced to solid electrolyte. The emitter is a quantum dot, such as PdS or PdSe, not dye. The quantum dots can be fabricated easily and tuned with their optical properties. Their band gap is modified by their composition and size. However, the efficiency is also limited to that of DSSC and organic solar cells. Because of the similar structure to these solar cells, the QD solar cells have same defects and obstacles, such as strong non-radiative surface recombination and inefficient transporting charge carriers from QD to back electrode.

1.4. Photovoltaics with perovskites.

Hybrid organic-inorganic perovskite solar cells (PSCs) show up in PV research field like a game changer. Since the research about PSCs started in earnest, the PCE of 23%, comparable to Si solar cells, was achieved in only 5 years. Now organic-inorganic perovskites are at the center of photovoltaics as a promising next generation technology for accomplishing highly efficient, inexpensive, easy usable solar cells. What does make it possible to improve fast?

As mentioned in the introduction, the basic structure of perovskite is ABX_3 . Hybrid organic-inorganic perovskite has also the same ABX_3 structure, where A is generally one or various kinds of mixed organic cations, B is an inorganic cation, and X is one or mixed halide anions. The most typical model is methylammonium lead iodide ($CH_3NH_3PbI_3$). As shown in CIGS, the perovskite material has also benefits that the band gap or other optical properties can be modified depending on the types or ratios of chemical compositions. For example, we can get higher band gaps by changing iodide to bromide and smaller band gap by tuning from $CH_3NH_3^+$ to formamidinium ($[H_2NCHNH_2]^+$).

The relatively simple fabrication process is another merit. The perovskite films can be deposited by coating perovskite precursor solutions with post annealing at moderate temperature. As the device geometry is close to solid state DSSC and organic solar cells, the manufacture cost is also inexpensive. On transparent conductive electrode, a perovskite layer is coated and additional hole transporting layer and counter metal electrode are all that we need at least to let it work perovskite solar cells. However, the performance is totally different and much higher than that of them, which is the strongest inspiration for many investors and researchers interested.

The very high efficiency come from the remarkable optical properties of perovskite materials. In contrast to previous organic polymers, the perovskite materials have very low exciton binding energy comparable to the thermal energy.⁹ So, the heterojunction may not be required to dissociate electrons and holes from photogenerated electron-hole pairs and the devices can have ordered structures reducing unwanted non-recombination. In addition, the absorption coefficient is very high due to the direct bandgap.⁹ High charge carrier mobility and large diffusion also contribute to high internal quantum efficiency.¹⁰

Despite impressively high performance, PSCs face a big challenge about long term stability, which the devices are fast degraded within few days under standard ambient conditions. However, advanced researches present many improvements, identifying UV light and high humidity are the main reasons for poor stability. At last, using the toxic element, Pb, remains to be resolved because it is more severe than the case of CdTe and GaAs due to its high solubility in water. However, these challenges

will be improved, as the progress has been achieved. Today, for higher performance, the large band gap perovskites are employed in tandem solar cells with Si solar cells or lower band gap perovskites.

1.5. Conclusions and outlook

Although the record efficiency of single-junction solar cells has continually been developing over the years, various established PV materials have approached their limitation, such as theoretical S-Q efficiency limit, and their high production cost always sustained the commercialization of these solar cells. However, the perovskite has quite larger room for improvement than all of the materials discussed previously. In addition, the efficiency record is going up even though it is close to the S-Q efficiency limit. This perovskite material can be applied in various field, such as flexible devices and semi-transparent glasses as building integrated PV systems. For high efficient stable solar cells, many researches and trials are also done in a lot of groups and institute. If the stability is also developed to degree that perovskite solar cells can work for a few years without degradation, they will lead huge revolution in all of energy markets and large-area PV power generation for the utility grid.

Chapter 2. Fabrication of PSCs

2.1. Introduction

Since a possibility about applying organic–inorganic perovskite to photovoltaics was shown first in 2009, perovskite solar cells on a small scale demonstrated power conversion efficiency (PCE) of $\geq 23\%$ with relatively fast development. So, it seems to be very easy to reproduce this highly efficient solar cells. However, except a few research groups, the others are still struggling to prepare PSCs with PCEs above 20%. As the perovskite materials are very sensitive and affected by various conditions and environments, the improvement in the final step, such as jumping to 20%, is quite difficult and required special understanding of fundamental working and fabrication process. Thus, a wider experience and following knowledge about fabrication process is crucial for improving device performances and reproducibility.

In this chapter, I summarize my comprehensive work and knowledge that are accumulated by a lot of experiments and efforts for yielding PSCs with 20%. On development of PSCs, preparing high efficient perovskite solar cells are also becoming complicated in case of conditions that should be considered for optimizations. For instance, the composition of perovskite in PSCs are transporting from basic MAPbI_3 to complex mixed compositions, including multiple cations and anions. And the methods of fabricating devices are also various. Charge carrier transporting materials, such as ETMs and HTMs in PSCs are continuously reported. Unfortunately, uncountable variations as mentioned make it hard to replicate reported protocols from very experienced groups. As one of starting members researching this field, I present typical widespread protocols that are optimized by me and a few key point to be careful as I know.

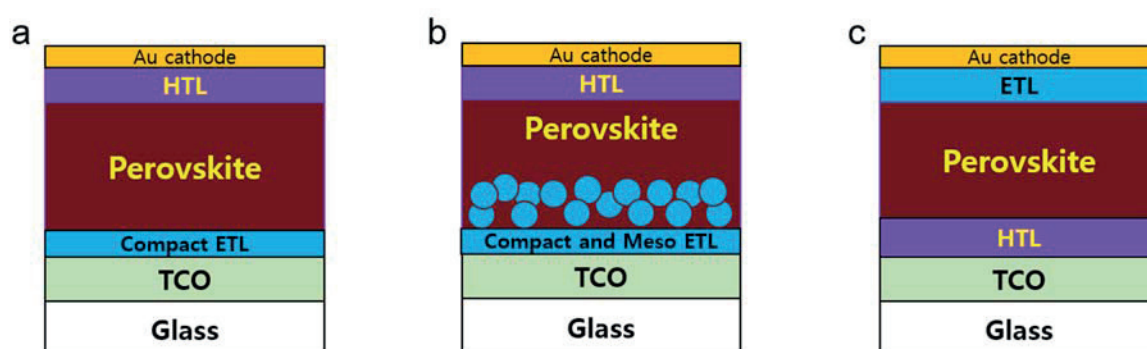


Figure 12 Illustrations of the three perovskite solar cells architectures. (a) Planar $n-i-p$ architecture, (b) $n-i-p$ mesoscopic architecture. The devices configuration is a glass, a transparent conductive oxide (TCO), an electron transporting layer (ETL), the perovskite, a hole transporting layer (HTL), and a gold (Au) electrode.. And (c) $p-i-n$ (inverted) architectures. The devices configuration is TCO/HTL/perovskite/ETL/Au.

2.2. Construction of complete perovskite solar cell.

Commonly and broadly, two types of configuration are used for single-junction PSCs, which comprise $n-i-p$ architectures, where it can be separated again to planar and mesoporous heterojunction, and $p-i-n$ (invert) architectures as depicted in Figure 12. In $n-i-p$ architectures, the side of incoming light, close to FTO glass, is selected for an electron transport layer (indicating 'n'), while the opposite contact is for a hole transporting layer (indicating 'p'). On the other hand, $p-i-n$ (invert) architecture has the hole transporting layer at the light incoming side (FTO glass side). The perovskite layer absorbing light passing through the glass substrate is located between electron and hole transporting layers. Based on these configurations, various research subjects are grouped and focused to the following outline irrespective of architectures;

- Electron transporting layer (ETL)
- Perovskite layer
- Hole transporting layer (HTL)
- Transparent conductive oxide (TCO) layer and glass substrates
- Metal electrode
- Perovskite solar cells structure.

In most of researches and publications, improvements and modifications on methods or materials have been reported on one of each outline. For examples, in the ETL an electron transporting material can be modified from titanium oxide (TiO_2) to tin oxide (SnO_2). Or in the perovskite layer a composition of a perovskite material can be improved from methylammonium lead iodide (MAPbI_3) to perovskite, formamidinium lead iodide (FAPbI_3). Likewise, I tried to find the better conditions of each part in perovskite solar cells by changing a little by little and obtained lots of knowledge and experience through uncountable trial and errors. From my experience, I recognized all of each part in PSCs are important to lead the best performance and the devices are very sensitive to around environment. Even though I fabricated PSCs on same method and procedure, different results were sometimes shown due to unknown factors and changed environments. For my PhD course I have almost concentrated on $n-i-p$ architectures of PSCs. So, I present some experimental expertise and methods for improving the performance $n-i-p$ PSCs.

2.3. Optimization of each part.

2.3.1. Electron transporting layer (ETL)

In the *n-i-p* configuration, ETL is prepared right after FTO is cleaned. Typically, the most used material for ETL is titanium oxide (TiO_2) and recently a tin oxide (SnO_2) is upcoming rapidly.

TiO_2 blocking layer on FTO

Spray pyrolysis

For spray pyrolysis, the cleaned FTO substrates are heated to 450 °C on a hot plate. The substrates are left at 450 °C more than 30 min before spraying because the remained organic residuals and impurities can be combusted. The sprayed solution are prepared diluting titanium diisopropoxide bis(acetylacetonate) in isopropanol. After set up, pure oxygen is turned on for carrying TiO_2 precursor solution and the spraying start. The spray nozzle is rapidly moved from side to side with keeping distance of ~15 cm far from the hot FTO substrates and the pressure is not big, such as little below 1 bar. This moving is repeated a few cycles until finishing the solution. After exhausting the solution, at 450 °C the FTO glasses are left more for 30 minutes and then cooled down slowly to room temperature. Here, we can change the below conditions

- Annealing temperature and time
- Titanium precursors (ex. titanium isopropoxide)
- Diluted solution concentration and amount

I didn't try to scan every condition for spray because this procedure is quite optimized previously. The TiO_2 compact layer has been applied from dye sensitized solar cells. I changed the thickness of compact TiO_2 layer by changing the concentration and amount sprayed. However, I could not find out a big different result from the changing thickness.

Spin coating

A spin coating a TiO_2 precursor solution and heating is another way for depositing TiO_2 layer. The diluted titanium diisopropoxide bis(acetylacetonate) solution is spin-coated on the cleaned FTO substrates. In this procedure, we can modify the concentration, the kind of diluting solvent, rotation speed, and so on. Typically, the FTO layer on glasses are quite rough and the roughness is different depends on the kind of FTO glasses. Therefore, the previous conditions can affect the quality of TiO_2 compact layer more than we expect.

As shown in Figure 13, the TiO₂ layers from spray pyrolysis and spincoating are compared by scanning electron microscopy.

TiO₂ mesoporous layer on compact layer

For the mesoporous TiO₂ layer, we coated the diluted TiO₂ paste (30 NRD, Greatcell solar) in ethanol (1g : 8 ml). It should be left under vigorous stirring overnight before use to separate every agglomerated sticky TiO₂ paste. Here, we also consider the below factors.

- Solvents: Ethanol, Isopropanol, 1-Butanol, Terpineol, mixed with two kinds of solvent, and so on.
- Solution concentration.
- TiO₂ paste: 18-NRT (Greatcell solar), 30-NRD (Greatcell solar), Ti-Nanoxide T/SP (solaronix), SC-HT040 (ShareChem).
- TiO₂ nanoparticles size
- Spin conditions; the rate of rotation and duration.

I tried to change various conditions to improve the performance. The concentration and the solvent used for diluting are quite important to the quality of mesoporous film. If the concentration is too high and the solvent has high viscosity, the mesoporous film coated on TiO₂ layer is not uniform and some pinholes are shown. After I tried with various conditions to find the better morphology, the mentioned condition above was optimized. Of course, this is not the best option and the other method should be tried for improving.

The thickness of TiO₂ mesoporous layer can be controlled by the rotation speed of spin-coating, as well as the concentration of TiO₂ dispersion. The thickness of 150~200 nm can be achieved from the above dispersion with using a rotation speed of 3000 rpm and this thickness is the best condition to my procedure. If reducing the thickness of TiO₂ mesoporous layer too much, a hysteresis may be observed in forward and backward scans of current-voltage (*J-V*) curves as shown in Figure 14.

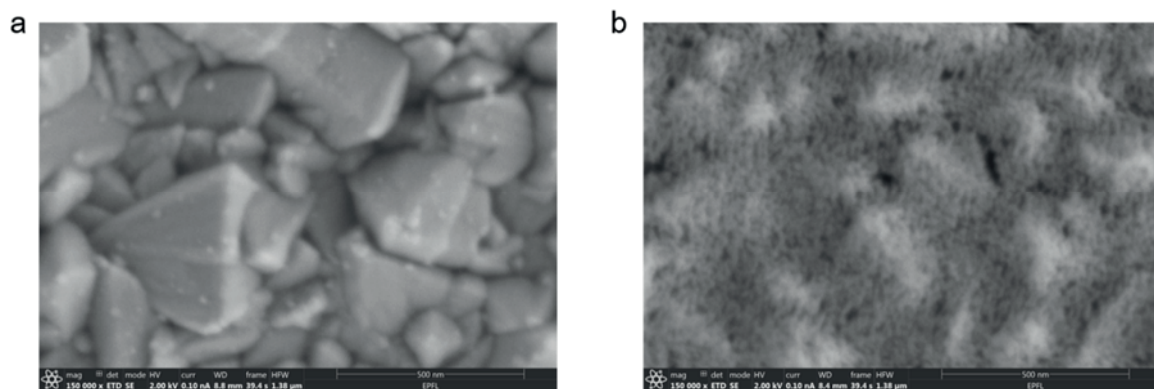


Figure 13 Scanning electron microscopy (SEM) images of compact TiO_2 layer surface. (a) from spray pyrolysis, and (b) from spin coating.

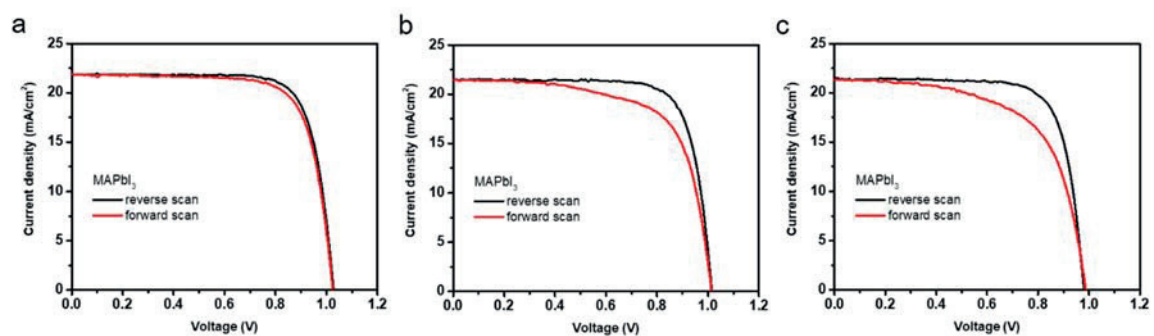


Figure 14 J-V curves measured depending on the thickness of mesoporous TiO_2 layer with hysteresis. Reverse scan from V_{oc} to J_{sc} (black) and forward scan from J_{sc} to V_{oc} (red). (a) about 250 nm, (b) 200 nm, and (c) 150 nm of TiO_2 thickness.

After the spinning, the substrates (FTO/TiO₂ compact/ mesoporous layer) are immediately dried at 100 °C before annealing. Then, the TiO₂ is sintered in the temperature of 500 °C for 30 min. The hot plate is cooled down slowly. And if possible, it is better that the hot (> 100 °C) substrates are rapidly transferred into a nitrogen-filled glovebox because it can reduce the contact and reaction with the moisture in ambient air, especially on summer.

SnO₂ mono layer on FTO or SnO₂ passivation layer on TiO₂ layer

For supplementing a few shortcomings of TiO₂ ETL, the interest about SnO₂ is growing as an attractive solution because that has some better properties, such as a wider bandgap, a deeper conduction band, and much higher electron mobility than TiO₂. As employing SnO₂, we can replace the TiO₂ compact layer to SnO₂ compact layer completely or supplement the TiO₂ layer by covering SnO₂ layer on TiO₂ layer. For both ways, UV ozone or plasma cleaning on FTO or TiO₂ layer is required for about 15 min right before depositing the SnO₂. The deposition of the SnO₂ layer is fulfilled by the spincoating of a diluted SnCl₄ anhydrous in water, respectively. The UV ozone treatment is very important because the spread of the SnCl₄ solution is affected dramatically by the treatment. Then, the coated substrates with the SnCl₄ precursor are dried on a hotplate of 100 °C and heated up to 190 °C. After the whole annealing process, again UV ozone treatment is needed to induce more oxidation of SnCl₄ residual.

Finally, if some spots or dusts are shown after preparing ETL (TiO₂ or SnO₂) on substrates, it may induce a problem when the perovskite solution dispersed or deposited. Even if shown in bare eyes, it will be a big problem in nanoscale of solar cells structure. Discarding these bad looking ones is recommended for reducing error and increasing reproducibility.

2.3.2. Perovskite film deposition

Preparing perovskite precursor solution

The preparation of the perovskite precursor solution has also a lot of complex variation. First, the stoichiometry and the coordination of perovskite complexes within precursor solution may affect the device performances largely. In perovskite materials, the difference in elements composing perovskite structures results in big change of their properties, such as band gap, defect, morphology,

and charge carrier mobility. Therefore, in the preparing various kinds of the perovskite precursor solution, calculating coordination and weighing chemicals are important steps that impact the reproducibility and performance of highly efficient devices. Next, chemicals can be changed by producing companies and purities. Depending the purities and producing companies, the final efficiency is different a lot sometimes. I compared some chemicals from different companies, which were reported on previous journals, and chose the best one among the tested chemical companies. In addition, it is recommend making solutions in a nitrogen-filled glovebox to reduce the effect of external atmosphere (water and oxygen) and keep a controlled preparation environment.

In the following, I detail the recipe of MAPbI₃ solution and mixed perovskite solution. When I started to research about perovskite solar cells, MAPbI₃ composition is normally used for the resource of perovskite layer because this field is in the early developing stage. So, I also optimized every parts in perovskite solar cells with MAPbI₃ at the first time. For MAPbI₃ solution, the PbI₂ is first dissolved in dimethyl sulfoxide (DMSO) at high temperature of about 100 °C. After completely dissolved and showing the transparent yellow color, the PbI₂ solution is cooled down below 50 °C and white MAI powder is added in that solution and stirred for about 10 min. I tried to change some conditions, such as the temperature and time for dissolving chemicals. But, there was no big difference on the final efficiency, except changing a company we ordered chemicals from. We found here the company producing chemicals can also be a significant factor for affecting the performance.

As getting used with experiment and obtaining a standard efficiency from MAPbI₃, I can move the different composition of perovskite materials. The mixed perovskite materials, such as (FAPbI₃)_{0.85}(MAPbBr₃)_{0.15}, has been known to deliver higher efficiency by using a formamidinium cation. So, I applied the experience of MAPbI₃ perovskite to this new perovskite type. It was certainly helpful to reduce the time taken for optimizing and researching. Afterward the addition of alkali metal cations, such as cesium and rubidium (Cs or Rb), was described as enhancing the performance of efficient cells by stabilizing the perovskite structure. However, it was also within similar process as previous development.

For mixed perovskite precursor solution, I first changed a solvent for dissolving PbI₂ and PbBr₂ from pure DMSO to mixed one of dimethyl formamide (DMF) and DMSO (volume ratio of 4:1). This change lead to big differences in film morphology and the efficiency. DMF has a lower boiling point (153 °C) than DMSO (189 °C), which means DMF are more volatile than DMSO. And DMSO has a special ionic bonding with PbI₂. By controlling these two factors, we can find the adjusted point for best quality of perovskite films. If the ratio of DMF increase, the perovskite film will be dried fast during spincoated and the morphology also change. After PbI₂ and PbBr₂ are dissolved at 100 °C

within about 10 min, the solution are left at room temperature for cooling under 40 °C. Then, FAI and MABr powders are weighed and added in PbI_2 and PbBr_2 stock solutions, where I modified a molar ratio of only FAI/ PbI_2 to 1:1.05. The small amount of lead excess was reported and demonstrated by me to enhance the performance. The solutions are stirred and the cation powder is dissolved clearly. If adding Cs to the $(\text{FAPbI}_3)_{0.85}(\text{MAPbBr}_3)_{0.15}$ precursor solution for more reproducible and stable perovskite, the stock solutions of CsPbI_3 are prepared and added with 5 vol % of the mixed perovskite precursor solution.

Depositing perovskite layer.

For depositing perovskite layer, there are two options normally; a sequential method, where the PbI_2 and MAI are coated separately, and one step method of spin-coating a perovskite precursor solution simply. In the sequential method as shown in Figure 15, PbI_2 layer is first coated on TiO_2 layer, and then MAI solution infiltrated into PbI_2 and reacted together. Finally complete MAPbI_3 perovskite layer are produced by drying remained solvent and chemicals.

We can consider below conditions to change a perovskite layer.

- PbI_2 layer; the concentration of PbI_2 precursor solution, the solvent for dissolving PbI_2 , the rotation speed for spin coating, and the drying temperature and time.
- MAI reaction; the concentration of reacting precursor solution, the solvent kind, the solution temperature, the reacting time, and the annealing temperature and time.

At the early stage of this research field, one step method, simply spin coating the MAPbI_3 precursor solution, has a big problem because this way produces many pinholes on the final perovskite layer after coating solution and drying on hot plate, as shown in Figure 16a in SEM. For resolving this problem, excess MAI was dissolved with PbI_2 at a ratio of 3:1. This method was used temporarily because excess MAI can reduce the pinholes by decreasing the drying rate of perovskite films. However, the main milestone for solving this problem is a novel method using solvent engineering by which the perfect clean and smooth perovskite layer without any pinhole can be fabricated. As exhibited in Figure 17, the perovskite film is constructed by spin coating the precursor solution and

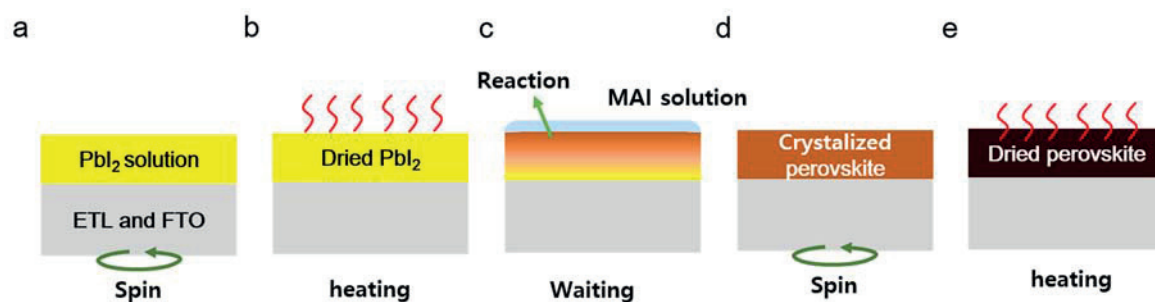


Figure 15 Sequential (two-step) spin-coating procedure for $CH_3NH_3PbI_3$ (MAPbI₃). (a) PbI_2 solution is spin-coated onto the TiO_2 layer. (b) Coated PbI_2 film is dried at 60 °C for 10 min. (c) MAI solution in IPA is then loaded onto the PbI_2 film for 20 s and (d) spun. (e) The reacted perovskite film is heated at 100 °C for 20 min.

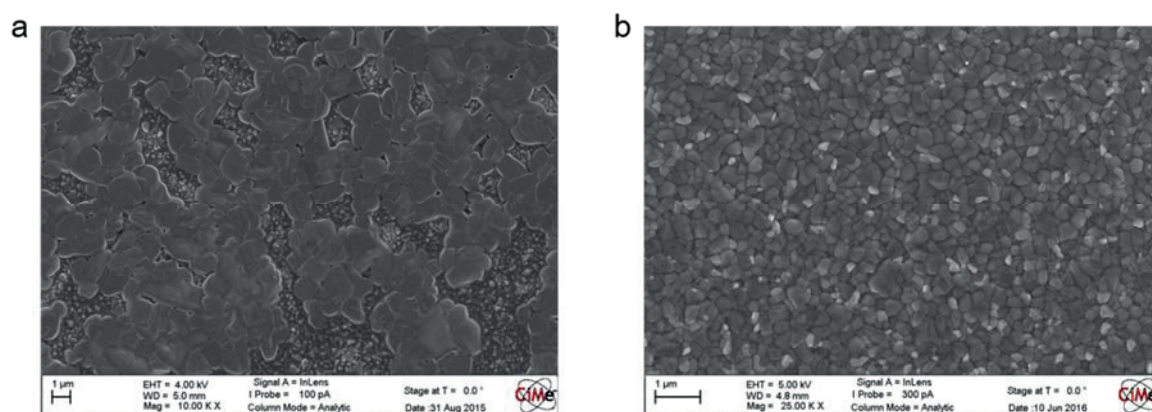


Figure 16 Scanning electron microscopy (SEM) images of top surface of perovskite films by using one step process. (a) When just spincoating and drying the perovskite film. (b) When using anti-solvent dropping during spinning perovskite film.

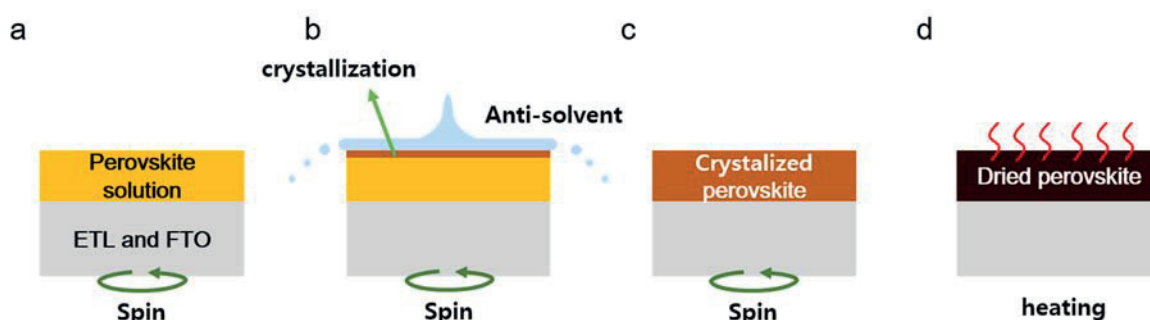


Figure 17 One step processing by solvent engineering. (a) A perovskite solution (ex. MAPbI₃) is spin-coated onto the TiO_2 layer. (b) During spin-coated, the Anti-solvent (ex. Chlorobenzene) is poured onto perovskite film spinning. (c) The perovskite film is formed and crystallized not perfectly. (d) The perovskite film is heated at 100 °C for 30 min.

during spinning the antisolvent is dropped in the center position of the rotating substrate. Antisolvent indicates all of solvents that cannot dissolve a specific chemical powder, thus here perovskite materials. If perovskite precursor solutions meet some solvents and the perovskite powders are precipitated immediately, the solvents will be categorized to antisolvent. As substrates are spincoated, the perovskite solution is spreading and keep a liquid film construction, but the perovskite solution is not dried yet. During this time, the antisolvent is coming from above the perovskite solution film. And it is spreading very rapidly and covering very thinly because the substrates is spinning at high rotation speed. At this time, the perovskite crystals are precipitated on top surface of perovskite liquid film and crystallized fast from top side to bottom side. By this fast transition, the perovskite film can be formed very nicely without any pinhole and covering whole area of ETL as exhibited in Figure 16b.

In general, the antisolvent dropping method follows similar procedures broadly, but sensitive and delicate steps because it is done by hands. Therefore, it needs a long time to become a skillful master for obtaining reproducible PSCs. I used chlorobenzene as the antisolvent and dropped at 10s before the end of the spinning. However, it can be changeable and flexible depending on environment and for improvement. After spincoating, the substrates are heated on a hot plate at about 100 °C. On drying the residual solvents, the surface of perovskite turns to shiny brown-black.

Here, these below condition can be modified.

- Perovskite precursor solution; the concentration of precursor solution, the solvent for dissolving, the rotation speed for spin coating, and the drying temperature and time.
- Antisolvent; the time of dropping antisolvent, the amount of antisolvent, the kind of anti-solvent, the intensity and duration for dropping anti-solvent and the distance between the dropping and spun substrates.

During spincoating or before beginning new batches, I usually clear DMSO/DMF/chlorobenzene solvent vapors in the glovebox by purging fast. The solvent vapors impact dramatically the quality of perovskite films. The gas of glovebox should be continuously changed with new clean for keeping the stable reproducibility of the perovskite film.

2.3.3. Hole transporting layer (HTL)

Spiro-OMeTAD or PTAA in *n-i-p* architectures

A spiro-OMeTAD is the most used hole transporting material in perovskite solar cells, as well as poly[bis(4-phenyl)(2,4,6-trimethylphenyl)amine] (PTAA). Spiro-OMeTAD solution is prepared with tris(2-(1H-pyrazol-1-yl)-4-*tert*-butylpyridine)cobalt(III) tri[bis(trifluoromethane)sulfonimide] (FK209), bis(trifluoromethane) sulfonimide lithium salt (Li-TFSI), and 4-*tert*-butylpyridine (tBP). These additives modify the spiro-OMeTAD more adjusted, such as matching energy level with perovskite materials and improving hole mobility. PTAA also needs Li-TFSI and tBP for working in HTL within PSCs.

Depositing the spiro-OMeTAD or PTAA film on top of the perovskite is simple, just spin-coating the HTM solutions. But, the additive ratio should be exact because a little mistake results in very big difference.

2.3.4. Metal electrode (gold) evaporation

When evaporating the gold, we need to take care if the temperature inside evaporator chamber increase by heating evaporation boats. High temperature is negative to organic HTMs and additives. And it is advised to use the slow evaporation rate of gold to evaporate uniformly and densely at the first stage. For instance, we evaporate the gold to the first 10 nm with the depositing rate of 0.1 Å/s, 0.2 Å/s to 20 nm and then of 0.7 Å/s up to 80 nm.

2.4. Conclusion.

As I tried to improve the performance of PSCs up to over 20% efficiency, some detailed experience and expertise are recorded and accumulated. Everything cannot be reported as a journal because these are too minor things to be published as a main subject. In this chapter, I described these careful protocols about fabricating perovskite solar cells and common things which should be considered to optimize. Additionally, the change of the environmental parameters during fabrication is also important. For example, high humidity in ambient air and the presence of DMSO/DMF solvent vapors in glove box influence the quality of the perovskite films negatively, leading a drop of the device performance. In addition, the kinds and quality of chemical products play an important role on the devices efficiencies. These minors make big difference at the end by accumulated. It is required many practices and experiments for recognizing which one should be improved and optimizing again and again. Recently, through many reports and knowledge about the perovskite

solar cells, it seems easy to get over 20% efficiency. Of course, this will be greatly beneficial in general. However, many trials and errors with practices are still necessary to understand how each factors have effects on the performance of perovskite solar cells and to have creative thinking for improvement.

2.5. Outline of next chapters

Based on the optimized PSCs, we can now apply new ideas and concepts into standard cells. If the standard cells show very low PCE, the papers and researches can loss their trust and seems not to be persuasive. We should develop from similar starting line to other groups. First, in Chapter 3, I designed the passivation skill in backside of perovskite layer, the interface between perovskite layer and HTL. This concept is drawn from a technique in Si solar cells, where a back surface field casing by passivating emitter layer help to prevent charge carrier recombination and improve the V_{OC} in $J-V$ curves. So, I employed formamidinium bromide (FABr) to passivate. Next Chapter 4 shows the supplemented passivation of using low dimensional perovskite structure which is reported as stronger and more stable under high humidity and UV-light than typical three dimensional perovskite (ex. MAPbI₃ and (FAPbI₃)_{0.85}(MAPbBr₃)_{0.15}). Chapter 5 suggested about the possibility of lead-free perovskite solar cells with double perovskite of cesium silver bismuth iodide (Cs₂AgBiI₆). From Chapter 6, the charge transporting layer modification are presented, HTL in chapter 6&7 and ETL in Chapter 8.

Chapter 3. FABr passivation (Highly efficient perovskite solar cells with a compositionally engineered perovskite/hole transporting material interface)

This chapter was published as the above title in *Energy & Environmental Science*, 2017, 10, 621-627.

The permission rule of Energy & Environment Science:

If you are the author of this article you do not need to formally request permission to reproduce figures, diagrams etc. contained in this article in third party publications or in a thesis or dissertation provided that the correct acknowledgement is given with the reproduced material.

If you are the author of this article you still need to obtain permission to reproduce the whole article in a third party publication with the exception of reproduction of the whole article in a thesis or dissertation.

In authors (Kyung Taek Cho, Sanghyun Paek, Giulia Grancini, Cristina Roldán-Carmona, Peng Gao, Yonghui Lee, Mohammad Khaja Nazeeruddin), I am the first author and led the project mainly.

3.1. Abstract

PSCs have experienced an outstanding advance in PCE by optimizing the perovskite layer morphology, composition, interfaces, and charge collection efficiency. To enhance PCE, here we developed a new method *i.e.*, engineering a compositional gradient thinly at the rear interface between the perovskite and the hole transporting materials. We demonstrate that charge collection is improved and charge recombination is reduced by formation of an engineered passivating layer, which leads to a striking enhancement in open-circuit voltage (V_{OC}). The passivation effect induced by constructing an additional $FAPbBr_{3-x}I_x$ layer on top of the primary $(FAPbI_3)_{0.85}(MAPbBr_3)_{0.15}$ film was proven to function as an electron blocking layer within the perovskite film, resulting in a final PCE of 21.3% in LED lamp. Our results shed light on the importance of the interfacial engineering on the rear surface of perovskite layers and describe an innovative approach that will further boost the PSC efficiency.

3.2. Introduction

Perovskite solar cells have been intensively researched in the recent few years because of the unique properties of perovskite materials, which combine a high absorption coefficient,¹¹ good charge carrier mobility,^{10, 12} long charge carrier diffusion lengths and a low recombination rate,^{12, 13} together with an adjustable bandgap depending on the perovskite constituents.¹⁴⁻¹⁶ As a result, power conversion efficiency of PSCs has reached up to 23%, approaching a similar value of the commercial silicon solar cells.² Such a high PCE is attributed to the relatively large open-circuit voltage (V_{OC}) of PSCs, generally over 1.0 V, which is outstanding compared to other photovoltaic technologies such as organic- or silicon based solar cells. However, given that the energy loss ratio of V_{OC} to the bandgap energy (E_g) in PSCs is lower than that of silicon solar cells, and considering theoretical Shockley–Queisser minimum loss in energy is about 250 meV,¹⁷ there is still some gain to achieve a higher PCE by further improving V_{OC} .

Surface passivation is one of the most studied methods to enhance V_{OC} in solar cells without sacrificing short circuit current (J_{SC}) and the fill factor (FF), by reducing charge carrier recombination occurring at heterojunctions. Several materials and methods for inducing passivation have been explored in different solar cells including perovskite photovoltaics.¹⁸⁻²³ Especially, mesoscopic perovskite solar cells, comprising a fluorine-doped tin oxide (FTO)/a compact TiO_2 (c- TiO_2)/a mesoporous TiO_2 (m- TiO_2)/a perovskite/a hole transport material (HTM)/gold (Au), have been found

to be strongly influenced by the efficient charge transfer that takes place at the interface of TiO_2 /perovskite, rather than that of perovskite/HTMs.²⁴ As a result, several studies have been focused on improving the interface between the electron transport materials and perovskite layers.^{21, 22, 25, 26} However, the formation of a rear surface passivation region on the perovskite layer has been hardly attempted except in few works where PbI_2 was partially formed on the perovskite surface and affected the PSCs positively.²¹ The importance of the rear side passivation through the back surface field (BSF) was already recognized and employed in commercialized Si solar cells.^{27, 28} On the other side, the use of sequential layers comprised of quantum dots of different sizes has been recently reported to convey photoelectrons toward an electron acceptor by the induced electric field.^{29, 30} These findings clearly determined that engineering at both interfaces is equally crucial to accomplishing a high PCE.

Here we introduced a surface passivation layer by spin-coating a formamidinium bromide (FABr) precursor on an as-prepared mixed perovskite, $(\text{FAPbI}_3)_{0.85}(\text{MAPbBr}_3)_{0.15}$, film with the presence of excess PbI_2 . By this approach, an additional perovskite layer with enriched Br composition, in the form of $\text{FAPbBr}_{3-x}\text{I}_x$, was formed after reaction with the excess of PbI_2 present on the surface. The wider bandgap bromide perovskite on the rear surface acts as a barrier for charge carrier recombination at the interface between the perovskite and the hole transport layer, resulting in the improvement of V_{OC} .

3.3. Results and Discussion

3.3.1. Design of configuration.

The cell configuration used in this study was based on the following architecture FTO/c- TiO_2 /mp- TiO_2 /perovskite: $[(\text{FAPbI}_3)_{0.85}(\text{MAPbBr}_3)_{0.15}] - [\text{FAPbBr}_{3-x}\text{I}_x]/\text{Spiro-OMeTAD}/\text{Au}$, illustrated in Figure 18a. The perovskite layer was fabricated by sequential deposition of the two different perovskites, $(\text{FAPbI}_3)_{0.85}(\text{MAPbBr}_3)_{0.15}$ and $\text{FAPbBr}_{3-x}\text{I}_x$.^{16, 31} Figure 18b shows a schematic of the energy level diagram corresponding to the device and includes the possible passivation working mechanism for the graded composition perovskite structure. The energy levels used for the conduction and valence band of the different perovskites are presented in Figure 19 and are estimated from previous reports using photoelectron spectroscopy in air.³²⁻³⁴

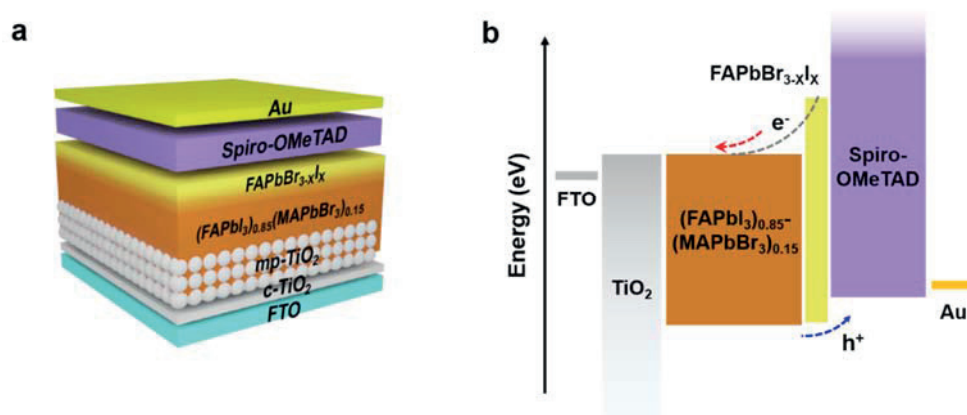


Figure 18 (a) Schematic of a passivated perovskite solar cell. FTO; fluorine-doped tin oxide/compact TiO₂/mesoporous TiO₂/perovskite; $(\text{FAPbI}_3)_{0.85}(\text{MAPbBr}_3)_{0.15}$ and $\text{FAPbBr}_{3-x}\text{I}_x$ /spiro-OMeTAD/Au; gold. (b) Energy bandgap diagram of the device and illustration of how a gradient composition perovskite improved V_{OC} . A different perovskite layer with wide E_g placed at a rear region can block transfer of excited electrons to the HTM layer. The black dashed line represents an assumed banded conduction band energy level.

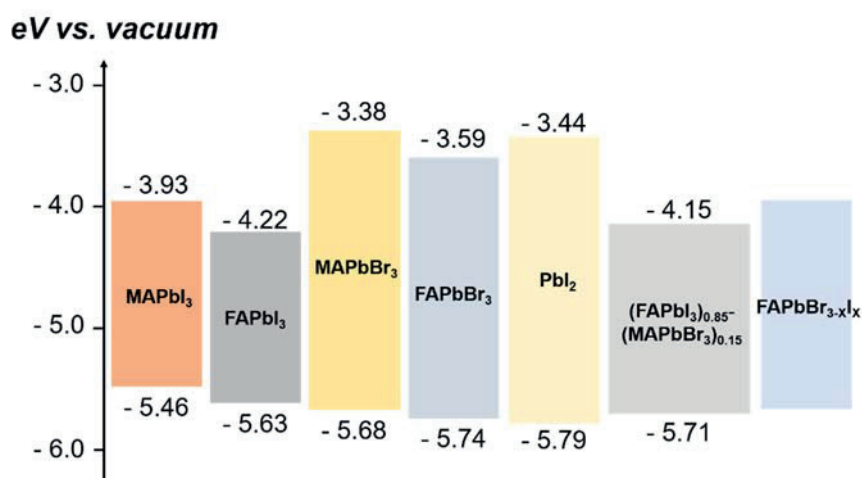


Figure 19 Estimated bandgap edge position of $(\text{FAPbI}_3)_{0.85}(\text{MAPbBr}_3)_{0.15}$ and $\text{FAPbBr}_{3-x}\text{I}_x$. Energy levels for FAPbI_3 , FAPbBr_3 , MAPbBr_3 and PbI_2 are referred from previous papers using photoelectron spectroscopy in air (PESA) and $(\text{FAPbI}_3)_{0.85}(\text{MAPbBr}_3)_{0.15}$ is calculated approximately by a reference from ultraviolet photoelectron spectroscopy.

We assumed that the bandgap edges of the newly formed perovskite, $\text{FAPbBr}_{3-x}\text{I}_x$ on top of the mixed perovskite (at the rear surface), would be close to that of FAPbBr_3 which has a larger E_g and a higher conduction band than $(\text{FAPbI}_3)_{0.85}(\text{MAPbBr}_3)_{0.15}$, leading to the favored energy level alignment. By introducing the thin perovskite layer to the rear surface as depicted in Figure 18b, a gradient in the conduction band was assumed. Expected upward bandgap bending by the passivation layer could prevent backflow of electrons from the conduction band of the perovskite to HTMs,^{30, 35} improving the charge collection. In addition, it is known that traps or defects are located more at the surface of the perovskite film, where the recombination of electron-hole pairs has frequently occurred. This newly fabricated layer will possibly passivate such defects, reducing the interfacial charge recombination and leading to higher V_{OC} .

3.3.2. Fabrication of PSCs and change of morphology

The detailed fabrication process to create the graded composition perovskite is illustrated in Figure 20a. Firstly, the primary perovskite layer, $(\text{FAPbI}_3)_{0.85}(\text{MAPbBr}_3)_{0.15}$, was coated on the mp-TiO₂ layer by the assistance of chlorobenzene dropping (see the methods section for further details). The film was then annealed at 100 °C for 90 min to form a highly crystalline perovskite layer. After cooling down to room temperature, surface treatment was performed by spin-coating FAPbBr precursor solution in isopropanol. By this treatment, the partial or total conversion of unreacted PbI_2 present at the surface region was expected. Finally, the as-prepared FAPbBr film was converted to the thin $\text{FAPbBr}_{3-x}\text{I}_x$ layer by thermal annealing at 100 °C for 5 min. Figure 20b and 20c show images of the perovskite film surface recorded using a high-resolution SEM before and after FAPbBr treatment, respectively, where the change in the morphology occurring at the surface of the perovskite film can be easily observed. Both films are fully covered with polycrystalline perovskite layers over the mp-TiO₂ layer. However, the passivated perovskite film exhibits a denser and more homogeneous surface morphology than the as-prepared film, even when a conspicuous change of the grain size is not observed.

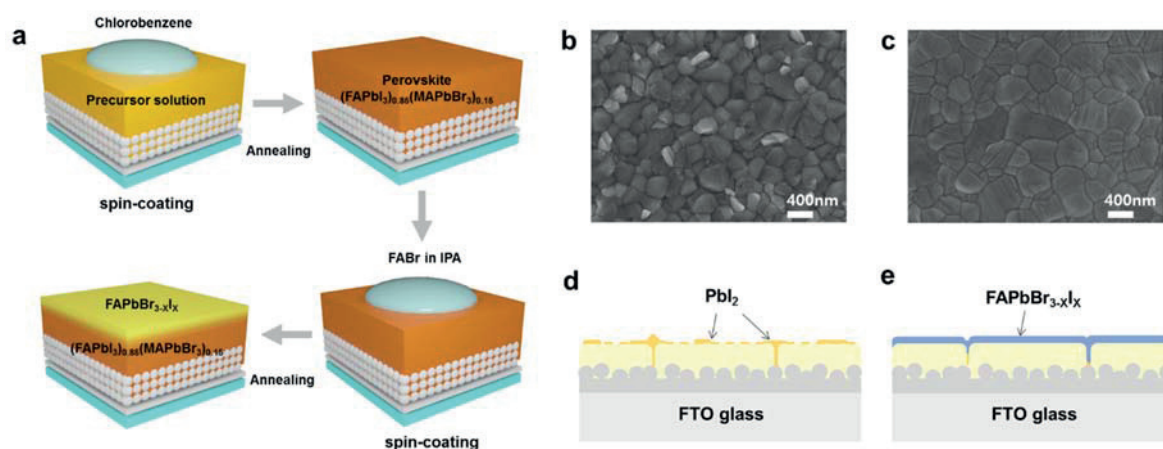


Figure 20 (a) Illustration of a method for fabricating a continuous graded perovskite film by further spin-coating FABr solution in isopropanol on the $(\text{FAPbI}_3)_{0.85}(\text{MAPbBr}_3)_{0.15}$ perovskite film. SEM top-view images of an as-prepared film (b) and a passivated film (c), respectively. Proposed change of cross sectional structures from the as-prepared perovskite film (d) to the passivated film (e).

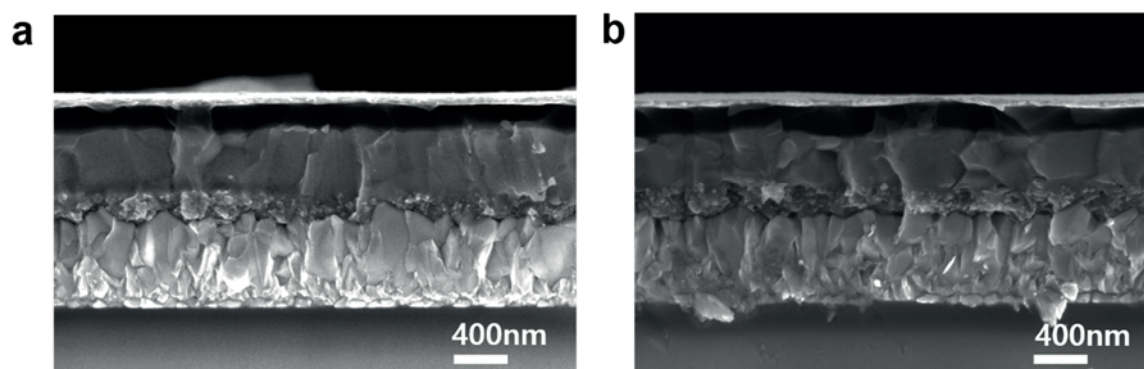


Figure 21 Cross-sectional SEM images of the complete perovskite solar cells. a, From an as-prepared perovskite film. b, From a passivated perovskite film. No obvious difference was observed between devices, which indicates that the passivation layer affects exclusively the surface of perovskite film.

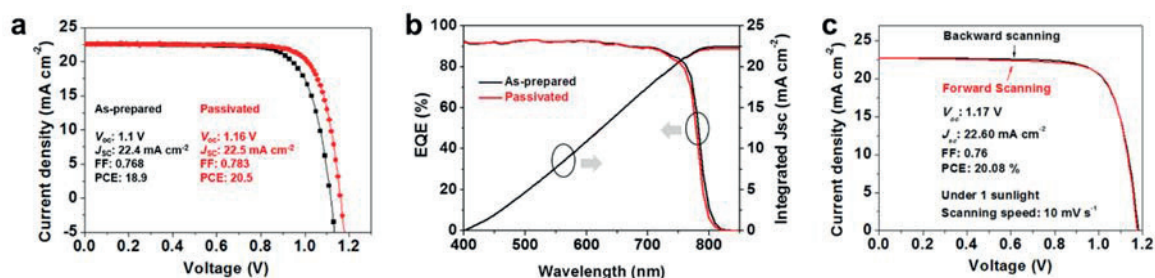


Figure 22 (a) Current density–voltage (J – V) curves of as-prepared and passivated PSCs. (b) EQE and corresponding integrated J_{sc} of the devices. (c) J – V curve hysteresis of the passivated cell.

It is reported that impurities like PbI_2 would likely be placed mostly in the grain boundaries and film surfaces for lowering the formation energy during crystallization.³⁶ In such a scenario, segregated phases of perovskites and PbI_2 may be formed, favored not only by the presence of PbI_2 excess in the precursor solution but also by the post-annealing treatment, which generates very thin PbI_2 -rich layers or a few PbI_2 crystals at the surface.^{36,37} This PbI_2 excess region can then be transformed into a $\text{FAPbBr}_3\text{I}_{3-x}$ layer as depicted in Figure 20d and 20e by using a weakly polar solvent, isopropanol, as the FABr precursor solution. Cross-sectional SEM images of two different complete devices are displayed in Figure 21. In contrast to the visible change shown in the top-surface morphology of the perovskite films, any distinctive difference was not found in the cross section images.

3.3.3. Performance of PSCs.

The current density–voltage (J – V) curves of these PSCs with the as-prepared and the passivated perovskite films are shown in Figure 22a. After generating the passivating layer, the PCE increased from 18.7% to 20.5%. It is notable that this improvement in PCE resulted from the increase of V_{OC} while J_{SC} and FF were almost unchanged. As can be seen in Figure 22b, the external quantum efficiency (EQE) demonstrates values around 90% in the whole wavelength range. For the passivated cells, a small blue-shift of light harvesting shown is maybe due to the formation of a wider bandgap perovskite, this slight difference does not influence J_{SC} . In both cases, the short circuit current-densities integrated from EQE are over 22 mA cm^{-2} , in agreement with those obtained from J – V curves. Moreover, there is a negligible hysteresis when measuring the passivated cells between the forward and reverse bias (Figure 22c), discarding any induced detrimental effect in the charge carrier mobility. Stability was investigated in both the unsealed devices and the passivated cell showed a similar degradation in PCE to the as-prepared one (Figure 23a).

3.3.4. Crystal and elemental change in perovskite films

To explore the passivation layer, we investigated the crystalline structure of the perovskite film. Figure 23b shows X-ray diffraction (XRD) patterns of the as-prepared and passivated perovskite films. Considering the use of an excess of PbI_2 in the precursor solution and the post-annealing time of the perovskite film, it is not strange to find a peak at 12.7° associated with the presence of PbI_2 among other peaks, at 14° and 20° , of typical $(\text{FAPbI}_3)_{0.85}(\text{MAPbBr}_3)_{0.15}$.³⁸⁻⁴¹

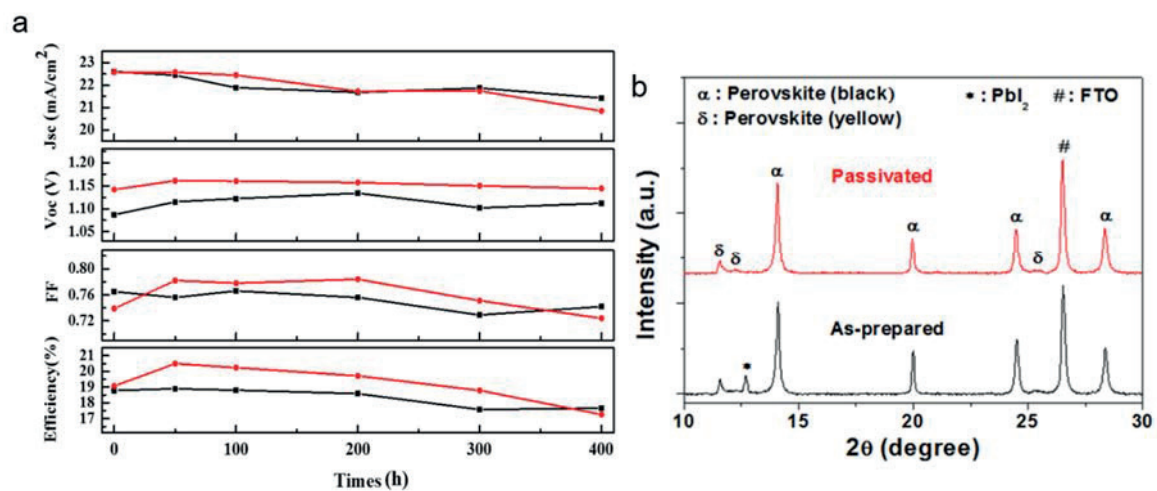


Figure 23 (a) Stability of J_{sc} , V_{oc} , FF and PCE in devices with the as-prepared (black line) and passivated (red line) perovskite film, measured in air without any encapsulation for 400 h. These devices were stored in dark at a relative humidity of 10%. (b) XRD patterns of the as-prepared and passivated perovskite films coated on FTO substrates.

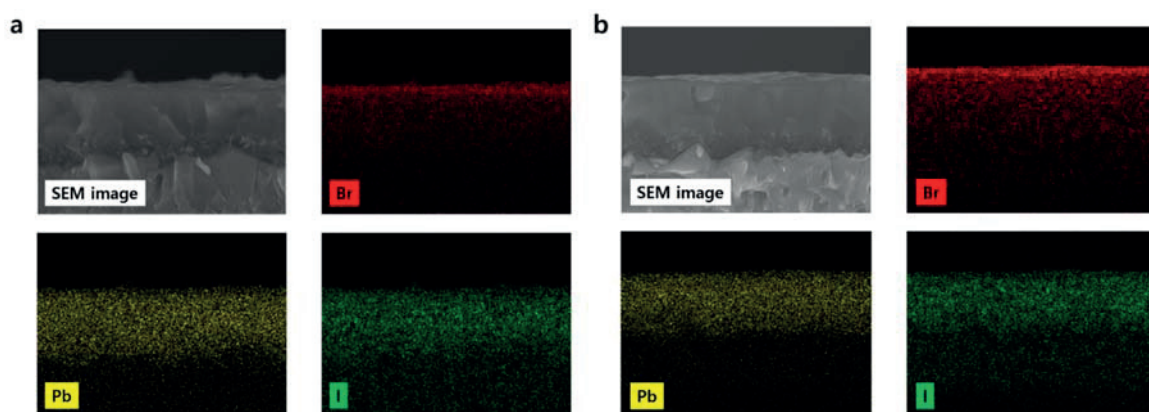


Figure 24 Cross-sectional SEM images and corresponding EDX mapping images of Br, Pb, and I component for as-prepared (a) and passivated (b) perovskite films.

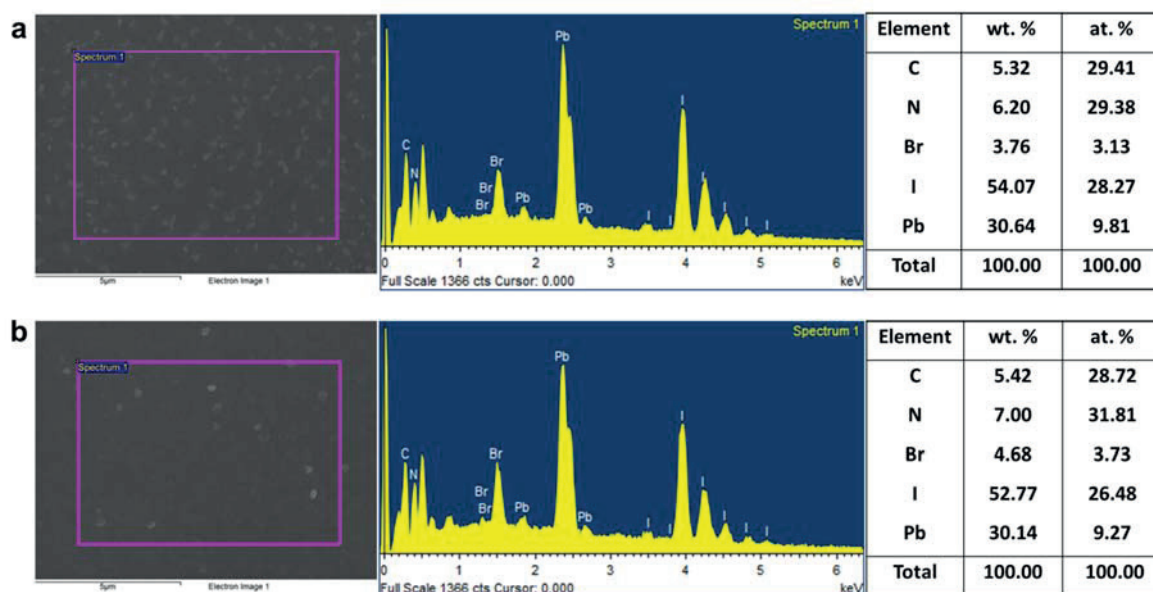


Figure 25 Energy dispersive X-ray spectroscopy (EDS) spectra of perovskite films. a, As-prepared. b, Passivated. Measured atomic percentages of the main elements (C, N, Pb, I and Br) in the annealed perovskite are summarized in tables. Br component can be re-calculated to 7.59 % and 9.45 % (considering Pb, I, and Br) in the pristine and passivated perovskite films, respectively. An increased amount of Br element after spin coating FABr and post annealing is verified.

Interestingly, after reacting with FABr solution the strong peak of PbI_2 is no longer observed, while the other peaks corresponding to the perovskite phase including the hexagonal δ -phase³¹ of FAPbI_3 at around 11.5° are retained with very little change of intensity and positions. In addition, no visible change in the grain size and crystalline primary perovskite has occurred after reaction with a FABr solution, as verified from the full width at half-maximum (FWHM) values of the (-111) diffraction peaks (~ 0.15 for both cases). This is clear evidence that FABr reacted with the excess of PbI_2 present on the surface and did not affect the primary perovskite layer. To further verify the surface conditions, cross-sectional SEM with elemental mapping *via* energy dispersive X-ray (EDX) analysis was also performed. Figure 24a and b showed the cross-sectional SEM images of the as-prepared and passivated perovskite films deposited on the mesoporous TiO_2 layer, and the corresponding EDX mapping images of Br are given in second images of Figure 24a and b, respectively. As observed from the figures, the perovskite films are uniformly deposited over the mp- TiO_2 layer with a 400 nm thick capping layer for all samples. By tracing the three main elements of Pb, I and Br in the films (see Figure 24), we confirmed that both Pb and I elements are uniformly distributed over both perovskite films, without any change due to the influence of FABr solution. On the other hand, although Br ions are likely to exist on top of the perovskite layers even when no post deposition is performed, the stronger intensity of Br can be observed after a passivating layer is created (Figure

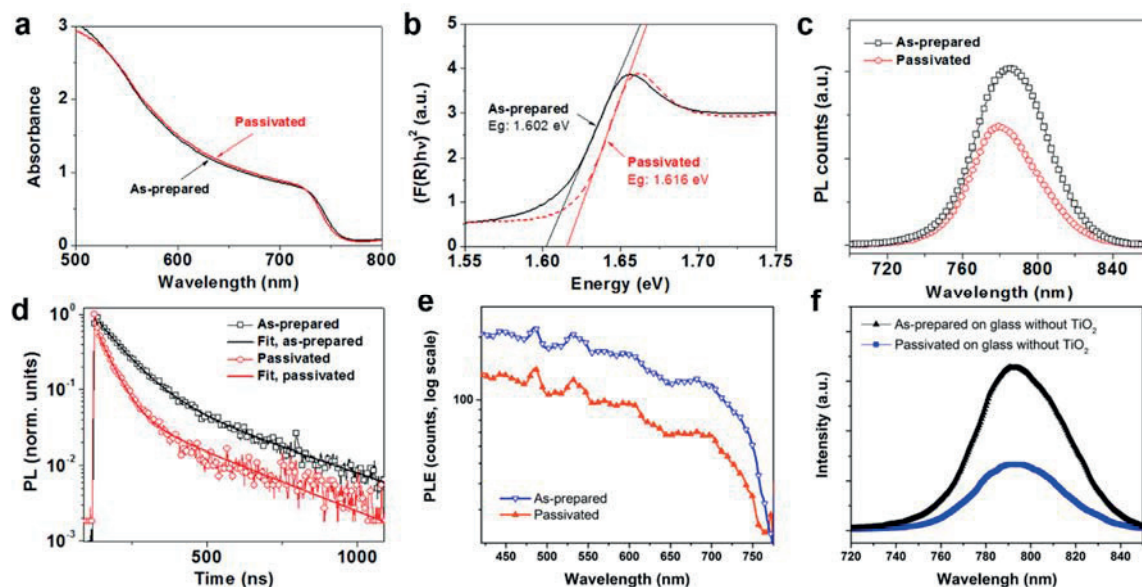


Figure 26 (a) UV-Vis absorbance spectra of the films. (b) Bandgap estimation from reflectance. (c) Steady-state photoluminescence (PL) spectra. (d) Time-resolved PL decays of the perovskite films. All of the measurement was conducted with the films deposited on FTO/compact TiO₂/mesoporous TiO₂ without HTMs. (e) Photoluminescence excitation (PLE) spectra of as-prepared and passivated perovskite films deposited on mesoporous TiO₂. (f) Photoluminescence (PL) spectrum of as-prepared and passivated perovskite films on the glasses without FTO and TiO₂.

24). This point is quite interesting as the aggregation of the Br component was exhibited in mixed lead excess perovskite layers even after one day of aging. However, we can conclude that increasing Br on the surface of mixed perovskite layers by FABr treatment leads to increase of V_{OC} . The quantified EDX analysis from the top view of perovskite films was also carried out and the relative atomic ratio displayed in Figure 25 can support the increased Br concentration. It indicates that the passivation layer was successfully generated on the surface of perovskite films.

3.3.5. Optic characterization and charge transfer.

We investigated the optical changes after formation of the passivation layer. Absorbance spectra in Figure 26a displays that both films have a comparable light absorption, and this is a good agreement with the results that we obtained from EQE and J - V curve measurements. From the absorption profile, a slight shift of the band edge is visible. To highlight it, we measured the reflectance of the films, and the determination of E_g was calculated by applying the Kubelka–Munk ($F(R)$) method which is based on the following equations.

$$F(R) = \frac{(1 - R)^2}{2R}$$

$$(F(R) \times hv)^2$$

where R is the reflectance, and hv is the photon energy. By plotting 2nd equation as a function of the energy in eV, the small difference in bandgaps of these perovskite films (about 0.014 eV) was obtained as shown in Figure 26b.⁴² It is confirmed again that the reaction with FABr solution may increase the bandgap of the product layer.

The bandgap shift is also detected using the photoluminescence (PL) emission spectra, displayed in Figure 26c. We used an incident excitation light of 450 nm from the top surface of perovskite films and measured the PL emission spectra with configuration of FTO/compact and mesoporous TiO₂/perovskite. Note that the light penetration depth being <100 nm, we specifically investigate the properties of the top perovskite layers. As presented, the perovskite film without a passivation layer exhibits a PL peak at 785 nm, whereas the passivated perovskite has the blue-shifted PL peak at 779 nm, which supports the reaction of FABr. This result is further corroborated by the PL-excitation measurements added in Figure 26e. Besides the blue-shift of the emission peak position, the emission intensity of the passivated perovskite film is reduced by *ca.* 30% compared to that of the as-prepared film. This can be possibly due to the change of the perovskite layer to contain more Br ions leading to intrinsic lower PL yield. However, it can also be explained as resulting from quenching, transfer of the excited electrons to the bottom perovskite layer, as allowed by the energetics difference (Figure 18b). The quenching is confirmed again by time-resolved PL decay profiles as displayed in Figure 26d, which was achieved by detecting the emission at 770 nm with the incident exciting light at 700 nm to the perovskite surface. The passivated perovskite film exhibits faster decay fitted by two-time constants of 40 ns and 320 ns than the as-prepared perovskite layer with a time constant of 80 ns. As no HTM was applied on perovskite layers, the shortened PL lifetime can be assigned to a favorable electron transfer occurring at the interface with the bottom perovskite film.³² To further support, additional PL measurement was fulfilled with different configuration with glass/perovskite/spiro-OMeTAD (Figure 26d). Consistent with the above data, even with the HTM the enhanced charge transfer was shown. On the basis of these results, we thus can suggest that the charge recombination was suppressed by the passivated perovskite layers in complete devices. Because the FAPbBr_{3-x}I_x surface passivation layer at the rear surface causes a quenching that can be due to the favorable electron transfer,²³ in the illuminated solar cells the passivation layer will prevent electrons from recombining with holes at the rear surface.

3.3.6. Comparison with passivation and mix.

Although the reduced charge recombination leading to improved V_{OC} was attained from spin coating FABr and post annealing, it remained to be proven if these results came from the passivating layer within the perovskite films or the ion modification of the main perovskite layer after reacting with FABr. To verify the difference between the gradient compositional structure and another homogeneously mixed perovskite structure, we carried out an additional experiment by preparing solar cells from different precursor $(\text{FAPbI}_3)_{0.85}(\text{MAPbBr}_3)_{0.15}$ solution where an excess of FABr was added. Different concentrations of FABr were tested from 0 to 10 mol% excess because we could not find the exact amount of FABr reacted with the as-prepared perovskite layer when preparing the passivation layer. The results, including the absorbance EQE, PL spectra, and $J-V$ measurements, as well as XRD patterns, are displayed in Figure 27 and 28a.

As can be seen, quite different results were observed compared to those obtained when using passivating layers. Regardless of the amount, it was found that mixing excess FABr with the

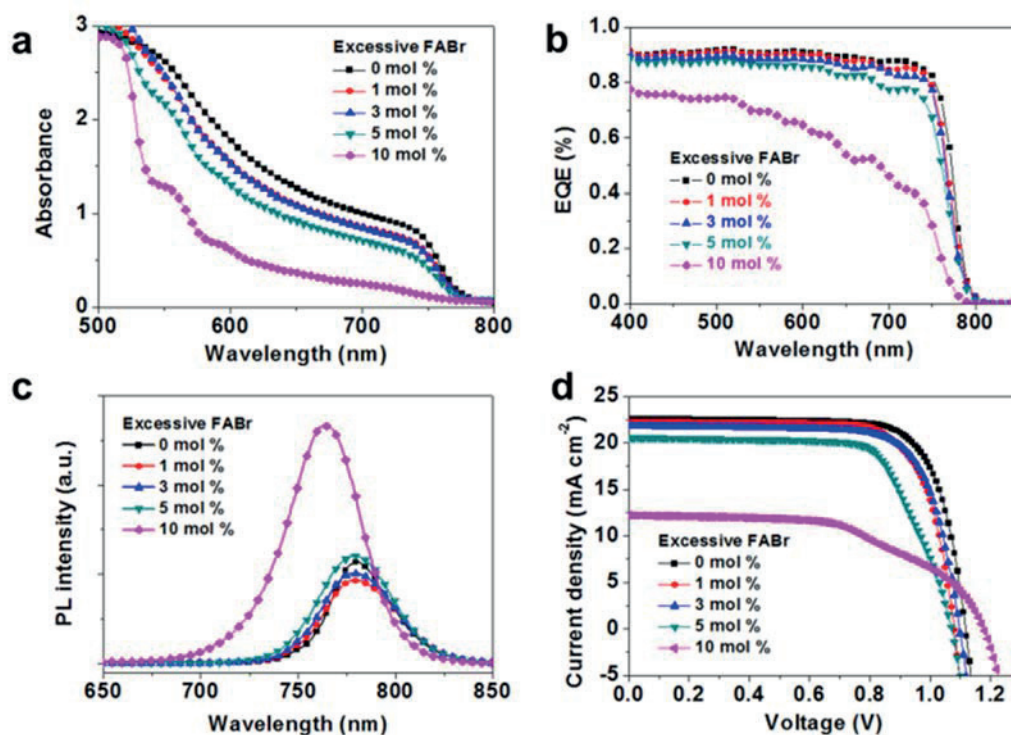


Figure 27 Photo-physical properties and photovoltaic performance observed from the perovskite films treated with FABr solutions (0, 1, 3, 5, and 10 mol %) (a) UV-Vis absorption; (b) EQE and (c) PL spectra for the as prepared samples; (d) $J-V$ curves obtained from devices prepared with the corresponding perovskite films.

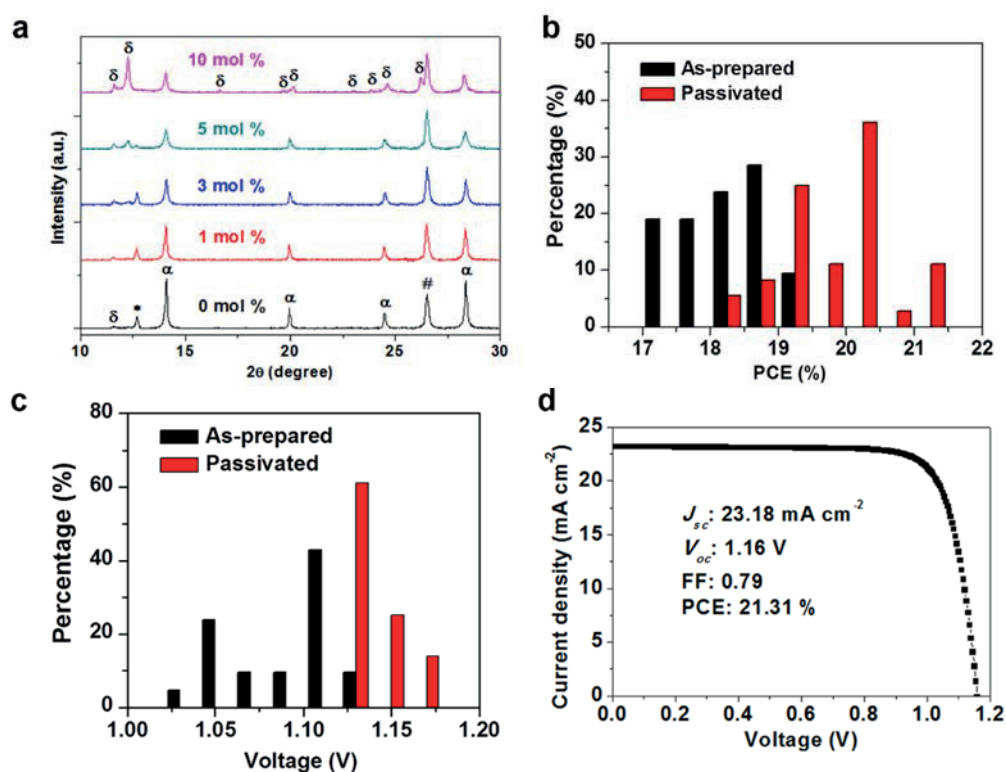


Figure 28 (a) XRD patterns of the perovskite films. α , δ , * and # denote the diffraction peak of α -FAPbI₃ phase, δ -FAPbI₃ phase, PbI₂ and FTO, respectively. Histogram of the PCE distribution (b) and the V_{OC} distribution (c) for devices with as-prepared (20 cells) and passivated perovskite films (40 cells). (d) The J - V curve of the champion cell from the passivated perovskite.

precursor solution affected the performance negatively. In Figure 16a, the perovskite films fabricated from solutions including excess FABr show decreasing absorbance from 1 mol%. Additionally, a dramatic decrease in EQE and a strong blue shifted PL emission peak were also found at increased 10 mol% excess (Figure 27b and c), together with a higher V_{OC} but reduced J_{SC} , probably due to the formation of FAPbBr₃ or FAPbBr_{3-x}I_x. None of the samples where an excess of FABr had been incorporated showed any improvement in PCE (Figure 27d). Finally, we investigated the XRD patterns of the FABr mixed perovskite films (Figure 28a). As the amount of mixed FABr increased, the intensity of PbI₂ and α -FAPbI₃ peaks decreased, while a δ -FAPbI₃ peak became obtrusive gradually.^{31, 33} It is worth noting that PSCs with 1 and 3 mol% excess of FABr show a lower PCE than that of a reference device despite their decreased PbI₂ peak like the passivated perovskite film. It implies that the formation of FAPbBr_{3-x}I_x inside the primary perovskite layer, rather than at the surface, does not have a passivation effect and even remove the beneficial role of PbI₂. As PbI₂ has been reported to enhance the electronic quality and ion migration resulting in higher V_{OC} ,^{32, 43} the decreased PbI₂ content without passivation could be the reason for the lower performance in samples

containing 1 and 3 mol% excess of FABr. Furthermore, decreasing α -FAPbI₃ phase peaks may be another reason for less PCE. Consequently, the higher efficiency obtained from an additional deposition of FABr solution was not achieved by forming a new kind of perovskite with larger E_g , but by introducing the passivation layer at the rear surface between the perovskite and the HTM. As a result, improved efficiencies with PCE average over 20% were obtained, as shown in Figure 28b. When comparing V_{OC} , it is clearly shown that the enhancement in performance is produced by increased V_{OC} , which we associate with the passivation layer (Figure 28c). The J - V curve of the champion cell is also shown in Figure 28d. With backward scanning, the cell exhibited 23.18 mA cm⁻² of J_{SC} , 1.16 V of V_{OC} , 78% of FF and 21.31% PCE under 1 sunlight LED illumination.

3.4. Conclusion

In conclusion, we have investigated and underlined an effect of introducing a passivating layer into a rear surface of a perovskite film for improving the photovoltaic performance. By treating the surface with a FABr solution, superficial PbI₂ was converted into a FAPbBr_{3-x}I_x perovskite layer on top of the perovskite film. Due to its wider bandgap and matched alignment of the conduction/valence band, V_{OC} was boosted without conspicuous dropping of J_{SC} . We verified that electrons were blocked and the reduced charge carrier recombination was resulted from the passivation layer in a gradient perovskite film. Also, it is demonstrated that the improved efficiency is realized by the fabrication of a passivation layer, not by generating a new kind of perovskite within a primary perovskite film. Our findings can broaden the understanding of perovskite solar cells by suggesting a deeper insight into possible solutions through interfacial engineering of perovskite films towards larger V_{OC} .

3.5. Experimental section

3.5.1. Device fabrication

FTO glass (Nippon sheet glass) substrates were sequentially cleaned with the detergent solution, acetone, and ethanol. A compact TiO₂ layer was then coated on the cleaned FTO substrate by spray pyrolysis deposition at 450 °C with a precursor solution prepared by diluting titanium diisopropoxide (Sigma-Aldrich) in ethanol. Mesoporous TiO₂ films were prepared using a diluted TiO₂ paste (Dyesol 30 NR-D) in ethanol solution. Films were spin-coated at 2000 rpm for 20 s, and sintered on

a hot plate at 500 °C for 30 min. After cooling to room temperature, films were treated with 0.1 M Lithium bistrifluoromethanesulfonimide solution (Li-TFSI, Aldrich) in acetonitrile by spin-coating at 3000 rpm for 10 s, and finally baked again at 500 °C for 30 min. The lead excess $(\text{FAPbI}_3)_{0.85}(\text{MAPbBr}_3)_{0.15}$ precursor solution was prepared by mixing FAI (1.1 M), PbI_2 (1.15 M), MABr (0.2 M) and PbBr_2 (0.2 M) in a mixed solvent of DMF : DMSO = 4 : 1 (volume ratio). The solution was then spin-coated at 1000 rpm for 10 s and continuously at 6000 rpm for 30 s. During the second step, 100 μL of anhydrous chlorobenzene was poured 15 seconds before the process was finished. Films were then annealed at 100 °C for 90 min. For the surface passivation treatment, the films were cooled down to room temperature and treated with a FABr solution. 100 μL of FABr solution (5 mg ml^{-1}) were spin-coated on the as-prepared perovskite substrates at 5000 rpm for 30 s, and annealed at 100 °C for 5 min. Finally, Spiro-OMeTAD was spin-coated at 4000 rpm for 20 s. The Spiro-OMeTAD solution was prepared by dissolving in chlorobenzene at 70 mM and adding 4-*tert*-butylpyridine, Li-TFSI in acetonitrile, and $\text{Co}[t\text{-BuPyPz}]_3[\text{TFSI}]_3$ (FK209) in acetonitrile at the molar ratio of Spiro : FK209 : Li-TFSI : TBP of 1 : 0.03 : 0.5 : 3.3. Devices were fabricated with a 70 nm thick gold counter electrode by using thermal evaporation.

3.5.2. Film and device characterization

X-ray diffraction (XRD) analysis was carried out using a Bruker D8 Advance diffractometer in an angle range of $2\theta = 10^\circ$ to 30° . The morphology of the films was characterized using a high-resolution scanning electron microscope (SEM, ZEISS Merlin). The energy dispersive X-ray (EDX) spectra and composition analysis were performed with SEM. It was carried out two days after preparing the films. The absorbance and reflectance were measured with an integrating sphere using UV/Vis/NIR spectroscopy (PerkinElmer Lambda). The photoluminescence dynamics were measured using the Time-Resolved Single Photon Counting (TRSPC) technique that is incorporated into the same Fluorolog-312 spectrofluorometer. The solar cell measurement was done using commercial solar simulators (Oriel, 450 W Xenon, AAA class/Oriel VeraSol-2, LED, AAA class). The light intensity was calibrated with a Si reference cell equipped with an IR-cutoff filter (KG5, Newport), and it was recorded before each measurement. Current–voltage characteristics of the cells were obtained by applying an external voltage bias while measuring the current response using a digital source meter (Keithley 2400/2604). The voltage scan rate was 10 or 25 mV s^{-1} and no device preconditioning such as light soaking, or forward voltage bias applied for a long time, was applied before starting the measurement. The cells were masked with an active area of 0.16 cm^2 to fix the

active area and reduce the influence of the scattered light. EQE was measured with IQE200B (Oriel) without bias light.

Chapter 4. PEAI Passivation

(Selective growth of layered perovskites for stable and efficient photovoltaics)

This chapter is from the article published as the above title in *Energy & Environment Science*, 2018, 11, 952-959.

The permission rule of Energy & Environment Science:

If you are the author of this article you do not need to formally request permission to reproduce figures, diagrams etc. contained in this article in third party publications or in a thesis or dissertation provided that the correct acknowledgement is given with the reproduced material.

If you are the author of this article you still need to obtain permission to reproduce the whole article in a third party publication with the exception of reproduction of the whole article in a thesis or dissertation.

In authors (Kyung Taek Cho, Giulia Grancini, Yonghui Lee, Emad Oveisi, Jaehoon Ryu, Osbel Almora, Manuel Tschumi, Pascal Alexander Schouwink, Gabseok Seo, Sung Heo, Jucheol Park, Jyongsik Jang, Sanghyun Paek, Germà Garcia-Belmonte, Mohammad Khaja Nazeeruddin), I am the first author and developed the main idea and led the experiment.

4.1. Abstract

Perovskite solar cells (PSCs) are promising alternatives toward clean energy because of their high-power conversion efficiency (PCE) and low processing cost. However, their poor photo- and thermal stability issues are still preventing for practical applications. Here we demonstrate an innovative approach to control the surficial growth of a low dimensional perovskite capping layer on top of a bulk three-dimensional (3D) perovskite film. The distinct layered low dimensional perovskite thin film is observed clearly in a form of layer by layer and the influence between a formation of the new perovskite layer and charge recombination are investigated. The photovoltaic cells of layered perovskite exhibited an enhanced PCE of 20.1% on average, when compared to pristine 3D perovskite film. The devices retained 85% of the initial efficiency stressed under one sun illumination for 800 hours at 50°C in ambient environment.

4.2. Introduction

PSCs with over 22% of PCE are attracting extensive interest in renewable energy to deliver low-cost electricity and to reduce carbon dioxide emission ^{2, 44, 45}. However, their commercialization and practical applications are still restricted by insufficient long term stability in ambient atmosphere. Therefore, advances particularly in improving device stability without sacrificing the efficiency is vital for the future of PSCs. One of the reasons of efficiency degradation in PSCs is attributed to unstable perovskite materials itself composed of small organic cations (A^+), metal cations (B^{2+}) and halide anions (X^-), which form a three-dimensional (3D) crystal structure of ABX_3 ⁴⁶⁻⁴⁸. To improve structure stability, various cations, formamidinium (FA^+), cesium (Cs^+), rubidium (Rb^+), and anions, bromide (Br^-), and chloride (Cl^-) have been explored for mixed 3D perovskites; $[FA/MA]Pb[I/Br]_3$ ⁴⁹, $[FA/Cs]Pb[I/Br]_3$ ^{50, 51}, or $[Rb/Cs/FA/MA]Pb[I/Br]_3$ ⁵².

To overcome the limited stability of the 3D perovskites, two-dimensional (2D) perovskites have been suggested due to their superior stability but at the expense of efficiency ^{53, 54}. The 2D perovskite is formed when the size of the cation (A^+) is large enough to isolate anionic metal layers in the 3D perovskite phase. Although the recent Ruddlesden-Popper layered perovskite using *n*-butylammonium carried the PCE up to 12.5% ⁵⁵, it suffers from lower PCE than that of the former 3D structure of mixed perovskite ^{31, 56, 57}. Here, we developed a strategy of controlled growth of a 2D perovskite overlayer on a 3D perovskite to take advantage of both high efficiency of 3D and stability of 2D perovskite. This approach conceptually differs from previous studies mixing 3D and

2D perovskite together by adding bulky cations homogeneously in perovskite precursors^{53, 58-61}. Indeed, by controlling the deposition parameter, the distinct 2D perovskite capping layer is obtained on top of the 3D perovskite film in a form of layer by layer. When embodied in the photovoltaic cells, this leads to a maximum PCE of 20.7%, representing a giant step forward with respect to recent results mixing 3D and 2D perovskite⁶¹. The efficiency remained 85% of the initial value after 800 hours of maximum power point tracking under full illumination at 50°C temperature in ambient condition (30–60% relative humidity).

We employed phenylethylammonium iodide (PEAI) to obtain a 2D perovskite (PEA₂PbI₄) thin layer. The PEA⁺ bulky cation has a large molecular radius that causes anionic layers in 3D architecture to be isolated and transform to the 2D perovskite^{60, 62, 63}. In particular, the PEA⁺ was demonstrated to improve the phase stability in FAPbI₃ when a small amount of PEA⁺ was added as quasi-3D FA_xPEA_{1-x}PbI₃ perovskite⁶⁴ and the change of valence band in (PEA)₂MA_{n-1}Pb_nI_{3n+1} was very negligible⁶⁵, which is expected to have a little influence on hole transfer. However, different from typical methods of mixing cations together, we attained the surficial growth of 2D perovskite overlayer on top of 3D perovskite by dynamic spin coating of the PEA⁺ isopropanol (IPA) solution on an optimized lead excess pristine Cs_{0.1}FA_{0.74}MA_{0.13}PbI_{2.48}Br_{0.39} (CFMPIB) perovskite film. This technique can reduce the impact of the IPA solution on permeating to the pristine perovskite films and provide the thin PEA⁺ film uniformly. For the pristine CFMPIB perovskite film, we exploited a lead excess stoichiometric ratio of a precursor perovskite solution (FAI:PbI₂ = 1:1.05) due to its positive effect on reducing defects in perovskite films^{32, 43}, and it was also aimed to be used for reacting with PEA⁺. The final perovskite film after annealing process is called L-CFM/P (layered perovskite with CFMPIB and quasi-PEA₂PbI₄).

4.3. Results and discussion

4.3.1. Growth of the 2D perovskite thin layer and characterization

Figure 29A shows X-ray diffraction (XRD) spectra of the CFMPIB and the L-CFM/P films coated on TiO₂/FTO substrates. In the pristine CFMPIB perovskite film, the PbI₂ peak (12.7°) is observed demonstrating the presence of excess lead iodide in CFMPIB precursor solution, as well as a δ -phase of FA-based perovskite. However, when the PEA⁺ IPA solution (10 mg/ml) was coated on the CFMPIB film and annealed, the PbI₂ and δ -phase peaks disappeared and new peaks at 5.44°, 10.8°,

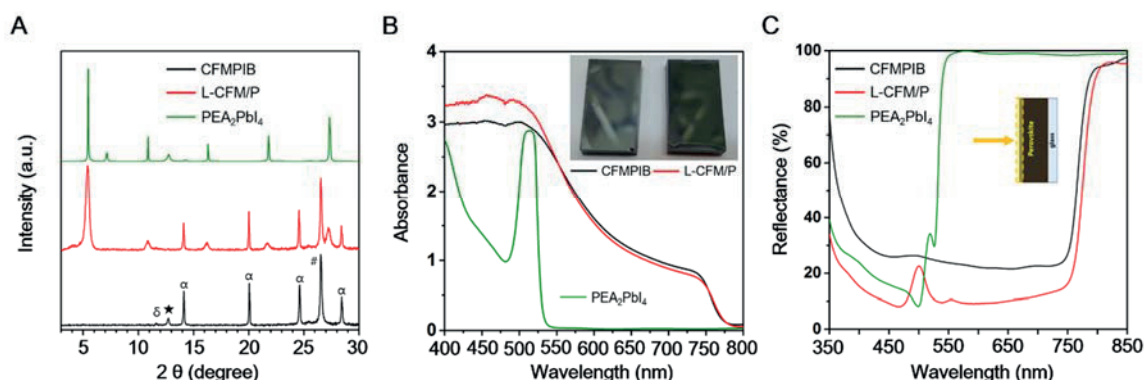


Figure 29 Characterization of CFMPIB ($\text{Cs}_{0.1}\text{FA}_{0.74}\text{MA}_{0.13}\text{PbI}_{2.48}\text{Br}_{0.39}$), L-CFM/P (PEA_2PbI_4 layered on CFMPIB), and PEA_2PbI_4 perovskite. (A) XRD data, (B) UV-Vis spectra, (C) diffuse reflectance spectra of these three perovskite films. In XRD spectra, α , δ , \star and # denote diffraction peaks corresponding to the α , δ phase of FAPbI_3 based perovskite, PbI_2 and FTO, respectively. The intensity for PEA_2PbI_4 perovskite was reduced by a factor of 500 to put in a same figure with other perovskites. The inset images in (B) show photo images of CFMPIB and L-CFM/P films. All of perovskite films examined for these measurements were prepared as coated on mesoporous TiO_2 /compact TiO_2 /FTO substrates

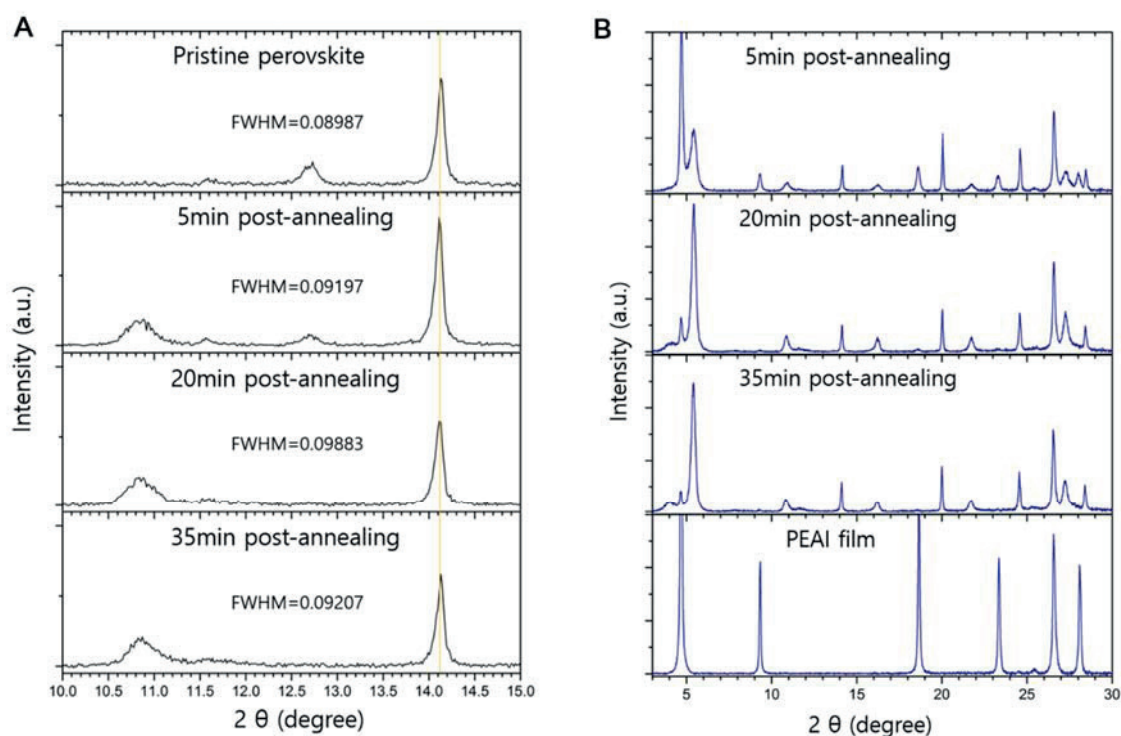


Figure 30 A) Magnified XRD data of region around 14° , the main 3D CFMPIB perovskite peak, as annealing time after spin coating PEAI isopropanol solution (10 mg/ml). Full-width at half-maximum of these CFMPIB perovskite peaks at 14.1° were calculated and listed. B) XRD spectra for L-CFM/P perovskite films varying annealing time (5, 20, and 30 min) and a PEAI film deposited on a TiO_2 /FTO substrate by spin coating PEAI solution (15 mg/ml).

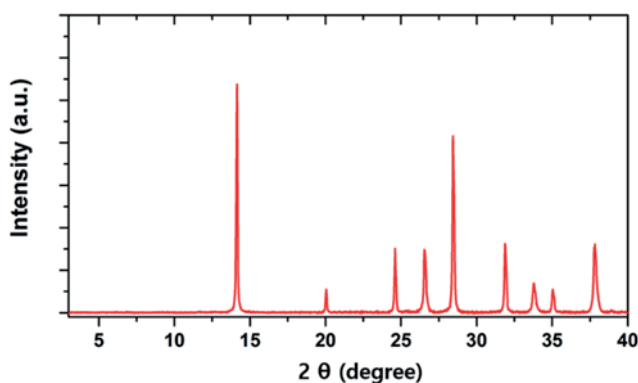


Figure 31 XRD spectra of a CFMPIB+PEAI perovskite film. For the CFMPIB+PEAI film, another precursor solution was prepared by adding PEAI to the CFMPIB precursor solution, where the amount of PEAI was same to the excess molar ratio of PbI_2 in the CFMPIB solution. The final composition of precursor solution was $\text{PEA}_{0.05}\text{Cs}_{0.1}\text{FA}_{0.73}\text{MA}_{0.13}\text{PbI}_{2.53}\text{Br}_{0.39}$. The perovskite film was fabricated by following same procedure for the CFMPIB perovskite film.

16.3°, 21.7° and 27.3°, appeared. We prepared a reference PEA_2PbI_4 film and measured the XRD data. A comparison of peak positions proved newly formed perovskite is consistent with PEA_2PbI_4 phase^{62, 64}. Despite of constructing the 2D perovskite, the other peaks for mixed 3D perovskite scarcely modified on intensities and positions. For the (111) crystal plane of the main 3D perovskite phase, the 2θ around 14° was zoomed and the full-width at half-maximum (FWHM) of the CFMPIB and the L-CFM/P were estimated in Figure 30A. Whereas the PEA_2PbI_4 peak at 10.8° increased and the PbI_2 peak at 12.7° disappeared when the films were heated, the main CFMPIB perovskite peak at 14.1° was neither shifted nor reduced. This change represents a PEA_2PbI_4 perovskite was generated separately in the CFMPIB perovskite film. In Figure 30B, a strong peak at 4.69° revealing PEAI was reduced as the heating time increased. We fabricated additional perovskite film from a solution including the CFMPIB precursor and PEAI together, where the amount of added PEAI was matched the excess molar ratio of PbI_2 in the CFMPIB precursor solution ($\text{FAI}:\text{PEAI}:\text{PbI}_2 = 1:0.05:1.05$). In Figure 31, the PbI_2 peak was not detected in the XRD data like the L-CFM/P film. Quite differently, however, the peak of PEA_2PbI_4 in the region around 5° was not appeared indicating either buried a little 2D perovskite in the bulk or not formed highlighting that only spin-coating PEAI solution on pristine CFMPIB perovskite films can produce the 2D perovskite.

After spin coating the PEAI solution, the color of the L-CFM/P film changed to dark green compared to the pristine CFMPIB film, as presented photo-images of pristine CFMPIB and L-CFM/P perovskite films in the inset in Fig. 1B. We measured Ultraviolet-Visible (UV-Vis) absorption and the reflectance spectra of CFMPIB, L-CFM/P, and $\text{PEAI}_2\text{PbI}_4$ perovskite films (Figure 29B and 1C). The slight redshift of the band edge is visible when forming 2D perovskite. It is an agreement with the literature⁶⁴, where the addition of small amount PEAI to mixed 3D perovskite shows slight redshift of absorption while the large amount leads to

the blue-shifted absorption. The greenish color of L-CFM/P can be consistent with a small hump at 500 nm in reflectance spectra, showing an independent perovskite emitting a green light was created.

The photoluminescence (PL) of CFMPIB and L-CFM/P perovskites was carried out from the top of perovskite and bottom of TiO₂ (Figure 32A, 32B and Figure 33). We used an excitation light of 450 nm which has a penetration depth less than 100 nm^{26, 66}. That implies these PL emission are correlated with thin layers at top and bottom of perovskite, respectively. For CFMPIB, the PL peaks appeared at 759 nm and 775 nm by exciting on the top surface and the bottom interface of the perovskite film, respectively. The small difference in the peak maxima might be due to the different perovskite crystal size when confined in the mesoporous-TiO₂ structure⁶⁷, these PL peaks are attributable to same pristine CFMPIB perovskite. On the other hand, strikingly the L-CFM/P film shows a different behavior comparing between top and bottom emission of perovskite film. From the top surface of the L-CFM/P film, a strong peak at 508 nm and a weak peak at 765 nm were measured, while from the TiO₂ side only one peak at 776 nm was observed. The peak at 508 nm from top side is derived from the newly formed 2D perovskite having a large bandgap, and it is consistent with XRD data. Thus, it is determined that the 2D perovskite was formed only at the top of perovskite film. It is noted that the thickness of this PEA₂PbI₄ perovskite layer is very thin or the partial 3D pristine perovskite was remained as unreacted because of the presence of the small peak at 765 nm indicating CFMPIB perovskite in PL spectra of the top side. The pristine perovskite phase was barely affected by PEAI treatment, except the modification of top layer to 2D perovskite film. We also conducted XRD analysis with fixed x-ray incident angles at 0.3°, 2° and 5° to elucidate the

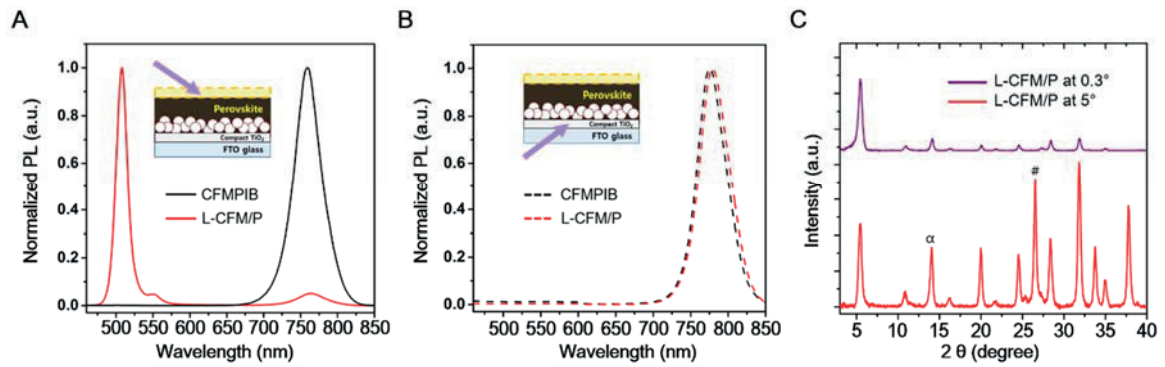


Figure 32. Comparison of photoluminescence emission spectra of CFMPIB and L-CFM/P perovskites. (A and B) Steady-state normalized PL spectra excited with a laser of 450 nm from top surface of perovskite films (A) and bottom of perovskite films (B). Non-normalized PL of CFMPIB, L-CFM/P, and PEA_2PbI_4 is shown in Fig. S4. (C) XRD data for L-CFM/P film at X-ray incident angle of 0.3° (for surface) and 5° (for interior). α and # denote diffraction peaks corresponding to the α phase of FAPbI_3 based perovskite and FTO, respectively.

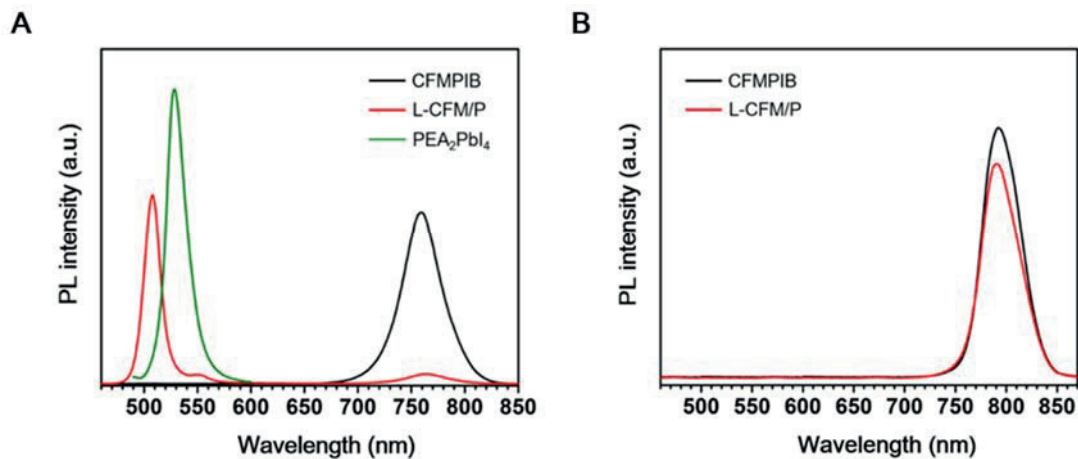


Figure 33. Steady-state PL spectra of CFMPIB, L-CFM/P, and PEA_2PbI_4 perovskite films. The intensity was not normalized and the PL emission peaks were obtained from top surface (A) and bottom side (B) of perovskite films. When prepared samples for (B), the perovskite films are coated on microscope glass for removing a quenching effect.

structure of surface and internal perovskite layers (Figure 32C and Figure 34).⁶⁸ At a lower angle of incident beam, the XRD data are dominated more by top of perovskite layers. Moving the incident angle from 0.3° to 5° , the relative intensity of the signal corresponding to internal 3D perovskite phase (14.1°) increased substantially in the L-CFM/P layer. The change from the surface to full depth diffractions reflects that the formation of PEA_2PbI_4 likely occurred on the surface of perovskite films and it is accordance with PL emission measurement.

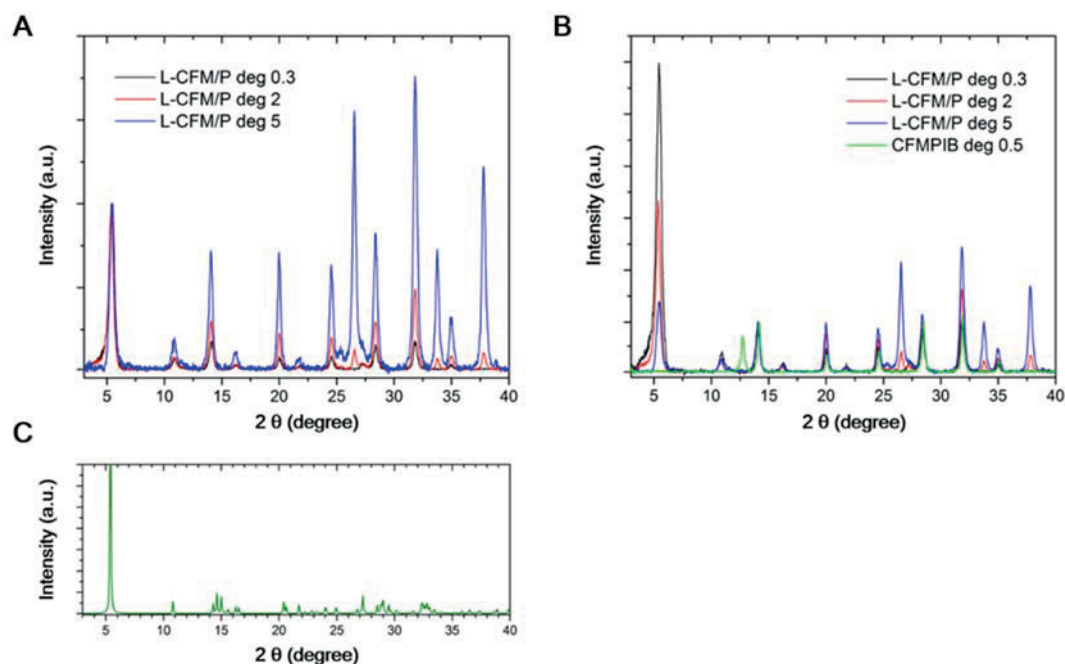


Figure 34. XRD measurement at fixed incident X-ray angle of 0.3° , 2° , and 5° . (A) XRD data were normalized to a main 2D perovskite (PEA_2PbI_4) peak of 5.44° 2θ . The relative signal intensity of the 3D phase at 14.1° increases with the incidence angle (blue - red - green curves). This indicates that the 2D perovskite is concentrated rather around the surface. Although we cannot tell how the layer is thick, it can be evidence that it is present in surface vicinity. (B) XRD data were normalized to a main 3D perovskite peak of 14.1° . (C) Calculated XRD data from PEA_2PbI_4 crystallographic information file obtained from a reference.

4.3.2. Device structure, charge transfer, and charge recombination.

We fabricated the mesoscopic perovskite solar cells with the pristine CFMPIB perovskite and the L-CFM/P perovskite. Both of devices have the same architecture (fluorine doped tin oxide/ compact and mesoporous TiO_2 / perovskite/ spiro-OMeTAD/ gold) except using different perovskite films. The top view scanning electron microscopy (SEM) images of perovskite films revealed stark differences between before and after PEAI coating (Figure 35A). The pristine CFMPIB perovskite film deposited on top of mesoporous TiO_2 layer showed a compact, pinhole free, and large grains having distinct grain boundaries like a rock wall. However, the forming 2D perovskite on top of the perovskite layer changed to more homogeneous and smoother films, and grain boundaries were reduced. The mitigated grain boundaries indicate decreased defects in perovskite layer, leading relieved charge recombination. Atomic force microscope (AFM) measurement was examined to further scrutinize the surface of the perovskite film (Figure 36). The root mean square roughness (R_q) value decreased after spin-coating PEAI and annealing, from 25.01 nm to 18.76 nm. In

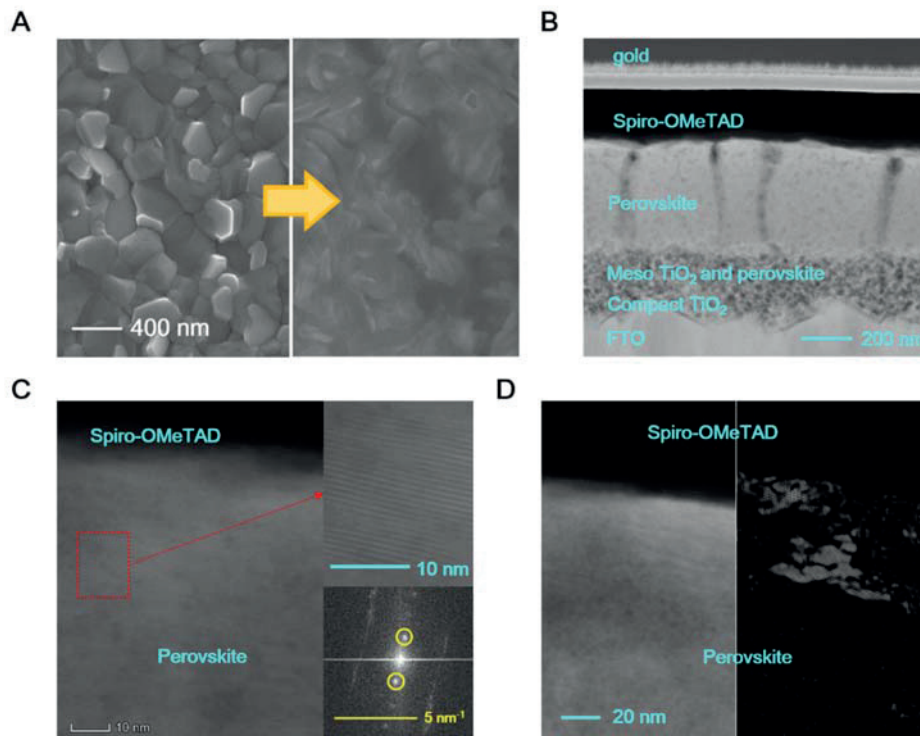


Figure 35. Morphologies of the perovskite film and PSCs with CFMPIB and L-CFM/P. (A) Top-view scanning electron microscopy (SEM) images of the CFMPIB film (left) and the L-CFM/P film (right). (B) Cross-sectional STEM HAADF image of a complete device fabricated with L-CFM/P. (C) HR-STEM HAADF image from the surface region of L-CFM/P along with a magnified view in the right top inset. A fast Fourier transform (FFT) image of this grain is displayed in the bottom inset. (D) Inverse FFT from yellow spots in the FFT and the corresponding STEM HAADF image.

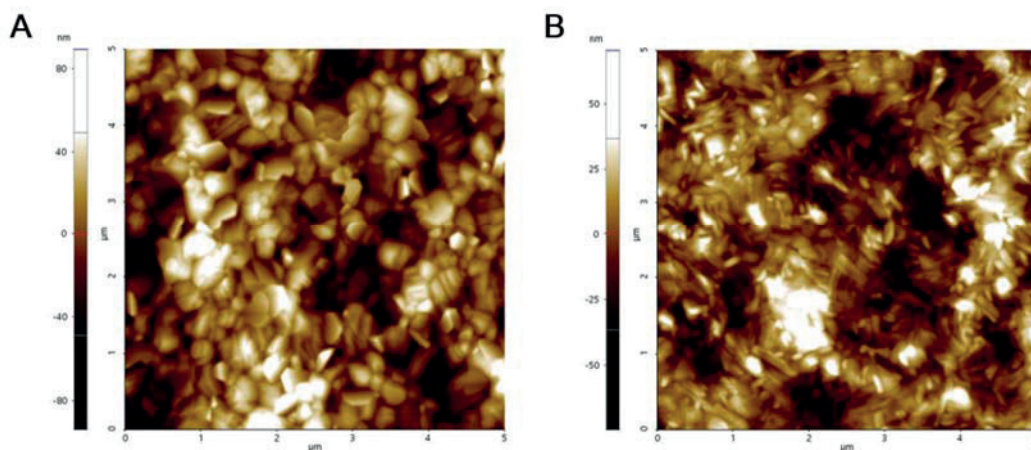


Figure 36. Comparison on roughness of perovskite films from typical AFM measurement. The AFM images of CFMPIB (A) and L-CFM/P (B) are taken as $5 \times 5 \mu\text{m}^2$.

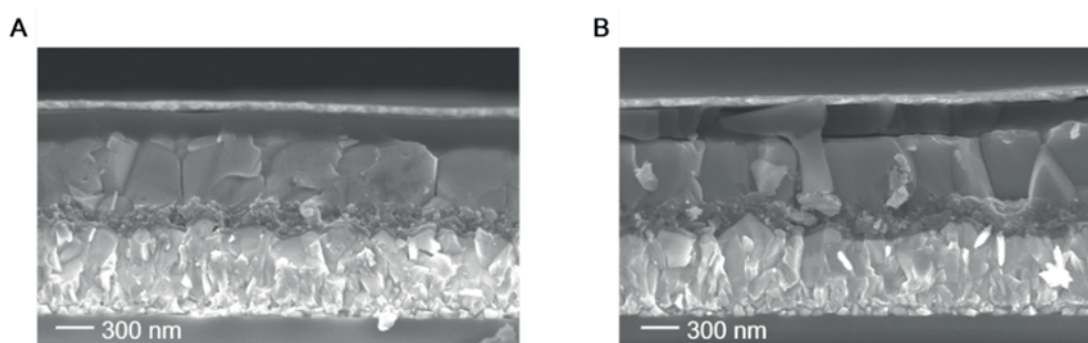


Figure 37. Cross-sectional SEM images of the complete devices fabricated with CFMPIB (A) and L-CFM/P (B).

contrast to the variation on top surfaces of perovskite films, a cross-sectional SEM images of them displayed no distinct difference (Figure 37). This change of morphology processed, especially, at the top surface of the perovskite film and thin 2D perovskite layer was newly formed.

To elucidate the difference between surface and internal layers, high-resolution scanning transmission electron microscopy (HR-STEM) of a cross-sectioned whole L-CFM/P device was carried out and are shown in Figure 35B. The magnified view in Figure 35C exhibits a region close to the surface having a different structure and distinct fringes compared to the middle of the perovskite layer. To visualize clearly the structure difference at the top surface layer, we obtained a fast Fourier transform (FFT) pattern corresponding to this lattice fringe in right bottom inset in Figure 35C and generated an inverse FFT image of the marked reflection as shown in Figure 35D. White patterns, indicating same structure, at the top of the perovskite layer implies that our approach leads to form the thin 2D perovskite layer effectively with quite distinct interface.

After building the thin 2D perovskite layer on CFMPIB films, the creation of band offset inside perovskite films is expected to cause an increase of charge transfer of photo-generated electrons to TiO_2 and to block the charge recombination at the interface of perovskite/hole transporting layer (HTL) under illumination⁶⁹. Based on Tauc plot (Fig. S8) and ultra-violet photoelectron spectroscopy (UPS) shown in Figure 38A, the energy level diagram of L-CFM/P was illustrated in Figure 38B. Considering the valence level coherence between the CFMPIB and PEA_2PbI_4 perovskite, the holes in the CFMPIB layer were expected to move to HTL without any impediment. However, the photo-excited electrons in a conduction band of

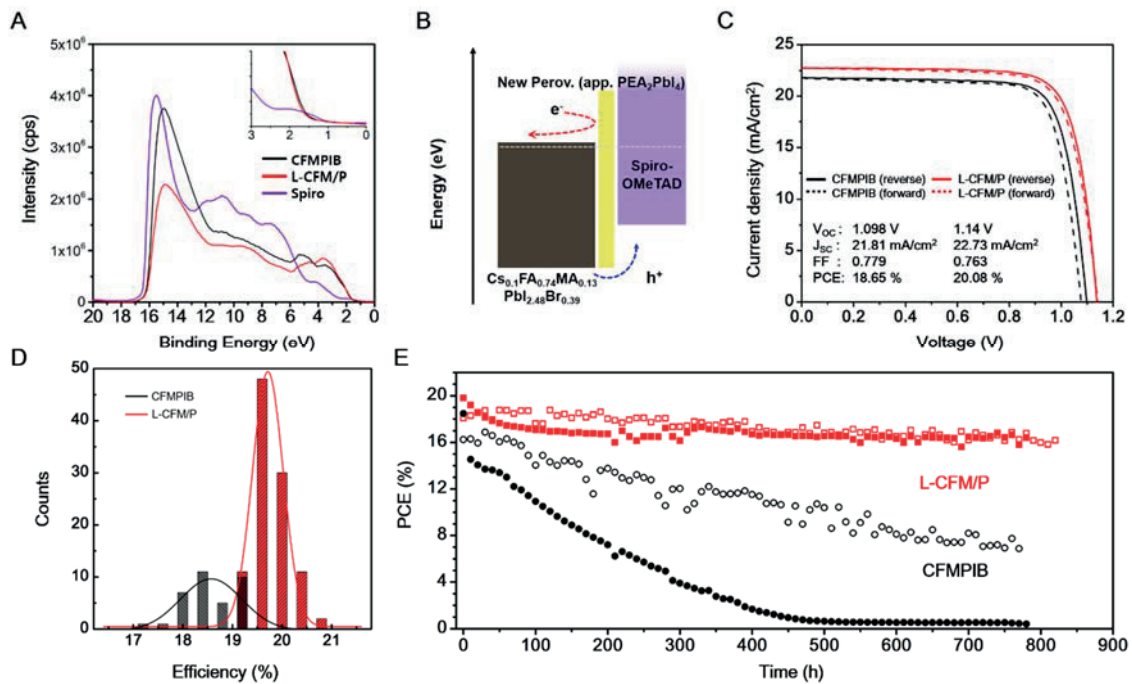


Figure 38. Energy level diagram and photovoltaic performance of PSCs with CFMPIB and L-CFM/P. (A) Ultra-violet photoelectron spectroscopy (UPS) for CFMPIB, L-CFM/P, and spiro film. For UPS measurement, each film, such as CFMPIB, L-CFM/P, and spiro-OMeTAD (on L-CFM/P), was prepared on FTO/compact and mesoporous TiO_2 /like real devices. (B) Energy band diagram of the L-CFM/P device and description of how the 2D perovskite capping layer improved the PCE. At the rear region of the perovskite film, the new 2D perovskite having a wide band gap can block transfer of excited electrons to the HTM layer. The band gap of perovskites is determined from the PL measurement and Tauc plot (Fig. S8, ESI[†]). (C) J - V curves and hysteresis of PSCs at a scan rate of 25 mV s^{-1} . (D) Histograms of the PCEs. (E) Photo-stability test from maximum power point tracking under 800 h continuous illumination of full intensity in an inert gas (blank ones) and ambient (filled ones) environment with encapsulated glass.

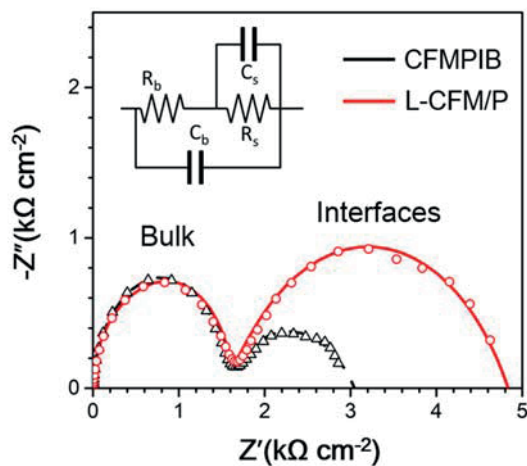


Figure 39. Open circuit impedance spectra with clear differences toward the low frequency range. The solid lines are fitted to the equivalent circuit of the inset. R_s and R_b represent resistance at surface and bulk, C_s and C_b represent capacitance at surface and bulk, respectively.

CFMPIB would be prevented from diffusing to HTL because of higher conduction energy level of PEA_2PbI_4 .

To investigate the charge transfer kinetics within perovskite films, impedance spectroscopy on both of samples was performed (Figure 39). In Nyquist plot under the same open circuit voltage (880 mV), the L-CFM/P device showed the bigger low-frequency arc than the CFMPIB cell, where this arc in the low-frequency is associated with the interface charge recombination process^{70, 71}. The recombination resistance, obtained from the fitting of the arcs to the equivalent circuit model of inset of Figure 39, increased twice from the CFMPIB to the L-CFM/P based devices. The reduced charge recombination can be explained by improved charge transfer. As shown in time resolved PL decay probed at 770 nm on the perovskite surface with different pulse fluence (Figure 40 and Table 2), the L-CFM/P showed a little faster decay in PL lifetime than the pristine CFMPIB film at initial decay rate, where electron-hole bimolecular recombination are dominated⁷². However, we observed similar behaviors for two perovskite layers at a system dictated by traps or defects density (Figure 41)⁷². Thus, a slight quenching was induced by restraining the interfacial charge recombination from inside CFMPIB perovskite to the top PEA_2PbI_4 layer, as demonstrated by the impedance spectra⁷³. The slowing recombination derived from introducing 2D perovskite interlayer can be confirmed by enhanced V_{OC} and performance.

4.3.3. Device performance and stability

The effect of this strategy was proved in photovoltaic performance of complete devices. Fig. 4C presents the current density-voltage (J-V) curves and hysteresis of devices with pristine CFMPIB and L-CFM/P perovskite films. Both of cells showed negligible hysteresis. We fabricated more than 100 PSCs with L-CFM/P, and the PCEs are summarized in the histogram (Figure 38D) and statistical data (Figure 43). The devices with 3D/2D perovskite films presented improved efficiencies with a high degree of reproducibility. The best performing device with L-CFM/P achieved 1.15 V open-circuit voltage (V_{OC}), 22.73 mA cm^{-2} short-circuit current (J_{SC}), and 0.794 fill factor (FF), yielding a PCE to 20.75%. We recorded the corresponding incident photon conversion efficiency (IPCE) of each PSCs (Figure 42). Although both of devices show high IPCE, the device employing the passivating 2D perovskite layer has a little higher efficiency than that of the pristine perovskite device in the whole wavelength range from 400 nm to 800 nm. The integrated J_{SC} values from IPCE curve

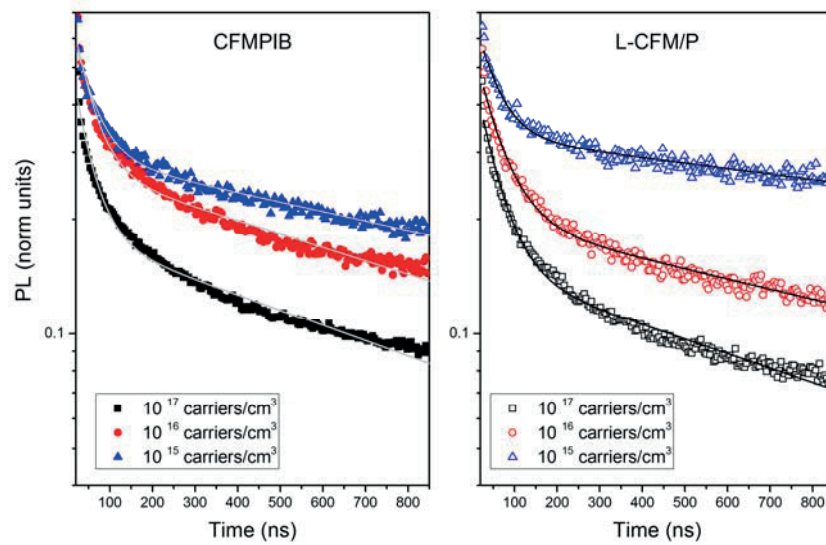


Figure 40. Time-resolved PL decays of CFMPIB and L-CFM/P perovskite films at different excitation densities from 10^{15} to 10^{17} carriers/cm³. Samples have been encapsulated with a glass slide to prevent any oxygen induced degradation. The measurement was carried out by monitoring the PL from the top side of perovskite films at 770 nm.

Table 2. Decay lifetime from PL fitting in Figure 40

	10^{15} carrier/cm ³		10^{16} carrier/cm ³		10^{17} carrier/cm ³	
	τ_1	τ_2	τ_1	τ_2	τ_1	τ_2
CFMPIB	36	790	41	>800	34	>800
L-CFM/P	29	749	31	>800	33	>800

with AM1.5G solar spectrum are agreement with the values obtained from J-V measurement. We found the L-CFM/P can be feasible on various ETLs or configuration by testing on the passivated planar SnO₂ ETL (Figure 44) ⁷⁴.

As the effect of capping 2D perovskite layer, we examined the long-term stability test of the 2D perovskite containing films under dark storage and continuous illumination. Firstly, for storage without continuous illumination, the L-CFM/P enhanced device stabilities compared to the pristine CFMPIB perovskite (Figure 45) and maintained the initial PCE of 20%, while one with pristine CFMPIB was decreased gradually. Figure 38E presents maximum power point tracking (MPPT) of the CFMPIB (black) and L-CFM/P (red) PSCs for 800 hours stressed at 50°C under continuous illumination of full intensity in an argon atmosphere (blank)

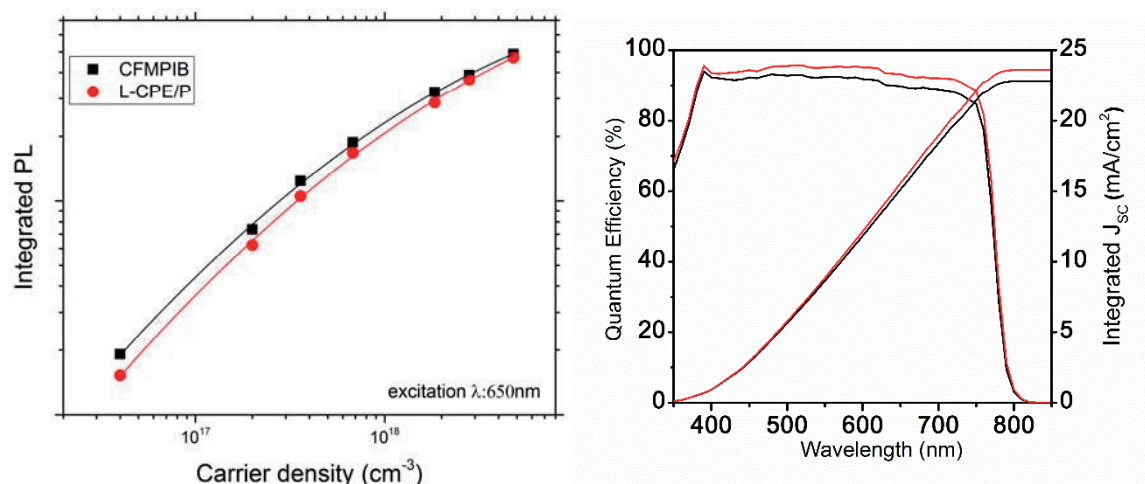


Figure 41. Time integrated Photoluminescence signal for the two perovskite as indicated in the legend as a function of the injected carrier density (cm^{-3}). Below 10^{17} cm^{-3} the integrated PL grows quadratically. So, the growth of PL signal with increasing pump fluence is dominated to the bimolecular radiative recombination rate; for the weak pulse fluence corresponding to injected carrier density, the rate of carrier trapping is faster than the radiative recombination. However, when this latter becomes faster than trapping at above 10^{17} cm^{-3} , the PL signal saturates and quantum yield (integrated PL/pulse fluence) will decrease by resulting from non-radiative recombination. In here, two perovskite films show similar behaviours at saturation point and the rate of growth. We can conclude the effect of trap density in two perovskite will be little difference.

Figure 42. IPCE spectrums and integrated J_{sc} from IPCE.

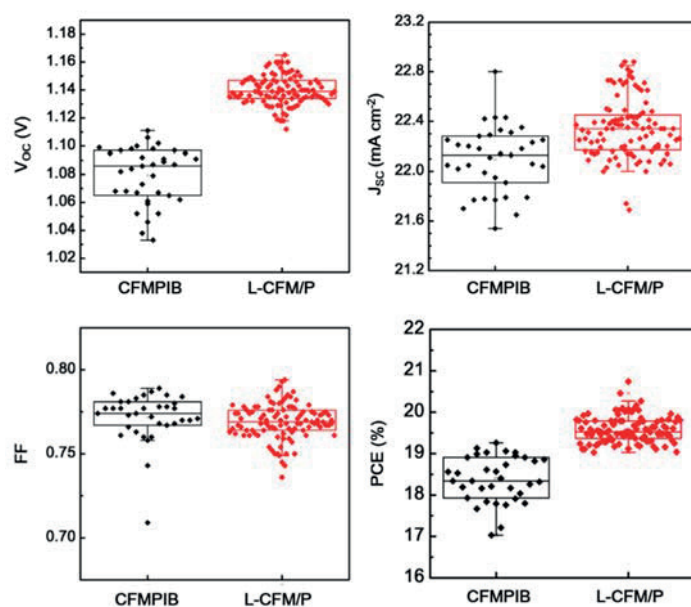


Figure 43. Statistics of V_{oc} , J_{sc} , FF, and PCE of devices more than 100. Showing that the main reason behind upgrading PCE lies in the V_{oc} improved from 1.08 to 1.14 V, which can be associated with a significant recombination reduction. With respect to the J_{sc} , a scattered $\sim 0.2 \text{ mA cm}^{-2}$ larger photocurrents were obtained for 2D/3D structures.

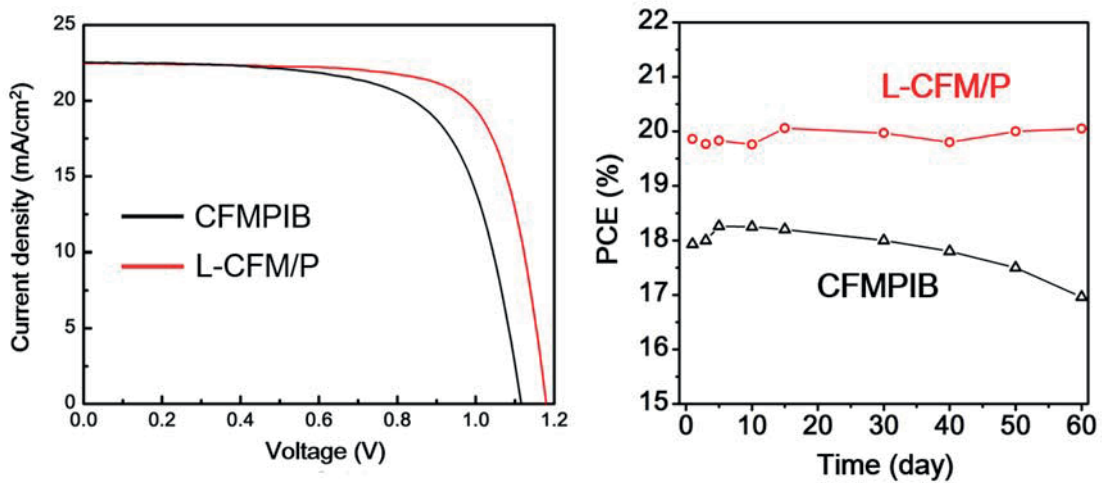


Figure 44. J-V curves of devices based on SnO₂ with CFMPIB and L-CFM/P perovskite.

Figure 45. Dark storage stability of devices with CFMPIB and L-CFM/P. All of cells are stored in dark and measured in ambient atmosphere.

and an ambient condition (filled), where the relative humidity stayed between 30% and 60% without controlling. The L-CFM/P devices displayed impressive improved stability even at 50°C temperature in air, retaining 90% of the initial PCE after 800 hours in the inert gas condition and 85% in humid environment with encapsulation. However, the devices based on pristine 3D perovskite showed the faster degradation of performance.

The small initial drop and continuous degeneration of devices could also be addressed by organic charge transport materials. However, despite spiro-OMeTAD used in these PSCs as HTM, which is known for instability due to dopants, metal electrode diffusion, and morphological decomposition^{52, 75}, the L-CFM/P cells showed surprising stable performance even at 50°C. Thus, it should be noted that 2D perovskite capping layer between perovskite and HTM can minimize the negative effects of the organic HTM as a buffer layer. The stability improvement can be also confirmed without encapsulation in flowing constant humid air gas, 40 ± 5RH% (Figure 46). Although both of device performances decayed faster absolutely than in inert gas due to main reasons related with the organic HTM, the relative stability in PEAI treated perovskite solar cells was enhanced in comparison with the control pristine device.

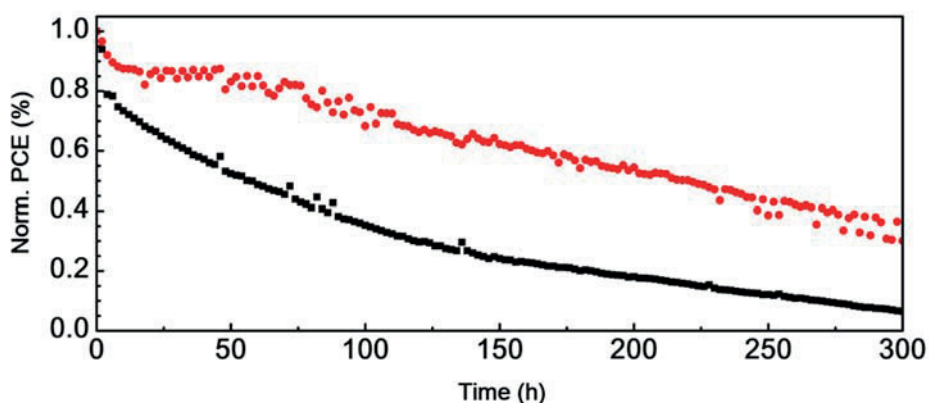


Figure 46. PCE tracking from J-V measurement for 300 h of unencapsulated devices with CFMPIB (black) and L-CFM/P (red) under continuous flowing humid air gas and full-sun illumination.

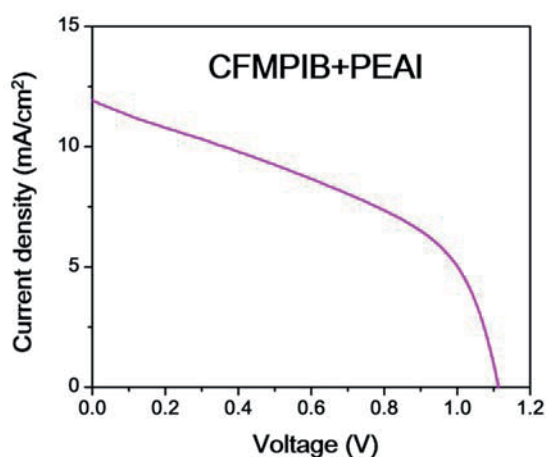


Figure 47. J-V curve of a homogeneous perovskite mixture of CFMPIB+PEAI device.

We also prepared another device using a precursor solution including with CFMPIB and PEAI, examined for XRD spectra comparison (Figure 47). Incorporating PEAI within the perovskite film homogeneously exhibited a dramatic drop in performance.

4.4. Conclusions

In conclusion, our strategy demonstrates an innovative method to engineer interfaces and direct the growth of a low dimensional perovskite which leads to improved stability and efficiency when employed in solar cells. Different from simply mixing low dimensional perovskite precursor cations, we modified the surface of the perovskite film to obtain a distinct lower dimensional – 2D – perovskite at the top surface. A different perovskite layer with a clear interface is observed and identified by optical and structural characterization comparing the surface and the bulk. In addition,

the wide band gap of the newly grown perovskite at the interface between the hole transporting layer and the absorbing layer leads to favored hole transfer, possibly reducing the charge recombination and overall resulting in enhanced efficiency. In conclusion, our investigation opens the possibility of controlling the growth of a layer by layer perovskite by low-cost solution processing. Most significantly, the presence of such low dimensional perovskite layer results in the improvement of the device stability. This approach can be generalized as a standard route to optimize perovskites for long term stability maintaining high efficiency, pushing the perovskite technology in the market, for photovoltaics and beyond.

4.5. Experimental methods

4.5.1. Materials

Formamidinium iodide (FAI) and methylammonium bromide (MABr) were purchased from Dyesol. Lead iodide (PbI_2) and lead bromide (PbBr_2) were obtained from TCI. Cesium iodide (CsI) was purchased from GmbH. Phenylethylammonium iodide (PEAI) was synthesized.²¹ 10 ml of phenylethylamine was diluted in 20 ml of anhydrous ethanol and cooled in an ice bath. With vigorous stirring, 20 ml of HI (55 wt% in H_2O , Sigma Aldrich) was slowly added dropwise. After stirring for 20 min, a colorless precipitate was filtered. The precipitate was washed with diethyl ether and dissolved in methanol twice. To obtain pure white crystals, the PEAi precipitate was recrystallized twice and stored in a vacuum oven overnight to dry.

4.5.2. Perovskite solar cell fabrication

FTO glass substrates (Nippon sheet glass) were sequentially cleaned with detergent solution, acetone, and ethanol. And then by spray pyrolysis deposition, a compact TiO_2 layer was coated on the cleaned FTO substrate heated at 450 °C. The precursor solution was prepared by diluting titanium diisopropoxide (Sigma-Aldrich) in ethanol (0.6 ml : 10 ml). After cooling, a mesoporous TiO_2 film was prepared by coating a diluted TiO_2 paste (Dyesol 30 NR-D) solution in ethanol. Right after spin-coating at 2000 rpm for 20 s, the substrates were sintered on a hot plate at 500 °C for 30 min. For doping Li on TiO_2 , the films were treated with 0.1 M lithium bistrifluoromethanesulfonimide solution (Li-TFSI, Aldrich) in acetonitrile by spin-coating at 3000 rpm for 10 s, and were finally baked at 500 °C for 30 min again. The lead excess $(\text{FAPbI}_3)_{0.85}(\text{MAPbBr}_3)_{0.15}$ precursor solution was

prepared by mixing FAI (1.1 M), PbI₂ (1.15 M), MABr (0.2 M) and PbBr₂ (0.2 M) in a mixed solvent of DMF : DMSO = 4 : 1 (volume ratio). Another 1.15 M solution of CsPbI₃ was also prepared in DMF : DMSO (with the same volume ratio). For triple cation mixed perovskite solution, (FAPbI₃)_{0.85}(MAPbBr₃)_{0.15} and CsPbI₃ solutions were mixed in 10 vol% ratio. The solution was then spin-coated at 1000 rpm for 10 s and continuously at 4000 rpm for 30 s in a nitrogen glove box. After entering the second step, 100 µl of anhydrous trifluorotoluene was poured 15 seconds before the completion of the process.³⁷ Films were then annealed at 100 °C for 60 min. For forming an additional 2D perovskite film on top of this perovskite film, cooled substrates were treated with a PEAI isopropanol solution. 100 µl of PEAI solution (15 mg ml⁻¹) were spin-coated on the as-prepared perovskite films at 4000 rpm, which is similar to the anti-solvent dropping method. Finally, spiro-OMeTAD was spin-coated at 4000 rpm for 20 s. A 70 mM spiro-OMeTAD solution was prepared by dissolving in chlorobenzene with 4-*tert*-butylpyridine, Li-TFSI in acetonitrile, and Co[*t*-BuPyPz]₃[TFSI]₃ (FK209) in acetonitrile at a molar ratio of spiro : FK209 : Li-TFSI : TBP of 1 : 0.03 : 0.5 : 3.3. Devices were completed with thermal evaporation of a 70 nm thick gold counter electrode.

For devices based on the planar SnO₂ ETL, compact TiO₂/FTO substrates were prepared as explained previously for mesoporous TiO₂. A PTO layer was prepared by spin-coating a precursor solution of SnCl₄ (Acros) dissolved in water. 0.1 M SnCl₄ aqueous solution was spin-coated at 5000 rpm for 10 s on the substrates to get ~20 nm thickness. Then the substrates were transferred onto a hotplate and heated at 180 °C for 1 h and cooled down.

4.5.3. Perovskite characterization

X-ray diffraction (XRD) analysis in an angle range of $2\theta = 3^\circ$ to 30° was carried out using a Bruker D8 Advance diffractometer. The absorbance and reflectance measurements were performed with an integrating sphere using a UV/Vis/NIR spectrophotometer (PerkinElmer Lambda). Photoluminescence were measured using a Fluorolog-3 (Horiba Scientific) with an excitation laser of 450 nm. High-resolution scanning electron microscope (SEM) images were obtained on a ZEISS Merlin at an accelerating voltage of 5 kV. Atomic force microscopy (AFM) images were acquired using a Park NX10 (Park system) and analyzed with XEI AFM data analysis software.

Time-resolved PL experiments were performed with a spectrophotometer (Gilden Photonics) using a pulsed source at 480 nm (Ps diode lasers BDS-SM). The time-resolved signals were recorded by a Time Correlated Single Photon Counting detection technique with a time resolution of 1 ns.

For the STEM and STEM-EDX measurements, cross-sectional lamellae were prepared from the devices using the conventional focused ion beam (FIB) lift-out technique on a Zeiss Nvision 40. To reduce FIB induced damage, a final thinning in the FIB at 5 kV using a beam current of 80 pA was employed. To minimize exposure to air, the data were acquired just after the FIB preparation. STEM imaging and energy dispersive X-ray analysis were performed on an aberration-corrected FEI Titan Themis 60-300 transmission electron microscope in scanning mode at an accelerating voltage of 200 kV. This microscope is equipped with a high brightness X-FEG gun and Bruker Super-X EDX detectors (four windowless silicon drift detectors).

The impedance spectra measurements were carried out with an SP-200 BioLogic potentiostat with an AC perturbation of 10 mV from 75 mHz to 1 MHz, at room temperature with 5% humidity. The illumination was tuned with an Oriel DC Regulated illuminator in order to make $V_{oc} = 880$, which corresponds to the operation region of the samples ($V_{oc} = 1.1$ V at 1 sun). With fitting purposes, in addition to the elements included in the equivalent circuit shown in the inset, extra series resistive and inductive elements were also considered. In the equivalent circuit R_b and C_b are the resistive and capacitive elements, respectively, behind the high frequency arc in the Nyquist plot, whose physical meaning is related to dielectric and chemical bulk properties. On the other hand, R_s and C_s analogously characterize the high frequency arc whose nature may be associated with interface phenomena.

Ultra-violet photoelectron spectroscopy (UPS) was carried out in an ultrahigh vacuum. The photon line width was ~ 250 meV and the minimum spot size was ~ 1 mm. He I photons (21.2 eV) with a bias of 5 eV were used to acquire the spectra at a normal emission level. The photoelectrons were collected using a Sigma Probe (Thermo VG Scientific) with 50 meV precision.

4.5.4. Solar cell measurement

Photovoltaic performance was evaluated using commercial solar simulators (Oriel, 450 W, Xenon, AAA class). The light intensity was matched to one sun (AM 1.5G or 100 mW cm^{-2}) by calibrating with a Si reference cell equipped with an IR-cutoff filter (KG5, Newport), and it was done before each measurement. Current–voltage (J – V) curves of the PSCs were obtained by applying an external voltage bias while measuring the current response using a Keithley 2400 digital source meter. The voltage scan rate was 25 mV s^{-1} in forward and reverse scans. Devices were not preconditioned such as light soaking or a pre-voltage bias applied before starting the measurement. The cells were masked with an active area of 0.16 cm^2 . EQE was measured using an IQE200B (Oriel) without bias light.

Stability tests were carried out in a sealed cell holder with a glass cover (house made), where argon gas was filled to remove the residual water and oxygen from the holder. For the ambient condition test, the argon gas was turned off and the humidity and oxygen were not controlled, and the cells were encapsulated with surlyn (solaronix) and glass coverslips. In this case, the humidity was not controlled but the laboratory humidity was monitored, which ranged from 30 to 60% relative humidity at room temperature. In the glass cover, 0.1225 cm² masks were equipped. The LED lamp used in the system had a light intensity of 100 mW cm⁻². $J-V$ curves were recorded on an electronic system using a 22 bit delta-sigma analog to digital converter. A scan rate of 25 mV s⁻¹ with a step size of 5 mV was used and the devices were kept at the temperature of 50 °C. Every 2 hours the $J-V$ measurement and maximum power point tracking were performed. A reference Si-photodiode was placed in the same holder to check the intensity of the light.

Chapter 5. Lead-Free Perovskite (Hysteresis-Free Lead-Free Double Perovskite Solar Cells by Interface Engineering)

This chapter was published as the above title in *ACS energy letter*, 2018, 3, 1781-1786.

In authors (Martina Pantaler, Kyung Taek Cho, Valentin IE Queloz, Inés García Benito, Christian Fettkenhauer, Irina Anusca, Mohammad Khaja Nazeeruddin, Doru C Lupascu, Giulia Grancini), I am the first co-authors. I designed the experiment and helped and guided my co-author.

5.1. Abstract

Hybrid perovskite solar cells have been creating considerable excitement in the photovoltaic community. However, they still rely on toxic elements, which impose severe limits on their commercialization. Lead-free double hybrid perovskites in the form of $\text{Cs}_2\text{AgBiBr}_6$ have been shown to be a promising nontoxic and highly stable alternative. Nevertheless, device development is still in its infancy, and performance is affected by severe hysteresis. Here we realize for the first time hysteresis-free mesoporous double-perovskite solar cells with no *s*-shape in the device characteristic and increased device open-circuit voltage. This has been realized by fine-tuning the material deposition parameters, enabling the growth of a highly uniform and compact $\text{Cs}_2\text{AgBiBr}_6$, and by engineering the device interfaces by screening different molecular and polymeric hole-transporting materials. Our work represents a crucial step forward in lead-free double perovskites with significant potential for closing the gap for their market uptake.

5.2. Introduction

Since their advent, organic–inorganic hybrid perovskite solar cells (PSC) have raised a great deal of enthusiasm in the photovoltaic (PV) research community. With power conversion efficiency (PCE) surpassing 22% after only 9 years of research,^{9, 11} this technology has the potential to stand out over other PV solutions, such as dye-sensitized solar cells; organic polymer solar cells; and even commercial polycrystalline Si solar cells, leaders in the current market.^{9, 11} However, despite their excellent performance resulting in high efficiency, they suffer from poor device stability mainly due to perovskite material degradation upon moisture and light exposure.⁷⁶⁻⁷⁸ In addition, they rely on toxic lead, representing a serious drawback for PSC commercialization because of the health and environment concerns associated with its possible release out of the cell.^{79, 80} Huge theoretical effort in screening “less toxic” materials is ongoing. Tin (Sn) has first been used to replace the position of Pb^{2+} as $\text{MASn}_x\text{Pb}_{1-x}\text{I}_3$, with PCE now reaching 12%.⁸¹ However, such samples are prone to oxidation (Sn^{2+} into Sn^{4+}). On the other side, Sn has been incorporated in A_2SnX_6 structures (e.g., Cs_2SnI_6),^{82, 83} which exhibit better stability because of the presence of Sn in its stable oxidation state, leading to rapid efficiency decay in ambient conditions.⁸⁴ To solve this problem, “quasi-2D perovskites” in the form of $(\text{PEA})_2(\text{FA})_{n-1}\text{Sn}_n\text{I}_{3n+1}$ were also suggested as a possible solution to improve material stability.⁸⁵ They have been obtained by mixing the different organic cations in a sort of bulk heterojunction structure, where the PEA molecules infiltrate at the boundary of perovskite grains blocking the oxygen diffusion into the perovskite lattice.⁸⁵ This resulted in a PCE of up to 6% with

enhanced stability. Other quasi-2D perovskites in the form of $(\text{BA})_2(\text{MA})_{n-1}\text{Sn}_n\text{I}_{3n+1}$ have also been developed that show promising PCE of around 2.5% for $n = 4$ and are stable for more than 1 month.⁸⁶ However, despite the improvements, the presence of Sn does not eliminate all toxicity concerns.⁸⁰ Instead of considering other divalent cations to eliminate the toxic Pb^{2+} , recent works have demonstrated the substitution of the two divalent Pb^{2+} ions into one monovalent ion M^+ and another trivalent ion M^{3+} , while keeping the total number of valence electrons unchanged at the halogen sites. The structure reads as $\text{A}_2\text{M}^{1+}\text{M}^{3+}\text{X}_6$, where $\text{A}^+ = \text{Rb}^+, \text{Cs}^+, \text{CH}_3\text{NH}_3^+$; $\text{M}^+ = \text{Na}^+, \text{K}^+$; $\text{M}^{3+} = \text{Bi}^{3+}$; and $\text{X}^- = \text{Cl}^-, \text{Br}^-$, which were first reported in the 1970s.⁸⁷⁻⁹¹ Among these, experimental syntheses of $\text{Cs}_2\text{AgBiCl}_6$ and $\text{Cs}_2\text{AgBiBr}_6$ have been successfully demonstrated, using both solid-state reaction or solution processing methods.⁹²⁻⁹⁴ $\text{Cs}_2\text{AgBiCl}_6$ and $\text{Cs}_2\text{AgBiBr}_6$ appear as good potential candidates for solar absorbers in PSCs.^{92, 93} Despite the large band gap and indirect absorption, these materials exhibit extraordinarily long radiative emission lifetime of hundreds of nanoseconds, high defect tolerance, and higher stability of heat and moisture compared to conventional perovskites.⁹³ In addition, charge carrier effective masses of $0.14m_e$, close to those calculated for methylammonium lead iodide ($\text{CH}_3\text{NH}_3\text{PbI}_3$), have been derived.⁹⁴ All properties make this class of materials an interesting alternative for nontoxic PSCs. For $\text{Cs}_2\text{AgBiBr}_6$ single crystal and thin films, theoretical prediction and experimental work revealed band gaps of 1.83 eV⁹³ and 2.19 eV,⁹² respectively. However, their incorporation in PSC as active layer has so far been very limited, mainly because of the challenge in the preparation of high-quality and compact double-perovskite thin films. Although $\text{Cs}_2\text{AgBiBr}_6$ perovskite meso-structure solar cells with a PCE close to 2.4% have been shown by Greul et al.,⁹⁵ this value was extracted from a device characteristic severely affected by a huge hysteresis and *s*-shape, which casts some doubt on the real device performance. In addition, they adopted a fast crystallization process which impedes the formation of a smooth and homogeneous $\text{Cs}_2\text{AgBiBr}_6$ layer. Micrometer-sized grains and a thick agglomerated morphology are formed on the capping layer, which is far from the ideal morphology for a clean interface with the HTM in the sandwiched PSC. In our work, we adopted a different strategy for the optimization of a facile and highly reproducible deposition protocol to obtain a 200 nm thick homogeneous $\text{Cs}_2\text{AgBiBr}_6$ capping layer in the meso-structure solar cell architecture. Furthermore, we screened different HTMs beyond the most used spiro-OMeTAD to optimize the perovskite/HTM interface and device parameters. As a result, we fabricated lead-free PSCs with no hysteresis in the device characteristic, leading to a real PCE beyond 1% with high fill factor (FF) up to 0.7. This work establishes a defined and robust protocol and sets the basic guidelines for an optimized growth of $\text{Cs}_2\text{AgBiBr}_6$ perovskite active layers, resulting in a device behavior free from hysteresis artifacts. We

believe that our approach will enable surpassing the current limits in lead-free double-perovskite technology, opening the way for massive device optimization in the near future.

5.3. Results and discussion

Double-perovskite materials are known to crystallize in the elpasolite structure, a highly symmetric face-centered cubic double-perovskite structure which can be denoted as $A_2M^+M'^{3+}X_6$.⁹⁶ This structure consists of a network of corner-sharing octahedra, with Cs^+ (for A^+) in the middle of the cuboctahedral cavity while the centers of the octahedra are occupied by either Bi^{3+} or Ag^+ (for M and M' , respectively) with an alternating rock-salt configuration, as shown in Figure 48a. The $Cs_2AgBiBr_6$ film has been deposited by using spin coating deposition of a solution 0.5 M $Cs_2AgBiBr_6$ in dimethyl sulfoxide (DMSO) and annealing at high temperature. In more detail, we first monitored the film growth and crystal quality while varying the annealing temperatures in the range of 250–280 °C for 5 min. Figure 48b reports the X-ray diffraction (XRD) pattern of the double perovskite $Cs_2AgBiBr_6$ deposited on mesoporous TiO_2 (m- TiO_2)/FTO substrate. A main peak at 31.8° is present, representative of the (400) reflection of the double perovskite $Cs_2AgBiBr_6$, along with other main reflections (111, 200, 220, 311, 222, and 331). This pattern is evident for all the temperature range used, providing solid proof for the successful formation of a phase-pure double perovskite at a temperature greater than 250 °C (see Figure 49 for more details). Notably, no additional peaks related to possible residuals of $Cs_3Bi_2Br_9$ or $AgBr$ have been observed. In addition to the high temperature, we also introduced a few other control parameters to drive the material crystallization, aiming to obtain a homogeneous film with high crystal quality.⁹⁷ In particular, we adopted a second step in the deposition, known in the standard perovskite method as an antisolvent dropping technique. In this case, we dropped chlorobenzene during the film formation before the annealing step, aiming to obtain a compact and homogeneous layer without any pinholes. Overall, our optimization protocols enable the realization of a 200 nm thick $Cs_2AgBiBr_6$ film that shows a smooth and compact double-perovskite layer with an average grain size of around 80 nm, as shown from the top surface of the scanning electron microscopy (SEM) image in Figure 48d. This achievement represents a step forward in the optimization of the double-perovskite morphology, which has highly challenged the community in the last year. This is especially relevant when compared to the state-of-the-art samples showing a dishomogenous and disconnected island-like morphology.⁹⁵ As the $Cs_2AgBiBr_6$ films were optimized for photovoltaics, a sufficiently thick material is mandatory for efficient harvesting of light. To optimize the optical absorption, i.e. the

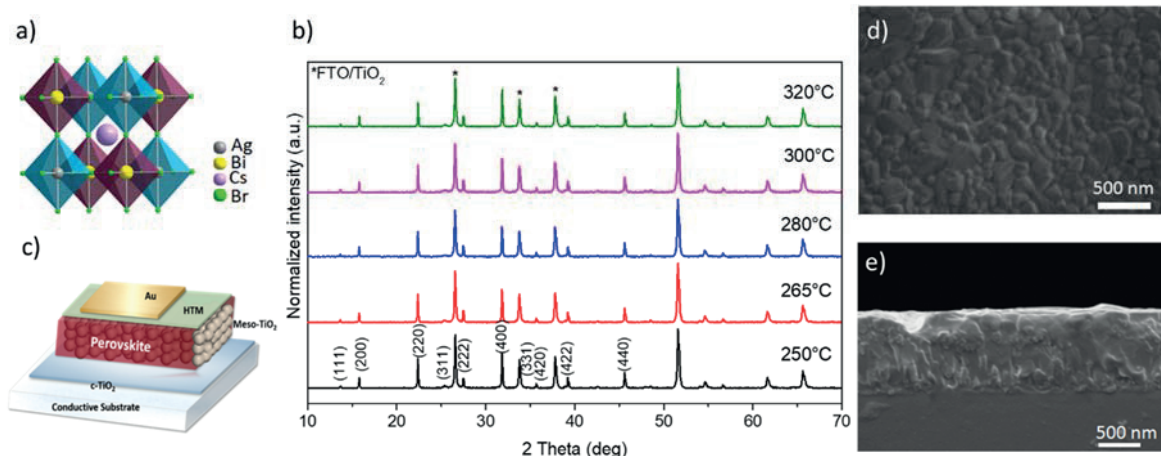


Figure 48. a) Cartoon of the Crystal structure of lead-free $\text{Cs}_2\text{AgBiBr}_6$ double perovskite. b) X-Ray diffraction (XRD) pattern of $\text{Cs}_2\text{AgBiBr}_6$ thin films deposited on mesoporous TiO_2 substrate at different annealing temperatures as indicated in the legend. c) Sketch of the device architecture used consisting of the double perovskite infiltrated in the mesoporous TiO_2 substrate and sandwiched, on top, with an organic HTM and gold top electrode. d) Scanning Electron Microscope (SEM) top view of the double perovskite layer obtained upon spin coating at room temperature using the anti-solvent treatment with chlorobenzene, e) SEM cross-section of the FTO/c- TiO_2 /m- TiO_2 /double perovskite sample, upon annealing at 280 °C. Scalebar shown in the figure.

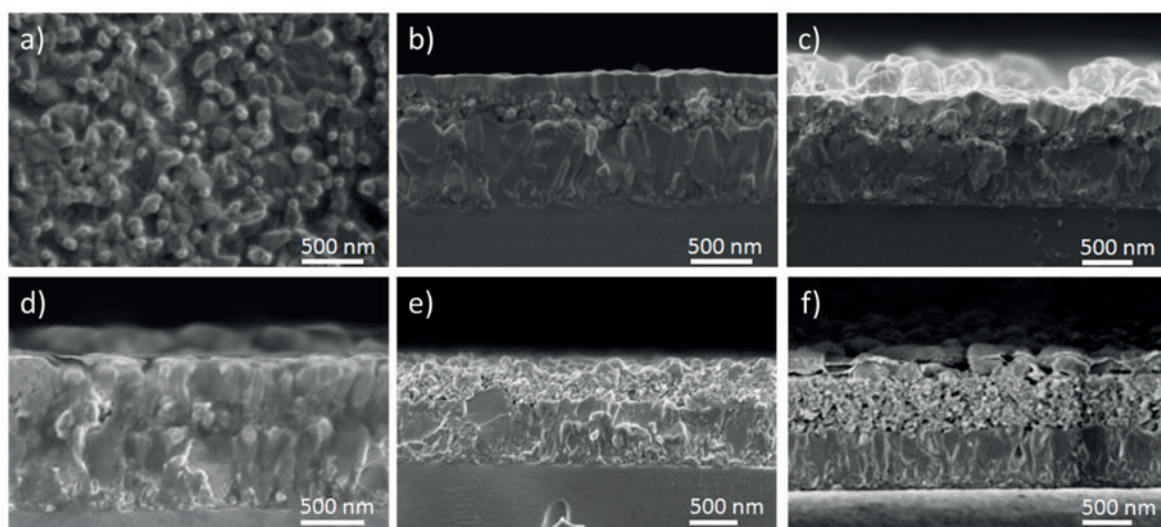


Figure 49. Double perovskite layer optimization and optimization of infiltration of double perovskite solution into mesoporous TiO_2 ; a) room temperature deposition and annealing at 220°C, b) cross-section of FTO/cTiO₂/mTiO₂/double perovskite, to low concentration of m-TiO₂ and no infiltration into m-TiO₂ layer, c) using double perovskite dissolved in DMF (0.16M) as 1st step deposition and double perovskite dissolved in DMSO (0.5M) as 2nd step deposition, d) ozone treatment on m-TiO₂ for 15min before spin coating of double perovskite, e) lower concentration of double perovskite dissolved in DMSO, f) TiCl_4 treatment.

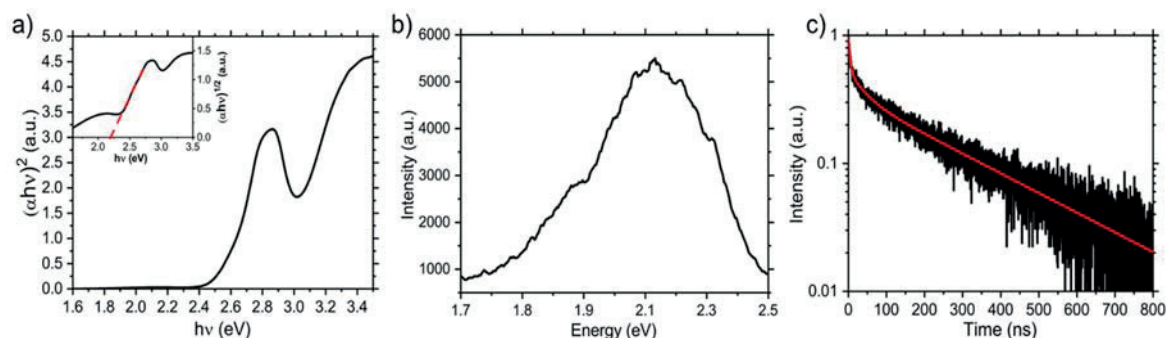


Figure 50. a) Absorption spectrum plotted in the form of Tauc plot, for an indirect bandgap, of the $\text{Cs}_2\text{AgBiBr}_6$ thin film deposited on glass (black). In inset, the Tauc plot for a direct bandgap with the dashed red line representing the linear fit for the band edge estimation. b) Photoluminescence (PL) spectra of the $\text{Cs}_2\text{AgBiBr}_6$ thin film. c) PL decay monitored at 2.1 eV. The decay is fitted using a bi-exponential function, resulting in fitted time constants of $\tau_1 = 5$ ns and $\tau_2 = 282$ ns (red).

thickness of the film, we aimed at improving the infiltration of the double-perovskite solution in the mesoporous oxide nanoparticle scaffold by modifying the m- TiO_2 surface. In more in detail, we pretreated the surface by ultraviolet (UV)-ozone for 15 min and by an additional TiCl_4 treatment. This led to a change in the surface properties of m- TiO_2 overall, further improving the material infiltration and crystallization, as shown by the SEM cross-sectional image in Figure 48d. Improving the material morphology is an essential step to reduce pinholes and paths for charge recombination. Overall, in our case, the optimal combination of the mentioned modifications and adjustments, such as UV-ozone and TiCl_4 treatment on TiO_2 ,⁹⁸ preheating solution at 75 °C before coating, antisolvent dripping technique on the spinning double-perovskite layer, along with the annealing at high temperatures, enabled the realization for the first time of a compact film of $\text{Cs}_2\text{AgBiBr}_6$. Notably, the choice of the solvent used also impacts the results obtained; indeed, the use of different concentration of DMF and DMSO can result in an inhomogeneous morphology (see Figure 49c and f). The inclusion of the preheating step turned to be also of fundamental relevance for thin-film optimization (Figure 49). Figure 50 reports on the optical characterization of the $\text{Cs}_2\text{AgBiBr}_6$ thin film in terms of optical absorption and emission properties. Absorption spectra are reported in Figure 50a. From the Tauc plot a step profile is observed, with a first onset at around 2.4 eV.⁹³ In the inset, the Tauc plot considering a direct band gap transition is also shown, giving a value for band gap of 2.20 eV, similar to what was already observed⁹⁸ for $\text{Cs}_2\text{AgBiBr}_6$ thin films.⁹³ The retrieved band gap value is consistent with that reported in the literature, within a variation range due to the different deposition approach used.⁹³ It is fair mentioning that, according to the Shockley–Queisser limit, a theoretical maximum PCE of 16.4% can be targeted with a material having a E_g of 2.2 eV, thus showing huge potential for working double-perovskite-based solar cells.⁹⁵ The $\text{Cs}_2\text{AgBiBr}_6$ emission

results are weak because of the indirect band gap nature of the material. The PL spectrum is reported in Figure 50b, peaking at 2.1 eV. The signal is very low in intensity, due to the indirect band gap nature of the material. To assess the fate of photogenerated carriers, we measured the time-resolved PL decay, shown in Figure 50c, monitored at the emission peak. The PL intensity shows a fast initial drop (fitted with $\tau_1 = 5$ ns), followed by a slower one ($\tau_2 = 282$ ns), which is similar to what is observed for double-perovskite thin films.⁹³ Notably, the fast decay is associated with trap and/or surface-state emission, which, given the weak PL signal, in this case dominates. On the other side, the longer-lifetime processes may originate from fundamental charge recombination, in agreement with the long carrier lifetime extracted in $\text{Cs}_2\text{AgBiBr}_6$ single crystals, which in this case is much longer than that of standard methylammonium lead iodide-based perovskites.⁹³

Using our optimized perovskite, we fabricated solar devices in which the perovskite is sandwiched between the 2,2',7,7'-tetrakis(*N,N*-dimethoxyphenylamine)-9,9'-spirobifluorene (spiro-OMeTAD) hole-transporting material and the mesoscopic TiO_2 scaffold (m- TiO_2) electron transporter in a standard mesoporous architecture. As known from the literature⁹⁵ and represented in Figure 51a, the energy level diagram shows that the conduction band (CB) of the $\text{Cs}_2\text{AgBiBr}_6$ is well-aligned with the CB of the electron-transporting mesoporous TiO_2 . Aiming to improve the device performance, we explored a series of different molecular and polymeric HTMs having slightly different highest occupied molecular orbital–lowest unoccupied molecular orbital (HOMO–LUMO) values, as shown in the energy diagram in Figure 51a. In addition to spiro-OMeTAD, typically used for lead perovskite solar cells, we considered PTAA (poly[bis(4-phenyl)(2,4,6-trimethylphenyl)amine]) and PCPDTBT

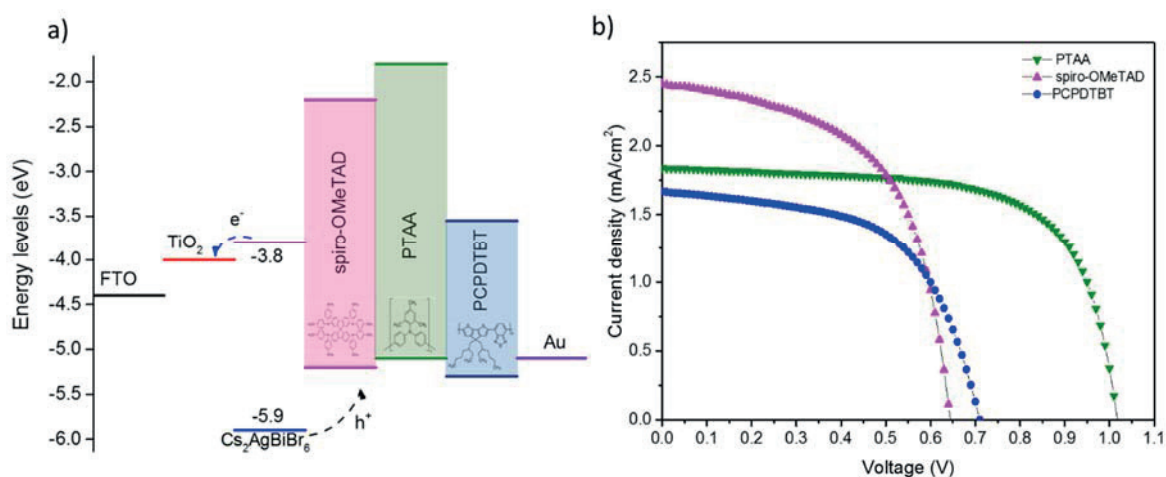


Figure 51. a) scheme of corresponding energy level diagram with the following energy values; FTO (-4.4eV), TiO_2 (-4.0eV), $\text{Cs}_2\text{AgBiBr}_6$ (HOMO; -5.9eV and LUMO; -3.8eV), spiro-OMeTAD (-5.2eV, -2.2eV), PTAA (-5.1eV, -1.8eV), PCPDTBT (-5.3eV, -3.55eV) and Au (-5.1 eV), b) J-V curves for best performance solar cells using different HTMs

(poly[2,1,3-benzothiadiazole-4,7-diyl[4,4-bis(2-ethylhexyl)-4H-cyclopenta[2,1-b:3,4-b']dithiophene-2,6-diyl]]), which are used in the PSC literature as polymeric HTMs.^{24,99}

The current–voltage (J – V) characteristics of the solar cells under simulated air mass 1.5 global standard sunlight (AM1.5G) are reported in Figure 51b, and the device parameters summarized in Table 3. The best solar cell performance resulted from using PTAA as HTM. Short-circuit current (J_{SC}) of 1.84 mA/cm² and open-circuit voltage (V_{OC}) of 1.02 V are obtained (Table 3). The spiro-OMeTAD-based solar cells show reasonable J_{SC} and V_{OC} of around 0.64 V. It is interesting to note the high V_{OC} value obtained despite the similarities in the HOMO level between spiro-OMeTAD, PCPDTBT, and PTAA, and the value of the latter is slightly higher for the latest.¹⁰⁰ It is fair to mention that although the interface energy level alignment represents a useful rule of thumb for screening the best HTM and evaluating the device V_{OC} , a direct link between HTM energy levels and device V_{OC} cannot be unambiguously derived. This is because device V_{OC} can be affected by multiple parameters which simultaneously come into play. Interfacial energy level mismatch, any possible internal electric field established by the difference in the work functions of the interfacial layers, interface charge accumulation, and bulk charge recombination can all affect. Importantly, those parameters that are highly sensitive to the perovskite crystal quality and film morphology.^{101, 102} We do not aim to address all the possible parameters and processes affecting the V_{OC} , which would extend beyond the scope of our work. However, we do note that the optimization process of the perovskite film itself—modifying the perovskite crystal quality, grain boundaries, and film homogeneity—strongly influences the V_{OC} (Figure 49 and 52). For instance, as shown in Figure 53, when we prepared a device using the perovskite film without the antisolvent dropping step but

Table 3. Photovoltaic parameters of devices based on the different HTMs; Short–circuit current density (J_{SC}), Open-Circuit Voltage (V_{OC}), Fill Factor (FF) and Power Conversion Efficiency (PCE). Notably, device statistics has been conducted on 44 devices (spiro-OMeTAD), 27 devices (PTAA), 6 devices (PCPDTBT)

HTM	J_{SC} (mA/cm ²)	V_{OC} (V)	FF	PCE (%)
PCPDTBT	1.67	0.71	0.57	0.68
spiro-OMeTAD	2.45	0.64	0.57	0.90
PTAA	1.84	1.02	0.67	1.26

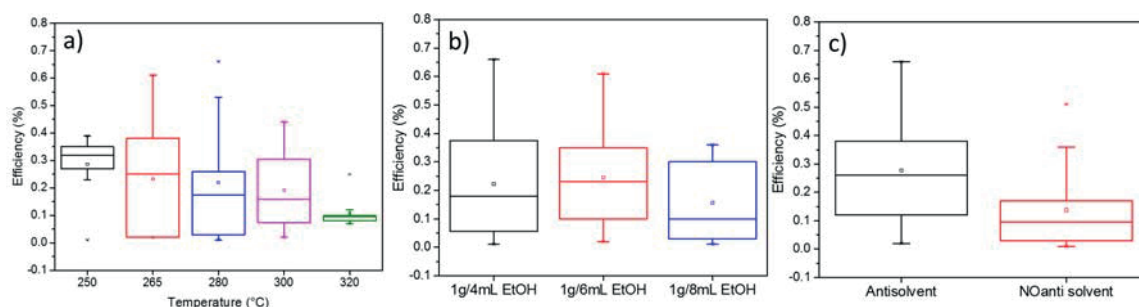


Figure 52. Device statistic on optimized layers, power conversion efficiency of solar cells; a) using different temperatures annealing (250-320°C) of $\text{Cs}_2\text{AgBiBr}_6$ double perovskite layer, b) using different concentration of m- TiO_2 dispersed in EtOH, c) using antisolvent (chlorobenzene) and non-antisolvent treatment.

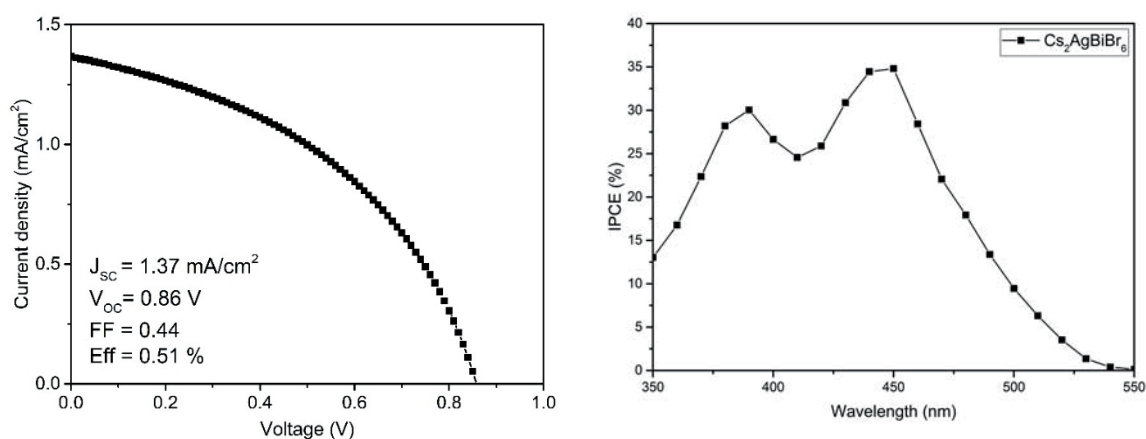


Figure 53. J-V curve for solar cells using antisolvent treatment and PTAA as HTM.

Figure 54. IPCE spectrum of $\text{Cs}_2\text{AgBiBr}_6$ perovskite solar cells with PTAA

keeping PTAA as HTM, we see a remarkable drop in the device V_{OC} , despite the same interfacial energy level alignment and device architecture.

The incident photon to current conversion efficiency (IPCE) spectrum (Figure 54) shows a band edge at ~ 525 nm, which is in agreement with the absorption edge in Figure 50a. On the other side, PCPDTBT-based solar cells show reduced voltage as well as reduced photocurrent. This can come from the lower band gap of PCPDTBT, and lower LUMO level, which can decrease the charge-transfer selectivity. Overall, this suggests that not only the interface energetics but also the interface quality and photoinduced processes, such as charge recombination, are of the utmost importance for optimizing the device performance. Device results are confirmed based on statistics of around 70 devices, as shown in Figure 55. An important characteristic that must be evaluated when measuring

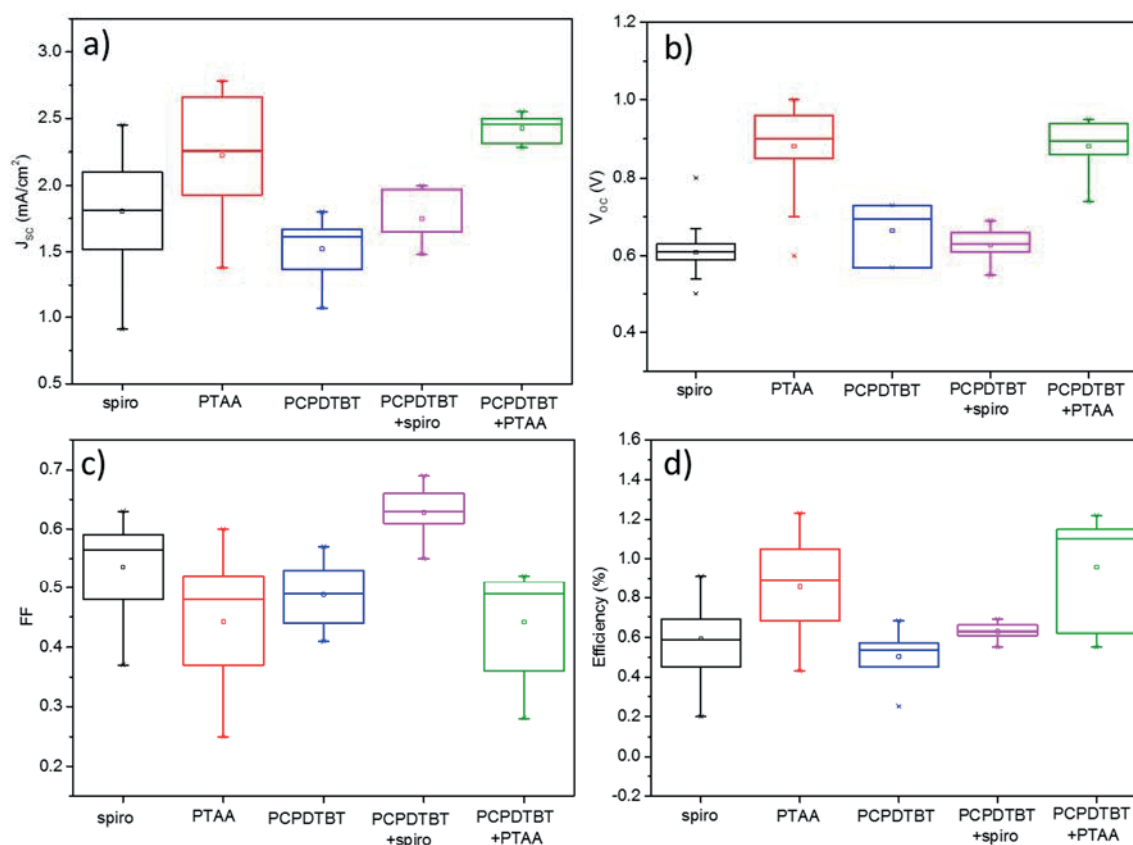


Figure 55. Statistical distribution of photovoltaic parameter for perovskite solar cells performance with different HTMs; a) short circuit current J_{sc} , b) open-circuit voltage V_{oc} , c) fill factor FF, d) power conversion efficiency

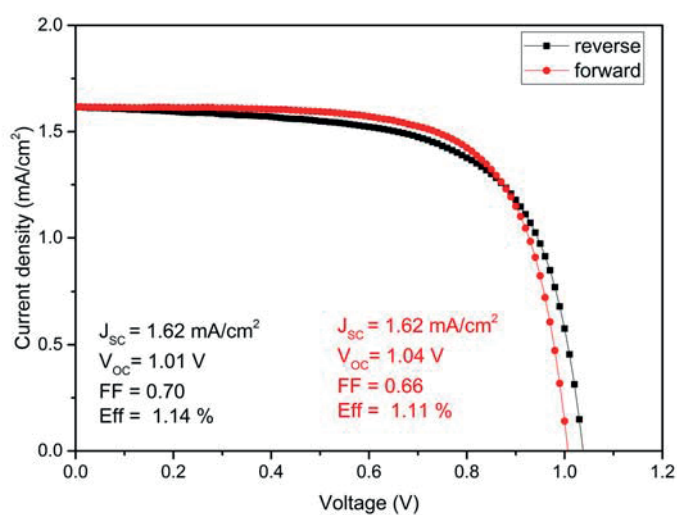


Figure 56. Current – Voltage ($J-V$) curves of forward and reverse scan showing no hysteresis. Device parameters are reported in the inset.

perovskite solar cells is the shape of the J - V curve measured at different scanning voltage directions. Indeed, for lead-based perovskite, as well as for previously reported $\text{Cs}_2\text{AgBiBr}_6$ -based solar cells,⁹⁵ a significant difference has been observed, which is indicative of a hysteresis behavior. Although the exact reasons behind this behavior are a subject of ongoing debate, it is the general consensus that effects such as light-induced ion movement, “photo-instability”, or structural deformations can overall contribute to the anomalous hysteresis behavior.¹⁰³⁻¹⁰⁵ Even for $\text{Cs}_2\text{AgBiBr}_6$, this has been previously assigned to ion and defect movement in the device, despite the totally different material structure and composition.⁹⁵ Figure 56 shows the J - V hysteresis for our devices using PTAA as HTM. Notably, our device shows a hysteresis-free behavior, reporting nearly identical values for the device parameters extracted in the back and forward configurations. This contrasts to what has been shown by Greul et al., who reported a tremendous hysteresis due to migration of the halide anions and trapping–detrapping of charge carriers.⁹⁵ We observe a different behavior: in our case, as shown in Figure 56, no difference in carrier collection during the forward and reverse scan is observed, leading, for the first time, to the observation of a hysteresis-free device behavior in lead-free double-perovskite solar cells. We ascribe this to the ideal and compact film structure and morphology we obtained, which can reduce the material structural stability. Further work is ongoing to clarify this point to gain deeper insights on the ion movement and interface charge accumulation dynamics.

5.4. Conclusion

In conclusion, we report for the first time the investigation on the interface of lead-free double perovskite $\text{Cs}_2\text{AgBiBr}_6$ using a new deposition approach following a multistep optimization protocol. This enabled the realization of a compact thin film of $\text{Cs}_2\text{AgBiBr}_6$ double perovskite with optimal infiltration into the m- TiO_2 oxide scaffold. When embodied in solar cells, different contact polymers as HTM have been considered. PTAA has been here adopted reaching maximal power conversion efficiency up to 1.26% and showing for the first time no device hysteresis. We believe that our method describes a robust and easy optimization approach of double-perovskite thin films, which are paramount for hysteresis-free lead-free solar cells. This will pave the way for further material and device investigations, providing clear direction for the massive exploration of lead-free perovskite solar cells, which are a viable alternative for nontoxic perovskite commercialization in the near future.

5.5. Experimental section.

5.5.1. Synthesis double perovskite precursor

CsBr (99.9 %), BiBr₃ (99.0 %), AgBr (99.5 %), and HBr were purchased from Alfa Aesar. Cs₂AgBiBr₆ was synthesized as reported elsewhere.¹ For this purpose metal bromides were dissolved in 2:1:1 stoichiometric ratio in hydrobromic acid at 150°C for 2h, and cooled down to room temperature. The obtained orange powder was washed with ethanol and dried overnight (yield 59.7%).

5.5.2. Device preparation

After etching FTO glasses (Nippon sheet glass) by Zn powder and 2M HCl, they were sequentially cleaned with the detergent solution, acetone, and ethanol. And then by spray pyrolysis deposition for a compact TiO₂ layer, a precursor solution diluting titanium diisopropoxide (Sigma-Aldrich) in ethanol (0.6 ml: 10 ml) was coated on the cleaned FTO substrate heated at 450°C. After cooling, mesoporous TiO₂ film was prepared coating a diluted TiO₂ paste (Dyesol 30 NR-D) solution in ethanol and the substrates were sintered on a hot plate at 500°C for 30 min. Then, cooled substrates were dipped in 40mM TiCl₄ aqueous solution and kept at 70 °C for 10 min and sintered again at 500 °C for 30min. Finally, before spin coating perovskite solution, the substrates were treated under UV-ozone for 15 min. The double perovskite powder was dissolved in DMSO (0.5 mol/L) at 70 °C, spin coated at 4000 rpm for 30 seconds, and annealed at 280 °C for 5 min. PCPDTBT was purchased from Sigma Aldrich. It has been prepared dissolving in chlorobenzene (30 mg/mL), heated at 70°C and stirred overnight. The PCPDTBT solution was spin coated on the double perovskite (or on the PTAA/spiro-OMeTAD) at 1000 rpm for 45 seconds.² PTAA has been deposited on top of the double perovskite film at 3000 rpm for 30 seconds. The PTAA solution was prepared by 3 dissolving 15mg of PTAA in 1,5 mL toluene adding 15µL of 170mg of Li-TFSI in 1 mL acetonitrile and 7,5µL TBP.³

5.5.3. Characterization methods

X-ray diffraction (XRD) analysis in an angle range of $2\theta = 10^\circ$ to 70° was carried out using a Bruker D8 Advance diffractometer. Devices and film morphology were investigated using a scanning electron microscope (Teneo, Thermo Fischer Scientific). SEM images were acquired at an accelerating voltage of 2 kV and 100 pA electron beam current.

5.5.4. Device characterization

J-V curves were obtained using commercial solar simulators (Oriel, 450 W, Xenon, AAA class) for alight source. The light intensity was matched one sun (AM 1.5G or 100 mW cm⁻²) by calibrating with a Si reference cell equipped with an IR-cutoff filter (KG5, Newport), and it was done before each measurement. The voltage scan rate was 25 mV s⁻¹ as forward and reverse scan. Devices were not preconditioned such as light soaking or pre-voltage bias applied before starting the measurement. The cells were masked with an active area of 0.16 cm². EQE was measured using IQE200B (Oriel) without bias light.

5.5.5. Absorption and photoluminescence measurements

Steady-state absorption spectra were acquired with a Perkins Elmer lambda 950s UV/Vis spectrophotometer using an integrating sphere to account for optical losses outside of the active layer. Steady state and time resolved photoluminescence measurement where carried out on Horiba a Fluorolog-3, with a PMT as detector. The excitation source for the TCSPC is a Horiba nanoLED-370 with an excitation wavelength of 369nm and a pulse duration of 1.3ns.

Chapter 6. HTMs Investigation I (Perovskite solar cells employing molecularly engineered Zn (II) phthalocyanines as hole-transporting materials)

This chapter was published as the above title in *Nano energy*, 2016, 30, 853-857

The permission rule of *Nano energy*:

Please note that, as the author of this Elsevier article, you retain the right to include it in a thesis or dissertation, provided it is not published commercially. Permission is not required, but please ensure that you reference the journal as the original source. For more information on this and on your other retained rights, please visit: <https://www.elsevier.com/about/our-business/policies/copyright#Author-rights>

In authors (Kyung Taek Cho, Kasparas Rakstys, Marco Cavazzini, Simonetta Orlandi, Gianluca Pozzi, Mohammad Khaja Nazeeruddin), I was fabricating solar cells by HTMs synthesized by my co-authors. I summarized the data and the results.

6.1. Abstract

Amino donor groups-substituted zinc(II) phthalocyanines (ZnPcs) **BI25**, **BL07** and **BL08** were obtained via cyclotetramerization of suitable phthalonitriles that were synthesized by Pd catalyzed amination reaction between 4-iodophthalonitrile and a selected secondary amine. The **BI25**, **BL07** and **BL08** ZnPcs were characterized using spectroscopic and electrochemical methods, and used as hole transporting layer in PSCs. The open circuit voltage (V_{OC}) of perovskite solar cell devices reached close to 1 V, and the short-circuit current density (J_{SC}) values evaluated from J-V curves were 16.2, 8.42, and 16.9 mA/cm², respectively, demonstrating influence of the HOMO levels of ZnPcs. A power conversion efficiency of 11.75% was obtained in the case of **BI25**, which is the highest value ever reported using ZnPcs as HTMs in perovskite solar cells with traditional device geometry.

6.2. Introduction

Recently, organic-inorganic hybrid perovskites have been advocated as alternative promising photovoltaic materials for light harvesting,¹⁰⁶ especially methylammonium lead halide ($CH_3NH_3PbX_3$ or $MAPbX_3$, X = Cl, Br, and I) perovskite. Since the first report of perovskite solar cells (PSCs) introduced by Miyasaka,¹⁰⁷ the power conversion efficiency (PCE) of PSCs has increased remarkably from 3.8% to 20.8% in a short span of less than 5 years.^{31, 43} In PSCs, hole transporting materials (HTMs) are one of the key components. Although the devices can work without HTMs,¹⁰⁸ HTMs are required to obtain high performance solar cells, since HTMs facilitate charge carrier separation and extraction by transporting hole from perovskite materials to cathode and reducing unwanted charge recombination reaction.¹⁰⁹ 2,2',7,7'-Tetrakis(*N,N*-di-*p*-methoxyphenylamine)-9,9'-spirobifluorene (spiro-OMeTAD) is the most commonly used HTM in PSC,^{43, 110, 111} as it has been previously studied in solid state dye-sensitized solar cells (DSSCs).¹¹² Nevertheless, the cost of spiro-OMeTAD is unfortunately high due to low synthesis yield and complicated purification. In addition, some additives for using spiro-OMeTAD as HTM in complete devices accelerate the decomposition of perovskite materials and it has detrimental effects on the long-term stability of the whole device. Consequently, tremendous efforts are currently devoted to development of new classes of stable, easily accessible HTMs holding promises to replace spiro-OMeTAD.

Phthalocyanines (Pcs) are photo- and electrochemically stable compounds structurally related to porphyrins, with remarkable light-harvesting capability in the far-red and near-IR spectral regions

where the maximum solar photon flux occurs. Light absorption, solubility and other relevant photovoltaic properties of Pcs can be tuned easily by introducing suitable substituents in the peripheral or non-peripheral positions of the macrocycle and replacing the host metal ions. For these reasons, complexes of Pcs have attracted much attention as photosensitizers in DSSCs.¹¹³ More recently, researchers have started to explore the use of Cu(II) complexes of Pcs as HTMs in PSCs.^{109, 114-116} PCE values up to 15.4% have been reached in the case of complexes deposited as a film by thermal evaporation under vacuum¹¹⁵ and more convenient deposition techniques such as solution spin-coating proved to be successful (PCE up to 15.2% in the case of the Cu(II) complex of tetra-*tert*-butyl Pc) when applied to devices based on a mixed perovskite, (FAPbI₃)_{0.85}(MAPbBr₃)_{0.15}.¹⁰⁹ At the same time, a solution processable Zn(II)-phthalocyanine (ZnPc) bearing eight bulky 2,6-diphenylphenoxy substituents has been investigated as HTM, affording PCE up to 6.7%.¹¹⁶ Hence, molecularly engineered ZnPc derivatives are good candidates for fabricating flexible, large-area, low-cost PSCs with good long-term stability.

According to computational studies, the introduction of secondary amine substituents at the periphery of Pc ring should have a deep impact on the light absorption properties and energy levels of ZnPcs.^{117, 118} In particular, diphenylamino-substituted ZnPcs should exhibit higher HOMO-LUMO levels and reduced bandgaps with respect to their phenoxy-substituted analogues. We thus inferred that ZnPcs bearing electron rich bis-aryl substituents, might be interesting as HTMs for PSCs. In order to avoid any unnecessary synthetic complexity, the molecular design of the prototype 2,6-diphenylphenoxy substituted ZnPc could be also simplified by reducing the number of macrocycle substituents from eight to four. Following this line of reasoning, three novel ZnPcs (**Figure 57**) have been readily obtained and successfully used as HTMs for solution processed PSCs.

6.3. Results and discussion

6.3.1. Synthesis and characterization of ZnPcs

The amino substituted phthalonitriles **1**, **2** and **3**, starting materials for the synthesis of ZnPcs **BI25**, **BL07** and **BL08**, respectively, were prepared by Pd catalyzed amination reaction between 4-iodophthalonitrile and a selected secondary amine (**Figure 58**).

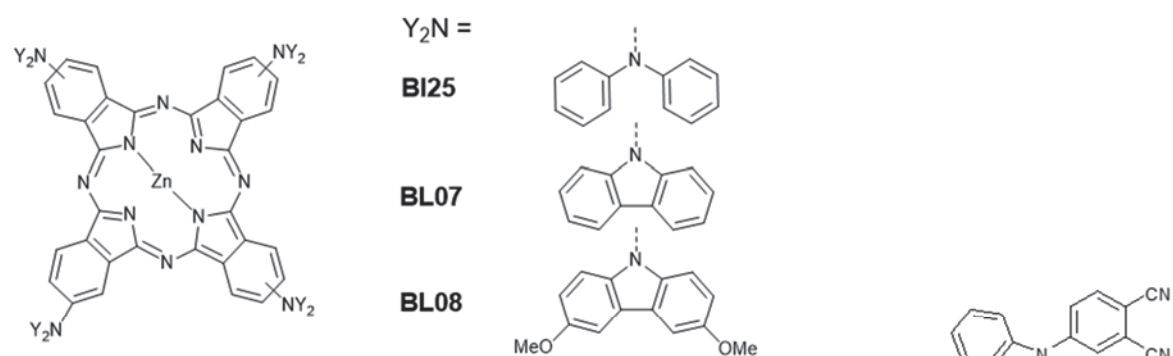


Figure 57. Molecular structures of synthesized ZnPcs.

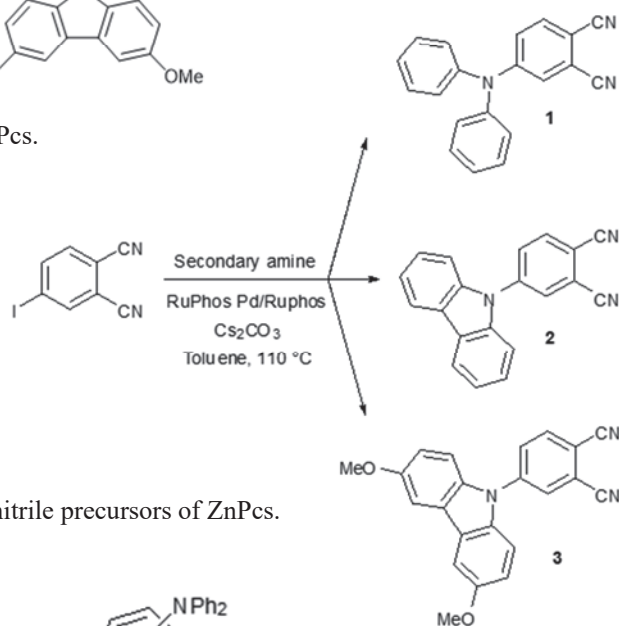


Figure 58. Synthesis of phthalonitrile precursors of ZnPcs.

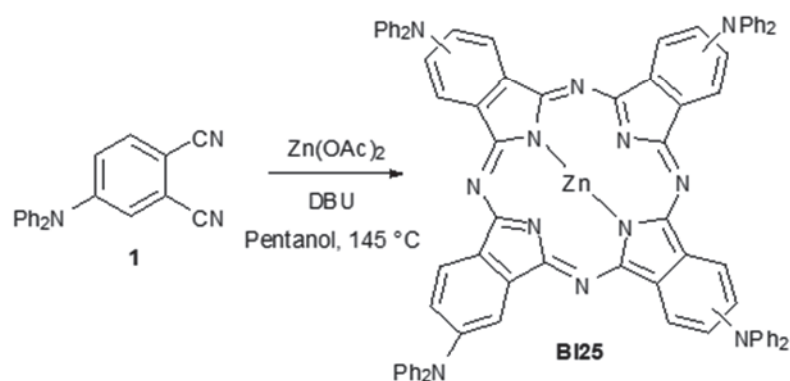


Figure 59. Example of cyclotetramerization reaction.

The synthesis of phthalonitrile **1** by displacement reaction of the nitro group of 4-nitrophthalonitrile with diphenylamine had been previously reported.¹¹⁹ Unfortunately, this procedure proved to be unsuitable in the case of **2** and **3** and, in our hands, afforded **1** in very low yields, too. In contrast, the C-N cross coupling reaction promoted by the couple RuPhos/RuPhos Pd, a specific combination for the arylation of secondary amines,¹²⁰ afforded all the desired phthalonitriles in excellent yields (82-98%). ZnPcs **BI25**, **BL07** and **BL08** were subsequently obtained as mixtures of positional isomers by cyclotetramerization reaction of the corresponding phthalonitriles in the presence of 1,8-diaza-

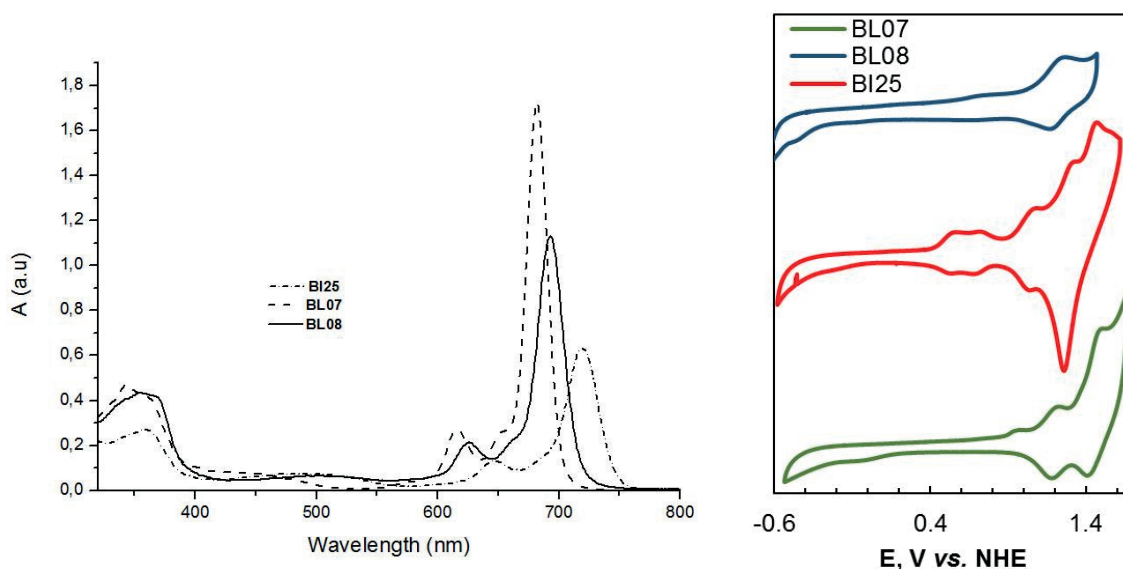


Figure 60. UV–vis spectra of BI25 ($3.11 \times 10^{-6} \text{M}$), BL07 ($6.05 \times 10^{-6} \text{M}$) and BL08 ($4.73 \times 10^{-6} \text{M}$) in THF solution.

Figure 61. Cyclic voltammograms of ZnPcs-based HTMs. Measured in DCM/tetra-*n*-butylammonium hexafluorophosphate (0.1 M) solution, using glassy carbon working electrode, Pt reference electrode, and Pt counter electrode with Fc/Fc⁺ as an internal standard. Potentials were converted to the normal hydrogen electrode by addition of +0.624 V and -4.44 eV to the vacuum, respectively.

bicyclo[5.4.0]undec-7-ene (DBU) and Zn(OAc)₂ (**Figure 59**).

The presence of secondary amine substituents influences the UV–vis spectra of the new compounds (**Figure 60**), which exhibit intense Q bands and less intense broad absorption bands in the 400–550 nm region, probably due to $n\text{-}\pi^*$ transitions, in agreement with computational predictions.¹¹⁷ The considerable red shift of the Q band of **BI25** is particularly evident. In THF solution the absorption maximum of the diphenylamine substituted ZnPc is centered at 720 nm, whereas the carbazole substituted **BL07** absorbs at 682 nm. In turn, the introduction of electron donating methoxy groups in the 3,6-positions of the carbazole unit produces a noteworthy bathochromic effect, triggering the shift of the absorption maximum of **BL08** to 693 nm.

To compare the energy levels of new HTMs we performed cyclic voltammetry (CV) measurements. The experimental HOMO energy levels of all the HTMs were derived from the ground-state oxidation potential $E^{S+/S}$ estimated from cyclic voltammograms shown in **Figure 61**. As expected, carbazole substituted ZnPc **BL07** has significantly more stabilized HOMO level of -5.39 eV vs. vacuum comparing with that of stronger diphenylamine donor substituted **BI25** (-4.96 eV). Contrary, comparing **BL07** with **BL08**, the presence of methoxy groups in carbazole donors of **BL08** (-5.18

eV) shifted HOMO level up by approximately 200 mV. From the CV data we predict that all ZnPcs should have enough overpotential for favorable hole extraction from the $\text{CH}_3\text{NH}_3\text{PbI}_3$ perovskite (-5.48 eV).

6.3.2. Performance in PSCs

To test whether the synthesized ZnPCs can act as HTMs, we fabricated cells using perovskite as the light absorber, TiO_2 was coated as the electron transport layer and the MAPbI_3 perovskite layer was deposited by the anti-solvent dropping method.¹²¹ The cross-sectional scanning electron microscopy (SEM) image of the device using **BL08** as HTM is displayed in **Figure 62a**. Each layer in structure of the PSC is clearly defined. 400 nm thick perovskite layer is formed as a bi-layer structure, such as a combined layer with mp- TiO_2 (250 nm) and a uniform capping layer (150 nm) atop the mp- TiO_2 layer. HTM and Au layers are deposited sequentially on the top of the perovskite with the thickness of 150 nm and 80 nm, respectively. The suitable band alignment of three HTMs and the perovskite is shown in **Figure 62b**.

Figure 63a shows the current density-voltage (J-V) curves of devices with **BI25**, **BL07**, and **BL08** HTMs and the corresponding values are summarized in Table 1. The open circuit voltage (V_{OC}) of these devices reached the value close to 1V, which means that the HOMO of ZnPcs can match quite well with valence band of perovskite material. On the other hand, the current density (J_{SC}) and fill factor (FF) are quite low compared with reference cells using spiro-OMeTAD or PTAA most likely due to the lower lying LUMO of ZnPcs that leads to poor electron blocking and greater charge recombination. As shown by UV-vis spectra, **BI25**, **BL07**, and **BL08** strongly absorb light at around 700 nm. We note that ZnPcs used in this study have a small band gap and much lower LUMO energy

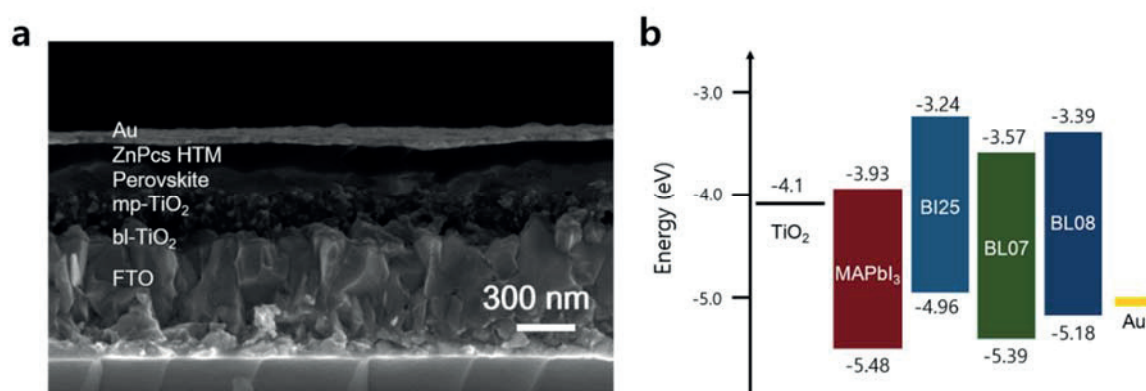


Figure 62. a) Cross-sectional SEM image of perovskite solar cell using BL08 as HTM. b) Energy level diagram of PSCs (FTO/blocking layer (bl)- TiO_2 /mesoporous (mp)- TiO_2 /MAPbI₃/HTM/Au) with different HTMs (right), where each HTM was employed for each complete devices.

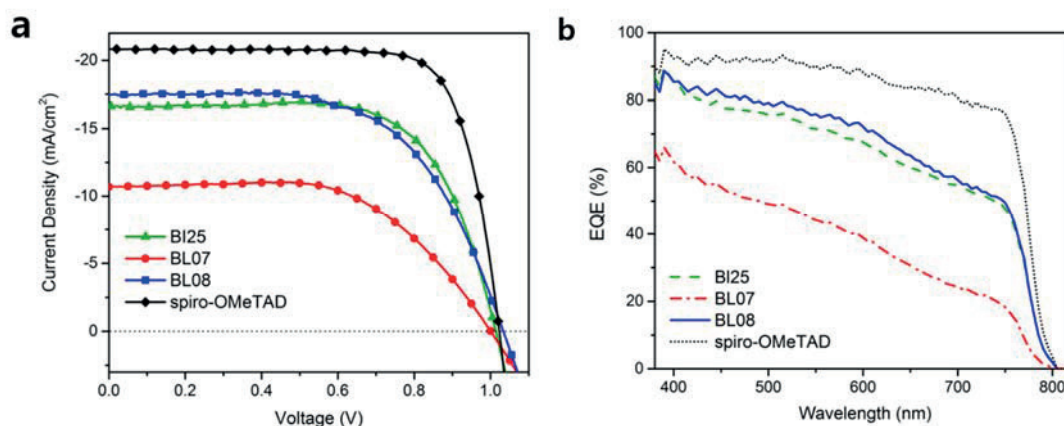


Figure 63. J-V curves of perovskite solar cells using BI25, BL07 and BL08 as HTMs (a). The curves were recorded scanning at 5mV/s from backward scan. EQE spectrum of the devices (b).

	V _{oc} [V]	J _{sc} [mA/cm ²]	FF [%]	PCE [%]	P _{in} [mW/cm ²]
BI25	1.014	-16.666	0.681	11.75	97.9
BL07	1.001	-10.693	0.598	6.65	96.3
BL08	1.034	-17.430	0.610	11.44	96.1
Spiro-OMeTAD	1.023	-20.806	0.767	16.78	98.0

Table 4. Summary of photovoltaic characteristics extracted from J-V curves of perovskite solar cells employing **BI25**, **BL07** and **BL08** as HTMs.

level than reference HTMs.

The external quantum efficiency (EQE) spectra for PSCs using three different HTMs is shown in **Figure 63b**. The integrated current densities are quite matched with the J_{sc} value evaluated from J-V curves as 16.2, 8.42, and 16.9 mA/cm², respectively. For devices with **BI25** and **BL08**, the EQE spectra are similar in the whole wavelength range. However, in case of **BL07**, the EQE is dropped comparing with latter. The short-circuit current density (J_{sc}) and EQE values of **BL07** is lower compared with **BI25** and **BL08**, due to the lack of over potential for blocking excited electrons backflows and favorable hole extraction from lower LUMO and HOMO energy levels of **BL07**, which is likely to cause more charge recombination.

6.4. Conclusions

In summary, we synthesized three Zn phthalocyanines (**BI25**, **BL07**, and **BL08**), which were applied as HTMs in perovskite (MAPbI₃) solar cells. Based on the UV-vis spectra and cyclic voltammetry (CV) measurement, each HTM demonstrates that the exciton dissociation and charge transfer are feasible at the interface between perovskite and HTM. The power conversion efficiency values of 11.75, 6.65, and 11.44% were obtained, respectively, which is the highest ever reported perovskite-based solar cells using ZnPcs as HTMs. We believe that this result will open new path for the molecular engineering of phtalocyanine-based HTMs to fabricate efficient and stable perovskite photovoltaic devices.

6.5. Experimental method and Charaterization.

6.5.1. Preparation of Zn(II)-phthalocyanines

In a flame dried Schlenk tube equipped with a stir bar phthalonitrile (1, 2 or 3, 1 mmol) and Zn(OAc)₂·2H₂O (55 mg, 0.25 mmol) were suspended in 1-pentanol (2 ml). The mixture was stirred for 15 min under a nitrogen atmosphere then DBU (150 μL, 1 mmol) was added and the mixture was heated at 145 °C for further 24 h. After cooling to room temperature the reaction mixture was poured into MeOH and the solid was collected by filtration on a Büchner funnel. The solid was thoroughly washed with MeOH, dried under reduced pressure. Column chromatography (silica gel, THF) followed by repeated washing with cold pentane gave the desired ZnPc as a mixture of positional isomers.

6.5.2. Device fabrication

FTO glass (NSG) was sequentially cleaned using detergent, acetone, and ethanol by ultrasonic bath for each 20 min. And then 40 nm TiO₂ blocking layer was deposited on the heated FTO at 450 °C by spray pyrolysis, using a precursor solution of 0.6 ml of titaniumdiisopropoxide and 0.4 ml of bis(acetylacetonate) in 9 ml of anhydrous isopropanol. About 250 nm mesoporous TiO₂ was spin-coated on the surface of bl-TiO₂/FTO substrate at a speed of 2000 rpm for 20 s from diluted 30NRT (Dyesol) with ethanol (1 g/7 ml). The substrate was then sintered at 500 °C for 20 min in air. The MAPbI₃ was spin-coated onto the TiO₂ mesoporous layer. The precursor solution was prepared as 1.2 M. The spin-coating was going through a two-step; first step is at 1000 for 10 s and then at

5000 rpm for 30 s. In the second step, 100 ml of chlorobenzene was dropped on the spinning substrate at 20 s. The substrates were then annealed at 100 °C for 30 min. The HTM solutions were prepared in chlorobenzene. The concentration of BI25, BL07, and BL08 solutions are 50, 30, and 30 mM, respectively and three additives, bis(trifluoromethylsulfonyl)-imide lithium salt (Li-TFSL, Sigma Aldrich), 4-*tert*-butylpyridine (TBP, Sigma Aldrich), and tris(2-(1*H*-pyrazol-1-yl)-4-*tert*-butylpyridine)-cobalt(III)tris(bis(trifluoromethylsulfonyl)imide) (FK209, Dyenamo), were added at a molar ratio of 0.4, 2.2, and 0.04, respectively. These HTM solutions were spun at 4000 rpm for 30 s. Finally, 80 nm of gold layer was deposited by thermal evaporation.

6.5.3. Characterization

A HR-SEM (ZEISS Merlin) was used to characterize the structure of the device cross-section. Solar cell efficiencies were measured using a potentiostat (Keithley model 2400) under simulated one sun irradiation from a Xe arc lamp with an AM 1.5 global filter. The light intensity was measured by an NREL certified KG5 filtered Si reference diode and was used for calibration. The active area exposed are defined to 0.16 cm². For IPCE characterization, a 100 W Xe lamp linked to a monochromator (Newport, IQE-200B) to tune the light beam accordingly.

Chapter 7. HTMs Investigation II (Molecularly Engineered Phthalocyanines as Hole-Transporting Materials in Perovskite Solar Cells Reaching Power Conversion Efficiency of 17.5%)

This chapter was published as the above title in *Advanced Energy Materials*, 2017, 7, 1601733.

In authors (Kyung Teak Cho, Olga Trukhina, Cristina Roldán-Carmona, Mine Ince, Paul Gratia, Giulia Grancini, Peng Gao, Tomasz Marszalek, Wojciech Pisula, Paidi Y Reddy, Tomás Torres, Mohammad Khaja Nazeeruddin), I obtained the best performance and helped some experiment.

7.1. Abstract

Easily accessible tetra-5-hexylthiophene-, tetra-5-hexyl-2,2'-bisthiophene-substituted zinc phthalocyanines (ZnPcs) and tetra-*tert*-butyl ZnPc are employed as hole-transporting materials in mixed-ion perovskite $[\text{HC}(\text{NH}_2)_2]_{0.85}(\text{CH}_3\text{NH}_3)_{0.15}\text{Pb}(\text{I}_{0.85}\text{Br}_{0.15})_3$ solar cells, reaching the highest power conversion efficiency (PCE) so far for phthalocyanines. Results confirm that the photovoltaic performance is strongly influenced by both, the individual optoelectronic properties of ZnPcs and the aggregation of these tetrapyrrolic semiconductors in the solid thin film. The optimized devices exhibit PCE of 15.5% when using tetra-5-hexyl-2,2'-bisthiophene substituted ZnPcs, 13.3% for tetra-*tert*-butyl ZnPc, and a record 17.5% for tetra-5-hexylthiophene-based analogue under standard global 100 mW cm^{-2} AM 1.5G illumination. These results boost up the potential of solution-processed ZnPc derivatives as stable and economic hole-transport materials for large-scale applications, opening new frontiers toward a realistic, efficient, and inexpensive energy production.

7.2. Introduction

Perovskite solar cells (PSCs) have reached record power conversion efficiencies (PCEs) in a remarkably short lapse of time,^{107, 122} rapidly becoming one of the top emerging technologies.⁹ Their fairly high PCEs are attributed to the unique optoelectronic properties of the perovskites, featuring intense panchromatic absorption¹²³ and high charge carrier mobilities.¹⁰ In addition, their band gap can be easily tuned by simple variation of their ionic composition.¹²⁴ For example, a mixed-ion perovskite obtained as a mixture of formamidinium (FA) lead iodide and methylammonium (MA) lead bromide, $[\text{FAPbI}_3]_{0.85}[\text{MAPbBr}_3]_{0.15}$, delivered the best to date energy conversion efficiencies of over 21% and revealed promising stability and reproducibility.^{43, 125, 126} All the above mentioned, together with the ambipolar charge transport characteristics of perovskites,¹²⁷ are exceptional properties behind the high efficiency reported in literature. However, highly efficient PSCs are mostly achieved when sandwiching the perovskite film between an electron-transport layer (ETM, n-type) and a hole-transport layer (HTM, p-type), to enhance the selective blocking and extraction of charges into the external circuit. In this connection, using mesoporous or planar metal oxide ETM, such as TiO_2 , delivered the best results.¹²⁸ In terms of HTM, small molecules and polymers have shown impressive performances, being so far 2,2',7,7'-tetrakis(*N,N*-di-*p*-methoxyphenylamine)-9,9'-spirobifluorene (Spiro-OMeTAD)¹⁰⁶ and poly(triaryl-amine) (PTAA)¹²⁹ the mostly used materials. However, despite their excellent performance with PCEs exceeding 20%, Spiro-OMeTAD and PTAA possess an elevated production cost and insufficient long-term stabilities, thus representing a

major bottleneck for a large-scale application. In this regard, phthalocyanines (Pcs) are attractive materials for the field of photovoltaics due to their high thermal-, chemical-, and photostability, known for their intense absorption in the near-infrared region. In the last decades, Pcs were probed as a hole-injection layer in organic light emitting diodes and¹³⁰ also light absorbers and sensitizers in dye-sensitized solar cells,¹³¹⁻¹³³ with device efficiencies still lagging below 6%. The optical and electrical properties of these macrocycles can be easily tuned by varying the metal center and the peripheral substituents,^{134, 135} while the supramolecular organization and crystal packing can be modified by properly substituting the macrocycle, leading to the formation of different condensed phases where the charge transport is enhanced along columnar stacks or aggregates.¹³⁶ Moreover, a low cost one-step synthesis and a simple purification process make these molecules promising candidates to be explored in light harvesting, photovoltaic, and molecular photonic modules.¹³⁷ Recently, higher efficiencies were obtained when employing Pcs as HTM using commercially available Cu(II)phthalocyanines.¹⁰⁹ Solar cells employing Zn(II)phthalocyanine have been also studied by incorporating an Al₂O₃ interlayer to reduce charge recombination¹³⁸ with efficiencies lagging far from those obtained with Spiro-OMeTAD.

In this work, we employed three different Zn(II)Pcs, where *tert*-butyl, hexylthiophene, or hexylbisthiophene groups have been intentionally incorporated into Pcs (**Figure 64**), to probe their capabilities as efficient, stable, and low cost hole-transport materials. Our results suggest a crucial role of the molecular aggregation of Pcs in HTM layers in the charge transport properties. By combining these materials with the high efficient mixed-ion perovskite light harvester [FAPbI₃]_{0.85}[MAPbBr₃]_{0.15}, maximum power conversion efficiencies of 17.5% (17.1% average) have been achieved. Our findings suggest that proper substitution in Zn(II)phthalocyanines could further boost the commercialization of perovskite solar cells, giving a chance to find their place in the photovoltaic market.

7.3. Results and Discussion

7.3.1. Synthesis and characterization of Zn(II)Pc

The three different ZnPc derivatives shown in **Figure 64** were tested as hole-transporting materials in PSCs. The novel highly π -conjugated tetra-5-hexyl-2,2'-bisthiophene-substituted Zn(II)Pc (HBT-ZnPc) was prepared in one step by Pd(PPh₃)₄-catalyzed cross-coupling between tetraiodo-substituted ZnPc¹³⁸ and hexylbisthiophene-boronic acid pinacol ester in 43% (Scheme S1, Supporting

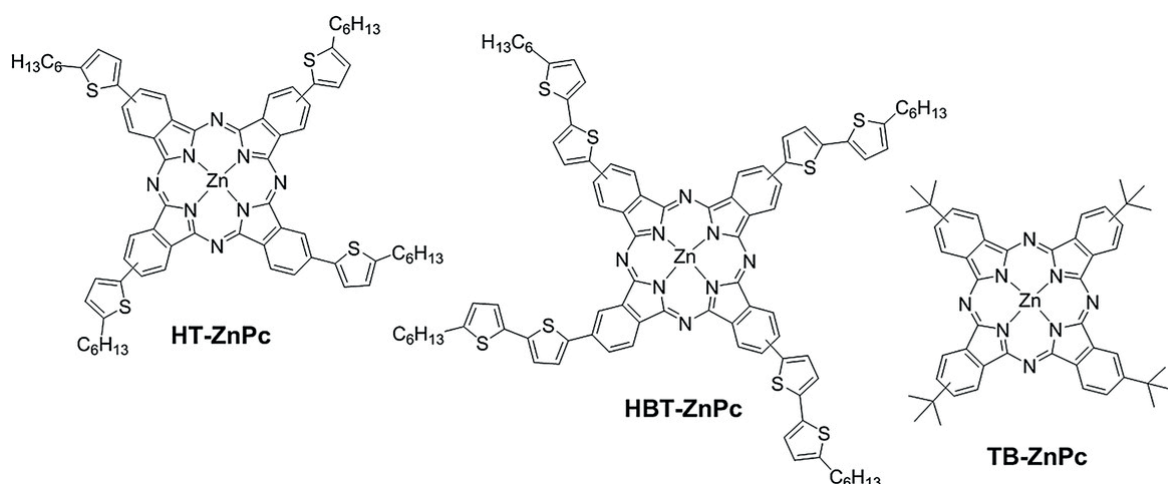


Figure 64. Chemical structures of HT-ZnPc, HBT-ZnPc, and TB-ZnPc.

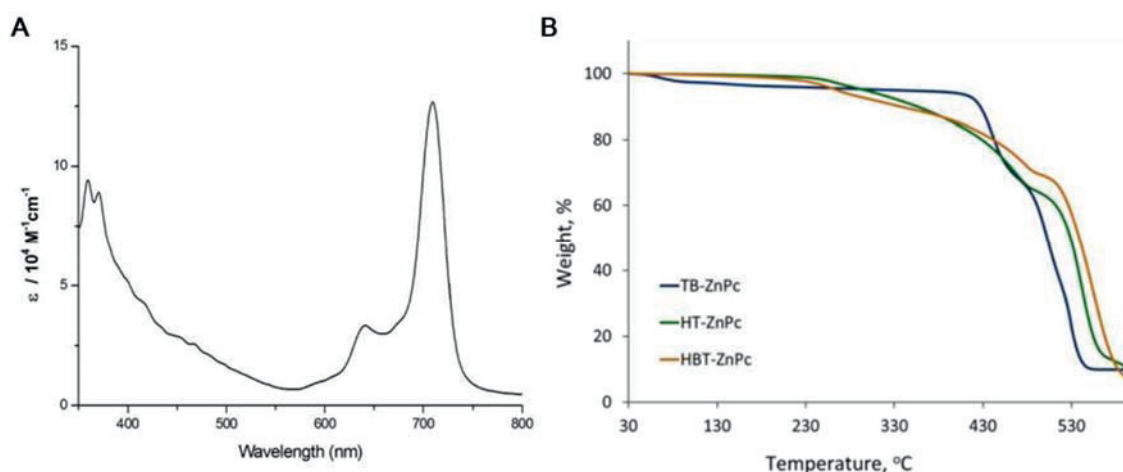


Figure 65 a) UV-vis spectrum of HBT-ZnPc (10⁻⁵M solution in THF). B) Thermogravimetric analysis of HT-ZnPc, HBT-ZnPc and TB-ZnPc in air at scan rate of 10 °C min⁻¹.

Information). The synthesis of tetra-5-hexylthiophene-substituted Zn(II)Pc (HT-ZnPc) has been reported elsewhere,¹³⁹ while tetra-*tert*-butyl-substituted Zn(II) phthalocyanines (TB-ZnPc) was purchased from commercial supplier. All compounds were used as mixtures of the corresponding regioisomers. Their good solubility in most of organic solvents was found to be especially useful for solution-processed HTM deposition. Thermogravimetric analysis (TGA) of the three ZnPcs in air revealed that the TB-ZnPc exhibits a good thermal stability up to 420 °C, resulting in 88% weight loss by 550 °C (**Figure 65b**, Supporting Information). The presence of thiophenes in HT-ZnPc and HBT-ZnPc, however, triggered their degradation starting from 220 °C.

7.3.2. Energy level alignment

Absorption measurements of ZnPc solutions in dichloromethane (DCM) shed light on some ground state features of these dyes. As it can be observed from **Figure 66a**, TB-ZnPc exhibits the typical Q-band absorption maxima at 665 nm. This signature appears bathochromically shifted for thiophene-substituted HT-ZnPc to 690 nm and further to 702 nm for HBT-ZnPc as a consequence of an extended conjugation. More importantly, a strongly pronounced tendency toward aggregation has been evidenced for thiophene-substituted HT-ZnPc and HBT-ZnPc 10^{-6} m solutions in DCM,

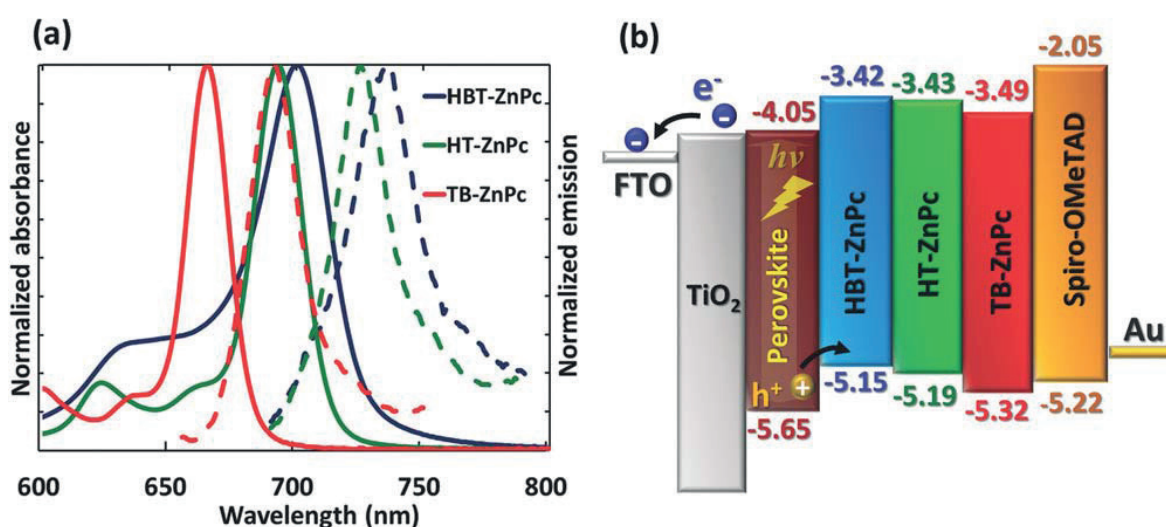


Figure 66. a) UV-vis absorption (solid line) and emission (dashed line) spectra of HT-ZnPc, HBT-ZnPc, and TB-ZnPc in DCM. b) Energy band diagram of the materials involved in the solar cell architecture (all values in eV).

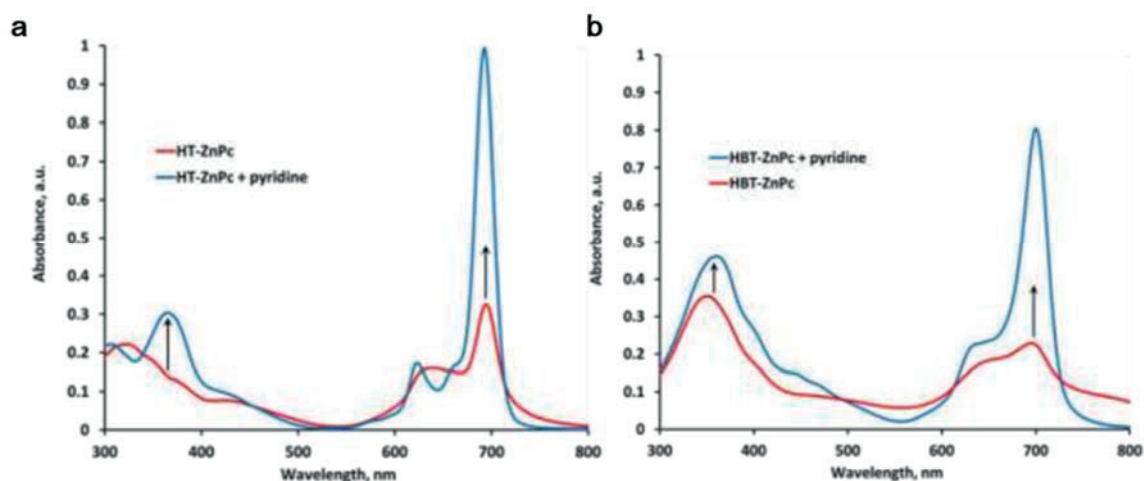
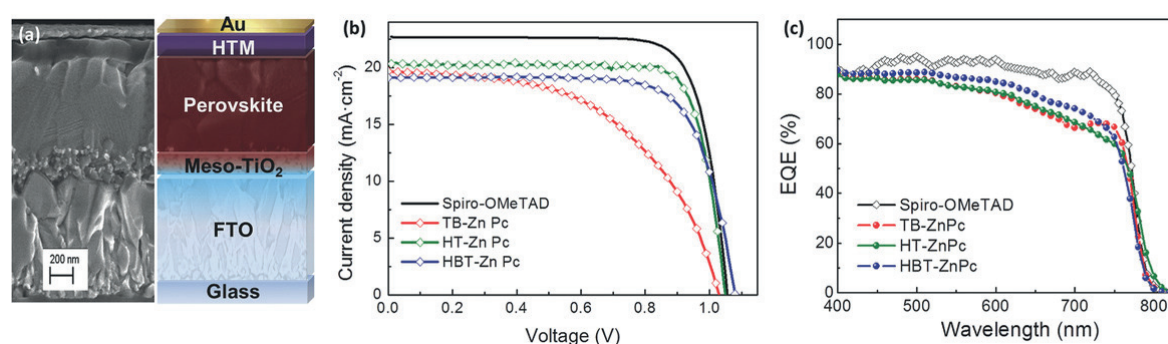


Figure 67. Effect of addition of pyridine on the UV-vis absorption (DCM) of HT-ZnPc (a) and HBT-ZnPc (b).

Table 5. Optical and electrochemical characteristics of the compounds

HTM	λ_{abs} [nm]	λ_{em} [nm]	E_{0-0} [eV]	E_{ox}^1 [V] versus NHE	$E_{\text{HOMO(a)}}$ [eV]	$E_{\text{LUMO(b)}}$ [eV]
TB-ZnPc	666	690	1.83	0.88	-5.32	-3.49
HT-ZnPc	692	725	1.75	0.75	-5.19	-3.44
HBT-ZnPc	701	734	1.73	0.71	-5.15	-4.42

**Figure 68.** a) SEM cross-section image of a typical device, b) current density versus voltage ($J-V$) curves and, c) EQE as a function of wavelength obtained for Pc-HTMs and Spiro-OMeTAD based PSCs.

resulting in a strong absorption increase of Q-band maxima upon addition of pyridine (**Figure 67**).¹⁴⁰ Similar behavior was also revealed for “bulkier” TB-ZnPc at higher concentrations. The optical band gaps (E_{0-0}) were estimated from the intersection of the corresponding normalized absorption and emission spectra, thus, resulting in 1.75 and 1.73 eV for HT-ZnPc and HBT-ZnPc, respectively. TB-ZnPc revealed a larger E_{0-0} of 1.83 eV. These results, combined with cyclic voltammetry data, allowed the estimation of the highest-occupied and lowest-occupied molecular orbital energy levels (HOMO and LUMO respectively), summarized in **Table 5**. Notably, an addition of four thiophene rings on the periphery of ZnPc core increased its first oxidation potential by 130 mV, compared to TB-ZnPc, whereas an addition of four conjugated bithiophenes in HBT-ZnPc further raised the first oxidation potential by 40 mV. The energy diagram of the $\text{TiO}_2/(\text{FAPbI}_3)_{0.85}(\text{MAPbBr}_3)_{0.15}/\text{HTM}/\text{Au}$ devices comparing different HTMs is shown in **Figure 66b**. Assuming the valence band of mixed-ion perovskite to be at -5.65 eV (vs vacuum),¹⁴¹ all ZnPcs show enough overpotential leading to efficient charge extraction at the HTM interfaces. However, the HOMO levels of HT-ZnPc and HBT-

ZnPc are lying higher comparing with that of some efficient HTMs like Spiro-OMeTAD (-5.22 eV vs vacuum),¹⁴² thus, a lower open circuit voltage (V_{oc}) can be expected.

7.3.3 Application to PSCs and Performances.

To further analyze the behavior of TB-ZnPc, HT-ZnPc, and HBT-ZnPc as suitable HTMs, hybrid organic–inorganic perovskite solar cells were fabricated. The devices were made using a standard configuration where the optimized $[FAPbI_3]_{0.85}[MAPbBr_3]_{0.15}$ perovskite absorber was sandwiched between TiO_2 -blocking layer/ TiO_2 -mesoporous layer as ETM and the ZnPcs as HTM (**Figure 68a**). The electron-transporting layer was fabricated as described in the Supporting Information of this article. The perovskite thin film was deposited by using a single-step spin-coating procedure employing chlorobenzene as antisolvent.³¹ The hole-transporting layers were spin-coated on the top of perovskite film using chlorobenzene solutions. A small amount of dopants was used in both cases, ZnPcs and Spiro-OMeTAD, to enhance their conductivity. Further details about the solution preparation and deposition parameters can be found in the Supporting Information. Solar cells with Spiro-OMeTAD-based hole-transporting layer were also fabricated as reference cells. Finally, 80 nm thick gold layer was deposited on the top of the HTM, completing the solar cell configuration.

The current density–voltage (J – V) curves and the key photovoltaic parameters of the solar cells recorded under standard AM1.5G illumination are summarized in **Figure 68b** and **Table 6**. Devices of the best performances and those of average characteristics are shown. In general, ZnPc-based perovskite solar cells exhibited reasonable performances in all cases, with open circuit voltages (V_{oc}) above 1.05 V. However, a strong influence of the ZnPc derivative employed in each case was

Table 6. Photovoltaic parameters of representative ZnPc-based PSCs of average performance in comparison with reference best performing Spiro-OMeTAD PSC

HTM	J_{sc} [$mA\ cm^{-2}$]	V_{oc} [V]	FF [%]	PCE [%]
TB-ZnPc	20.19	1.03	66.3	13.3
HT-ZnPc	20.28	1.05	80.3	17.1
HBT-ZnPc	20.16	1.10	69.4	15.5
Spiro-OMeTAD	23.01	1.07	77.8	19.1

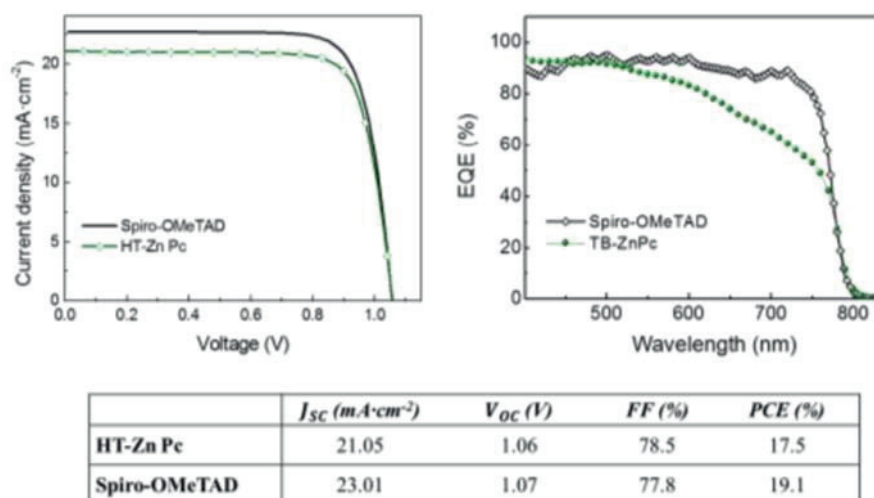


Figure 69. J-V curve and EQE measured for one of the highest efficient cells under AM 1.5G illumination in ambient atmosphere.

observed, leading to substantial differences mainly of the fill factor (FF). Compared with Spiro-OMeTAD, which exhibited a short circuit current (J_{sc}) of 23 mA cm^{-2} , the TB-ZnPc showed slightly lower J_{sc} of nearly 20 mA cm^{-2} , and a considerably reduced FF of $\approx 65\%$. We attributed this behavior to a higher series-resistance (R_s) in the device, resulting in a lower conductivity for the HTM layer. As a consequence, a drop in PCE from 19% to 13.3% occurred for TB-ZnPc. PSCs containing HT-ZnPc derivative led to a comparable current density (20.3 mA cm^{-2}) but a record FF, in some cases, superior than that obtained with Spiro-OMeTAD, with impressive values of 80%. This resulted in a record value of 17.5% (**Figure 69**), which is the highest reported for phthalocyanines-based HTMs. However, the introduction of a bis-thiophene unit (HBT-ZnPc) caused an unexpected detrimental effect, decreasing considerably both the J_{sc} (below 20 mA cm^{-2} in most of the cases) and the FF of 69%, resulting in a reduced efficiency with an average value of 15.5% (see **Table 5**). These observations are particularly interesting since the chemical structures of both, HT-ZnPc and HBT-ZnPc, are rather similar, resulting in comparable values for HOMO, LUMO, and E_{0-0} . Our findings clearly underline the important influence of the molecular packaging on the final optoelectronic properties on the solid film. Overall, the replacement of four *tert*-butyl groups by four 5-hexylthiophene moieties led to a significant increase of PCE from 15.1% to 17.5% (maximum values), a record efficiency which opens up new frontiers toward abundant, efficient, and low cost alternatives to Spiro-OMeTAD.

Figure 68c summarizes the external quantum efficiency (EQE) as a function of wavelength of ZnPc-based devices, and that of Spiro-OMeTAD. As clearly observed, the EQE from all HTMs is very similar at high energy wavelengths, staying close to $\approx 90\%$ conversion for all the cells. Interestingly, the presence of ZnPc derivatives causes a strong decrease above ≈ 600 nm. We associate the reduced EQE at larger wavelength to the absorption of phthalocyanines, as they exhibit a strong absorption band from ≈ 580 to 790 nm. As a consequence, they can reduce considerably the fraction of current generated by the second pass of reflected light from the gold electrode (**Figure 70**). As the perovskite film exhibits higher absorption coefficient at shorter wavelengths, this effect can be observed only for low energy photons. Compared with Spiro-OMeTAD, which is transparent in the visible range, phthalocyanines absorb part of this light, causing a decrease in the incident photon-to-current conversion efficiency (IPCE) above 590 nm. Interestingly, comparing the performance of the record cell obtained for HT-ZnPc with the state-of-the-art Spiro-OMeTAD, it can be observed that the main loss in efficiency is due to the lower J_{sc} , while V_{oc} and FF are within the same range of values. Additionally, a pronounced hysteresis behavior was observed for $J-V$ curves of all studied Pcs under forward and reverse bias measured under AM 1.5G illuminations in ambient atmosphere at a constant rate 10 mV s^{-1} , most likely caused by the interface between the perovskite and HTM layer (**Figure 70**). These results suggest that further investigations toward larger band gap Pc derivatives are promising in order to maintain the fraction of current generated by the second pass. More information

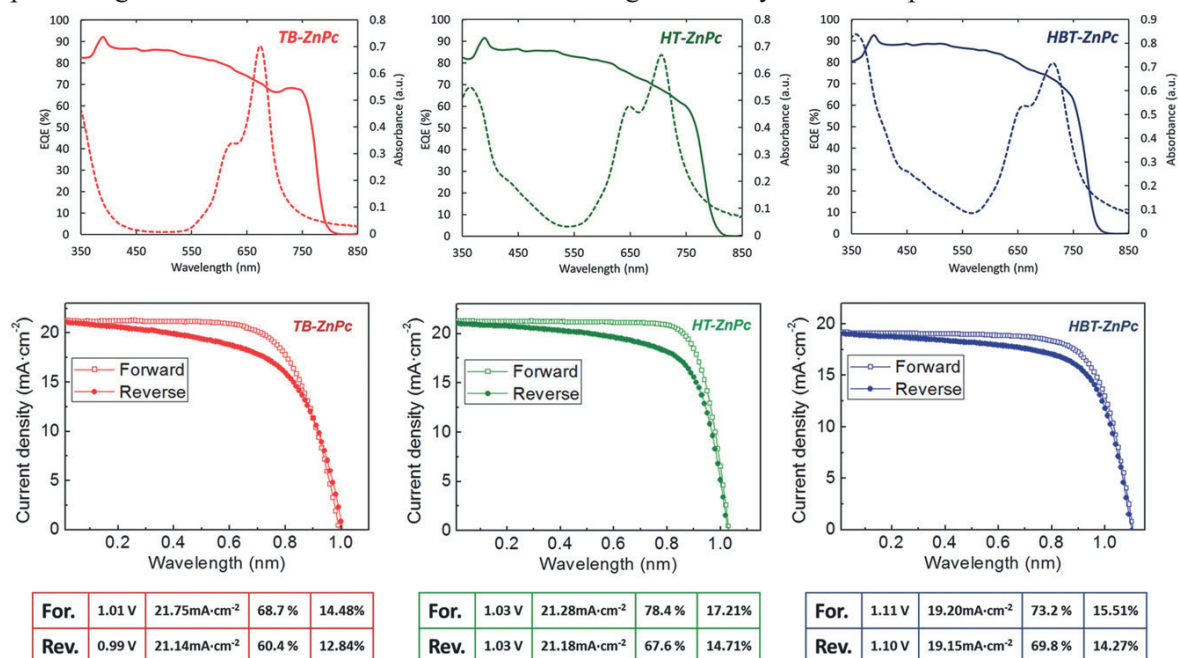


Figure 70. (Top) EQEs of ZnPc-based perovskite solar cells and UV-vis absorption spectra of the corresponding ZnPc thin films on glass substrates, containing the same amount of dopants as used in device fabrication. (Down) $J-V$ curve under forward and reverse bias measured for ZnPc-based PSCs under AM 1.5G illuminations in ambient atmosphere. The cell was measured without encapsulation at a constant rate 10 mV s^{-1} .

regarding device performance, reproducibility, as well as the performance of the record cells can be found in **Figure 71**.

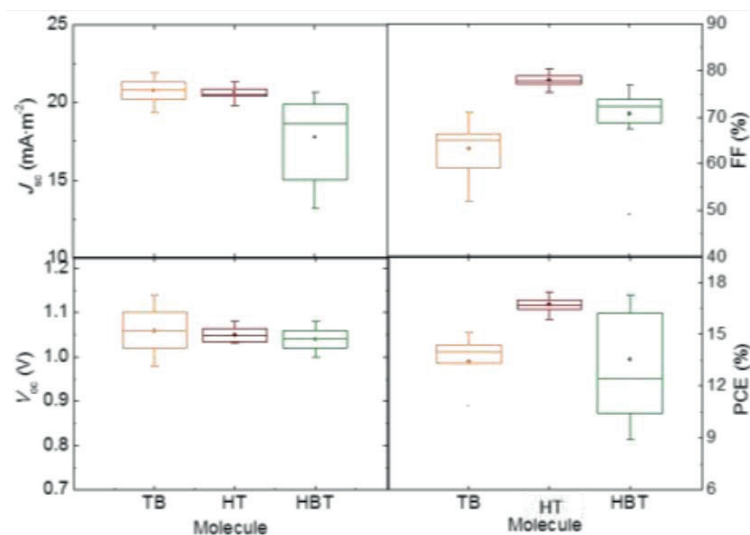
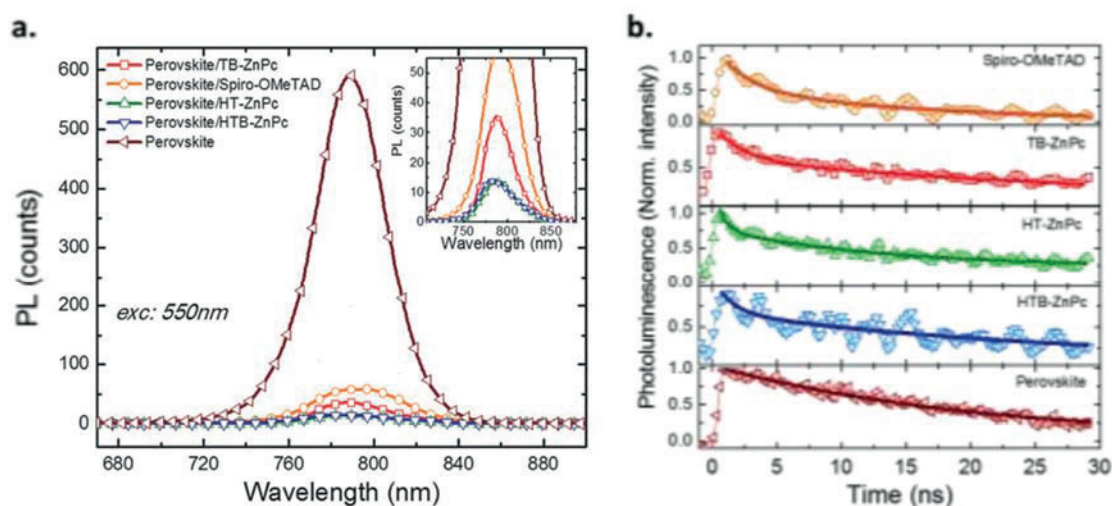


Figure 71. Average values obtained for perovskite solar cells employing TB-ZnPc, HT-ZnPc and HBT-ZnPc as hole-transport materials.



	τ_1 (ns)	τ_2 (ns)	A_1	A_2	A_1 (%)	A_2 (%)
Perovskite		27	1	-	100	-
TB-ZnPc	2.1	33	0.47	0.63	43.06	56.93
HT-ZnPc	1.0	33	0.55	0.92	37.41	62.58
HBT-ZnPc	1.4	27	0.50	0.71	41.32	58.68
spiro-OMeTAD	2.2	33	0.70	0.55	56.00	44.00

Figure 72. a) Steady-state fluorescence spectra obtained for Glass/perovskite/Pc-HTM substrates excited from the HTM side. Pure perovskite and perovskite/Spiro-OMeTAD samples are also included as a reference. b) Time resolved photoluminescence decay at 770nm obtained for all samples when exciting at 550nm from the HTM side. The fitting parameters are depicted in the table below.

7.3.4. Photoluminescence and hole transporting Analysis.

As mentioned, the proper energy level alignment of the Pc/perovskite interfaces would allow efficient hole-transfer pathway. To further demonstrate this mechanism, we monitored the photoluminescence (PL) of the perovskite/Pc bilayer, to exclusively target the interfacial behavior. The perovskite film deposited on glass has been covered with the different Pc-HTMs, deposited in the same conditions as during device preparation. Both, steady-state PL and time-resolved PL evolution in the nanosecond regime have been monitored. Pristine perovskite film without the HTM has also been measured as a reference. Upon excitation at 550 nm, the bilayer samples containing different HTM on top showed in all cases a quenched emission with respect to the pristine perovskite, indicative of an effective hole-transfer happening at the heterojunction, as it can be observed in **Figure 72a**. The PL decay for all samples showed similar trends: the decay is dominated by a fast component with a time constant ≈ 2 ns (see **Figure 72b**), much shorter with respect to the long-living signal of the perovskite-only film (with a decay time constant beyond our temporal window). This behavior is observed for all Pc-HTM, with TB-ZnPc and HTB-ZnPc both exhibiting a faster time decay with amplitude, however, slightly lower than those of Spiro-OMeTAD. The PL quenching with respect to the pristine perovskite film indicates that hole-transfer is a viable and efficient interfacial mechanism, in accordance with the energy level landscape previously retrieved.

Assuming that the three ZnPcs possess comparable energy levels for the proper hole-injection, and taking into account the similarities in their chemical structures, we further considered the influence of a specific molecular packing of ZnPcs in HTM films as a potential reason of their different performance. Metal Pcs in thin films are usually stacked, forming columns with the macrocycle tilted in relation to the column vertical axis.¹⁴³ Such specific organization affects not only the optical properties of the material but also the conductivity of the films, leading to anisotropy in their optoelectronic properties, i.e., asymmetric hole-mobility within the layer.¹⁴⁴ This property can be further affected, for instance, by an incorporation of bulky-substituents in the Pc core, decreasing the hole-extraction as a consequence of a lower intermolecular contact.¹¹⁶ Molecular tilting, rotations, or lateral displacement of the macrocycles within the aggregate can further enhance the anisotropy of a system, increasing the resistivity toward charge migration.¹⁴⁵ Resuming, the supramolecular packing represents a complex phenomenon that, however, can easily affect the performance of the entire molecular system such as hole-transporting layer, and, ultimately, the resulting solar cell performance. Taking the before mentioned into account, we have studied the properties of HTM thin films, to reveal a relationship between the charge-carrier transport characteristics of ZnPc-based HTM layers and the observed photovoltaic performance of perovskite solar cells.

Ground-state features of ZnPc-based hole-transporting layers were studied by steady-state absorption of the corresponding thin films on glass substrates, containing the same doping composition as during device fabrication. All ZnPc-based hole-transporting layers exhibited characteristic ≈ 10 nm blue-shifted broaden Q-band maxima if compared to the corresponding ZnPc signatures in solutions (Figures 66a and 70). The latter was associated with the formation of aggregates. Notably, the presence of *tert*-butylpyridine (TBP) as one of the dopants in all the films should have enhanced the anisotropy of the ZnPc packing.¹⁴⁰ As a matter of fact, no steady-state emission has been detected for the studied films, confirming the presence of close intermolecular contacts between ZnPcs in the thin film, accounting for the quenching.

The lateral conductivity of thin films of different ZnPcs was measured between 2.5 μm spaced interdigitated gold electrodes. Films were fabricated in the same way as for PSCs, containing 5 mol% of FK209 as a dopant. Intentionally, film with tetra-*tert*-butyl copper phthalocyanine (TB-CuPc) has been also analyzed instead of that of Spiro-OMeTAD. In fact, TB-CuPc yielded the highest 15.2% PCE among Pc-based perovskite solar cells,¹⁰⁹ remaining the aforementioned molecular stacking behavior typical for Pcs. Figure 73a shows the conductivity values obtained for the three ZnPc and a reference TB-CuPc films. HBT-ZnPc and TB-ZnPc layers exhibited the lowest conductivities of 6.0×10^{-7} and 5.0×10^{-7} S cm^{-1} , respectively. Surprisingly, the HT-ZnPc film revealed the conductivity similar to that of TB-CuPc (8.0×10^{-5} and 4.0×10^{-5} S cm^{-1} , respectively), being both comparable with that of Spiro-OMeTAD.¹⁴⁶ In summary, the conductivity trend clearly supports the observed difference in the device performance, suggesting the optimal packing of HT-ZnPc within employed thin films for the proper photovoltaic output.

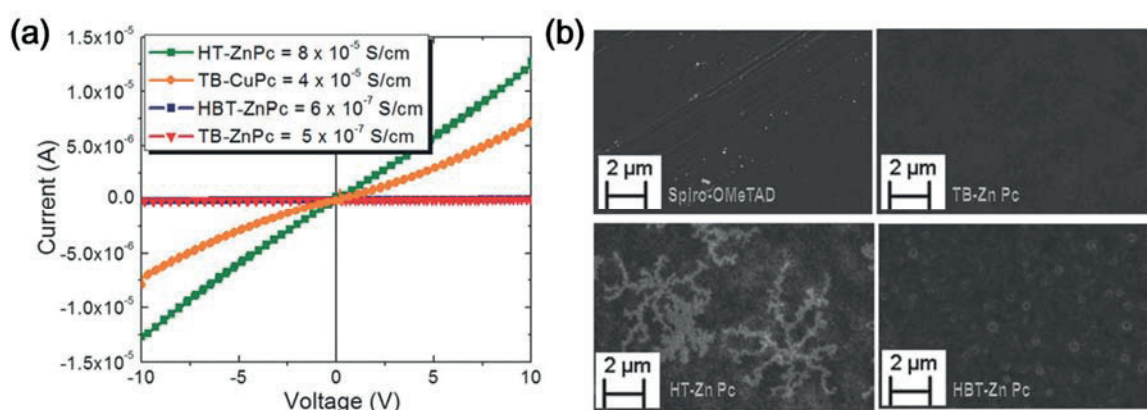


Figure 73. a) Lateral conductivity of the doped HTMs given in comparison with tetra-*tert*-butyl CuPc. b) SEM top-images of devices fabricated with different HTMs.

7.3.5. Morphology and Crystallization

Scanning electron microscopy (SEM) was used to analyze the topology of HTM layers after their deposition on the perovskite material. SEM top-images of all films, including Spiro-OMeTAD, as one of the fabricated devices, are displayed in **Figure 73b**. Both, Spiro-OMeTAD and TB-ZnPc present a very homogeneous surface of their films where no special features could be distinguished within a micrometer to nanometer range. On the contrary, some aggregation was identified in the HBT-ZnPc layer, with circular domains different in size and shape. Most surprisingly, the flower-type branched micrometer-size aggregates were formed by HT-ZnPc molecule in a reproducible manner. Speculatively, these structures might be responsible for the outstanding performance of HT-ZnPc as HTM for Pcs. This finding clearly supports the huge influence of the Pc structural peculiarities on a scale of a single molecule on the final electrical properties of films and bulk material, through subtle and difficult to define in the solid state aggregation features of these macrocycles.

In order to disclose possible ordered or semicrystalline ZnPc-based structures within the thin films, grazing incidence wide-angle X-ray scattering technique (GIWAXS) was employed to reveal characteristic scattering signals. An incidence angle of X-ray below the critical angle of HTM layer was used. Corresponding ZnPcs were spin-coated from their chlorobenzene solutions on top of perovskite layer, following the same procedure as during device fabrication. The obtained 2D GIWAXS patterns for individual films are represented on **Figure 74**. Several intense halo peaks corresponding to the underlying perovskite layer were visible in all the samples, being assigned to the perovskite (110). Scrutinizing the diffraction region of ZnPc layers, it has been found that most PCs are quite poorly ordered, most likely due to the presence of dopants. For the HT-ZnPc sample,



Figure 74. 2D GIWAXS images of (a) HT-ZnPc (b) HBT-ZnPc and (c) TB-ZnPc. GIWAXS samples were prepared with similar procedures as device fabrication. Doped with LiTFSI, FK209 and TBP, HTMs were spin-coated on the underlying perovskite film.

- 2D GIWAX Measurements GIWAXS measurements were performed by means of a solid anode X-ray tube (Siemens Kristalloflex X-ray source, copper anode X-ray tube operated at 35kV and 40mA), Osmic confocal MaxFlux optics, X-ray beam with pinhole collimation and a MAR345 image plate detector. The beam size was 0.5×0.5 mm and samples were irradiated just below the critical angle for total external reflection for X-ray beam ($\sim 0.18^\circ$). Data analysis was carried out with Datasqueeze software.

no reflections were observed, indicating that the HT-ZnPc domains are very amorphous or mainly oriented perpendicular to the top surface. However, reflection at 1.28 nm is observed for HBT-ZnPc, being in agreement with the value typical for the (100)-oriented brickstone structure.¹⁴³ For TB-ZnPc, only one isotropic reflection at *d*-spacing of 1.49 nm is observed, clearly stating a disordered morphology in the film. No clear evidence of crystalline-like structures has been found for any of the studied ZnPc-based films, thus, confirming the amorphous character of Pc stacks within hole-transporting layers.

7.4. Conclusion

In summary, we investigated a series of easily accessible zinc phthalocyanines as hole-transporting materials in mixed-ion perovskite [FAPbI₃]_{0.85}[MAPbBr₃]_{0.15} solar cells overcoming the record power conversion efficiency reported to date for phthalocyanines. The optimized devices exhibited PCE of 15.5% when using tetra-5-hexyl-2,2'-bisthiophene substituted ZnPcs, 13.3% for tetra-*tert*-butyl ZnPc, and outstanding 17.5% for tetra-5-hexylthiophene-based analogue under standard global AM 1.5 illumination. Worthy to highlight, the latter cells showed very high FF superior to those of Spiro-OMeTAD, with impressive values surpassing 80%. The resulting difference in photovoltaic performance was rationalized in terms of individual optoelectronic properties of ZnPcs and their aggregation in a condensed HTM layer employing steady-state absorption and emission, time-dependent PL, conductivity measurements, SEM, and GIWAXS techniques. Formation of the amorphous aggregated structures in the ZnPc-based HTM layer was concluded to enhance drastically the resulting device performance. These results boost up the potential large-scale applications of solution-processed ZnPc derivatives as stable and economic hole-transport materials, opening new frontiers toward a realistic, efficient, and inexpensive energy production.

7.5. Experimental section

7.5.1. Synthesis and characterization

Chemicals were purchased from commercial suppliers and used as received. Air sensitive reactions were carried out under argon atmosphere. Column chromatography was carried out using silica gel Merck-60 (230-400 mesh, 60 Å) as the solid support. TLC analyses were performed on aluminum sheets precoated with silica gel 60 F254 (E. Merck). Size-exclusion chromatography (GPC) was carried out using Bio-Beads S-X1 support (BIO-RAD) as a stationary phase and THF as a mobile

phase. Matrix-assisted laser desorption ionization (coupled to a time-of-flight analyzer) experiments (MALDI-TOF) were carried out using Autoflex III mass spectrometer (Bruker Daltonics) in positive mode. NMR spectra were measured on a Bruker AC-400 instrument, locked on deuterated solvents. UV-vis spectra were recorded on Analytic JENA S 600 and Perkin Elmer UV-vis spectrophotometers in spectroscopic grade solvents. IR spectra were collected on Perkin-Elmer, FT-IR spectrophotometer (ATR = Attenuated total reflectance). Cyclic voltammograms (CV) and differential pulse voltammograms (DPV) were recorded on BioLogic SP200 potentiostat. Measurements were carried out in a home-built onecompartment cell using a three-electrode configuration, dichloromethane (DCM) as a solvent and 0.1 M tetrabutylammonium hexafluorophosphate (TBAPF6) as a supporting electrolyte. A carbon-glassy electrode was used as the working electrode and platinum coil as a counter electrode. All potentials were recorded against a platinum wire pseudo-reference electrode and corrected against Fc^+/Fc redox couple. DPV and CV were measured at scan rates of 20 and 100 mVs⁻¹, respectively. Prior to each voltammetric measurement, the cell was degassed by bubbling with argon for about 20 min. Electrochemical measurements were performed using a concentration of approximately 1×10^{-3} M for the compound in question. Thermogravimetric analysis (TGA) was performed using a TGAQ500 instrument with a ramp of 10 °C/min under N₂ from RT to 600 °C. - Synthesis of 2(3), 9(10),16(17),23(24)-tetra[5'-hexyl-2,2'-bithiophene]-phthalocyaninato (2-)-N 29, N30, N31, N32 zinc(II) (HBT-ZnPc)

A suspension of tetra-iodo Zn(II)Pc (50 mg, 0.046 mmol), bithiophene-boronic acid pinacol ester (105 mg, 0.28 mmol), Pd(PPh₃)₄ (5.3 mg, 0.0046 mmol) and a solution of Na₂CO₃ (100 mg, 0.1 mmol) in H₂O (1 mL) in dimethoxyethane (10 mL) was stirred at 95 °C under argon atmosphere for 24 h. The mixture was then cooled at room temperature and poured into a 1M NH₄Cl aqueous solution (100 mL). The suspension was extracted with ethyl acetate (3 × 25 mL) and the combined organic layers were dried over MgSO₄, filtered and evaporated in vacuo. Column chromatography of the crude product on silica gel (hexane/dioxane = 6:1, vol.), following size-exclusion chromatography (Bio-Beads SX1, THF) afforded pure compound (31 mg, 0.02 mmol) as a green solid. Yield: 43%. ¹H NMR (d₈-THF, 400 MHz): δ (ppm) = 9.2-8.6 (m, 9H), 8.2-7.9 (m, 5H), 7.9-7.8 (m, 1H), 7.8-7.7 (m, 3H), 7.4-7.2 (m, 7H), 6.9-6.8 (m, 3H), 3.0-2.8 (m, 8H), 1.9-1.7 (m, 8H), 1.4-1.3 (m, 24H), 1.06-0.9 (m, 12H). UV-vis (THF): λ_{max}, nm (log ε): 710 (5.10), 641 (4.52), 358 (4.96). IR (ATR): ν = 2919, 2850, 1734, 1605, 1490, 1450, 1331, 1255, 1050, 891. MS (MALDI-TOF) m/z: calc. for C₈₈H₈₀N₈S₈Zn: 1568.356; found 1568.413 [M]⁺.

7.5.2. Solar Cells Preparation

Device preparation Devices were fabricated on fluorine doped tin oxide (FTO) coated glass substrates. The substrates were cleaned sequentially with Hellmanex and Milli Q grade distilled water in 6 ultrasonic bath for 15 min, then washed with isopropanol. Prior to the deposition of any functional layer, UV-ozone surface treatment was performed for 15 min to remove any remaining traces of organic material. A 30 nm TiO₂ compact layer was deposited on FTO via spray pyrolysis at 450°C from a precursor solution of titanium diisopropoxide bis(acetylacetonate) in anhydrous ethanol. Then, substrates were left at 450°C for 30 min and cool down to room temperature. Mesoporous TiO₂ layer was deposited by spin coating for 20 s at 2000 rpm with a ramp of 1000 rpm s⁻¹, using 30 nm particle paste (Dyesol) diluted in ethanol to achieve 150 nm thick layer. After the spin coating, the substrate was immediately dried at 100°C for 10 min and then sintered again at 500°C for 30 min, under dry air flow. Upon cooling to room temperature, the perovskite layer was deposited in a nitrogen-filled glovebox by spin coating the perovskite precursor solution. The spin coating program includes two steps, first 1000 rpm for 10 s with a ramp of 200 rpm s⁻¹, then 6000 rpm for 30 s with a ramp of 2000 rpm s⁻¹. 12 s before the end of the spin-coating program, chlorobenzene was gently dropped on the spinning substrate for 2 s. The substrate was then heated at 100°C for 80 min on a hotplate in the nitrogen-filled glovebox. The HTM solutions were prepared dissolving the molecule in chlorobenzene at Pc concentration of 30 mM, with the same doping composition we used for the Spiro-OMeTAD solution. The HTM layer was finally deposited by spin coating from solution at 4000 rpm for 20 s with a ramp of 2000 rpm s⁻¹. Finally, 80 nm of gold was deposited by thermal evaporation under high vacuum, using a shadow masking to pattern the electrodes.

7.5.3. Characterization

High resolution cross-section images of the finished devices were recorded with a ZEISS Merlin HR-SEM scanning electron microscope. Current-voltage characteristics were measured in air under AM 1.5 simulated sunlight with Keithley potentiostat. The light intensity was measured for calibration with an NREL certified KG5 filtered Si reference diode. The solar cells were masked with a metal aperture of 0.16 cm² to define the active area. The current-voltage curves were recorded scanning at 10 mVs⁻¹ from forward scan to short circuit and vice versa, with a preconditioning of the device with light during 3s before the scan.

Chapter 8. ETL Investigation

(Beneficial role of reduced graphene oxide for electron extraction in highly efficient perovskite solar cells)

This chapter was published as the above title in ChemSusChem, 2016, 9, 3040-3044

In authors (Kyung Taek Cho, Giulia Grancini, Yonghui Lee, Dimitrios Konios, Sanghyun Paek, Emmanuel Kymakis, Mohammad Khaja Nazeeruddin), I was the main author. I designed experiments and fabricated devices by graphene prepared by other co-authors.

8.1. Abstract

In this work we systematically investigated the role of reduced graphene oxide (rGO) in hybrid perovskite solar cells (PSCs). By mixing rGO within the mesoporous TiO₂ (m-TiO₂) matrix, highly efficient solar cells with power conversion efficiency values up to 19.54 % were realized. In addition, the boosted beneficial role of rGO with and without Li-treated m-TiO₂ is highlighted, improving transport and injection of photoexcited electrons. This combined system may pave the way for further development and optimization of electron transport and collection in high efficiency PSCs.

8.2. Introduction

Since its isolation in 2004,¹⁴⁷ graphene has had a huge impact on applications in optoelectronic and photon energy conversion, owing to its unique electronic, optical, and mechanical properties.¹⁴⁸⁻¹⁵¹ The development of solution-processable graphene, such as the chemical exfoliation of graphite into graphene oxide, allowed the functionalization and processing of graphene, extending its use in the different layers of solution-processable solar cells.^{152, 153} Among different solar cell technologies, organic–inorganic hybrid perovskite solar cells (PSCs) have been dominating the interest of the scientific research community for their impressive technological development with power conversion efficiency (PCE) values beyond 22 % in a short of six years of research.² However, further improvements are necessary to optimize the PSC device operation and stability, and enhance the device performance. From this point, mixed graphene-based derivatives have been proposed to further enhance the device properties.¹⁵³ Used in various forms and with different functionalities, either incorporated in mesoscopic or in planar device configuration,^{154, 155} functionalized reduced graphene oxide (rGO) derivatives have been successfully employed for improved charge extraction in the electrontransport material (ETM)^{154, 156, 157} or hole-transport material (HTM)¹⁵⁸ in PSCs. Its ability to effectively reduce the chargerecombination pathways and decrease the leakage currents has been demonstrated, with a similar role as in organic solar cells.¹⁵⁹⁻¹⁶¹ However, all of the PCEs reported are limited to less than 14 % and the perovskite was not formed as a perfect film, which casts the doubt on the real beneficial role of rGO on high-efficiency PSCs. In contrast to many applications of carbon-based materials that are usually introduced at the perovskite/TiO₂ or perovskite/HTM interfaces, or in substitution of the HTM itself,^{162, 163} here we propose a systematic study by exploring three different configurations as shown in **Figure 75**.

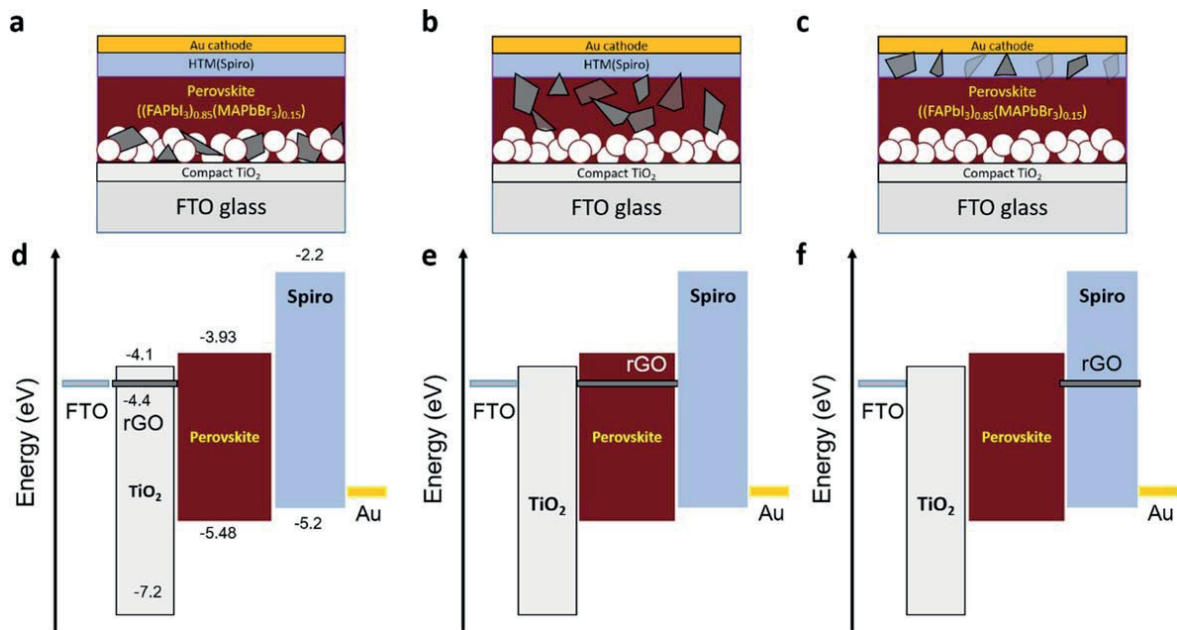


Figure 75. Illustration of the solar cells architectures fabricated with rGO in each layer: (a) m-TiO₂+rGO, (b) perovskite+rGO, and (c) spiro-OMeTAD+rGO. (d–f) The corresponding energy level diagram of these three devices. These energy levels are based on the individual materials; within the solar cell and under illumination there will be a relative shift.

8.3. Results and discussion.

We integrated the rGO: 1) within the mesoporous TiO₂ (m-TiO₂) ETM, 2) in the matrix of the active perovskite layer, and 3) in the 2,2',7,7'-tetrakis(*N,N'*-di-*p*-methoxyphenylamine)-9,9'-spirobifluorene (spiro-OMeTAD) HTM. In this study, mesoscopic PSCs are composed of a fluorine doped tin oxide (FTO)-coated glass substrate, a compact TiO₂ layer followed by a m-TiO₂ layer, a mixed (FAPbI₃)_{0.85}(MAPbBr₃)_{0.15} (FA=formamidinium, MA=methylammonium) perovskite layer that infiltrates into the m-TiO₂, a spiro-OMeTAD layer, and a Au counter electrode.¹²⁹ We investigate the effect of the introduction of the rGO flakes in each layer comparing the results with control cells without rGO. Furthermore, to better examine the effect of rGO in the ETM, we compared devices with and without treating the TiO₂ surface with lithium bistrifluoromethanesulfonimide (Li-TFSI), which was recently shown to improve the device performance by facilitating the interfacial electron injection.²² The different device architectures are illustrated in **Figure 75** a–c, where rGO has been included in the m-TiO₂ layer, mixed perovskite layer, and spiro-OMeTAD layer, respectively. Energy level diagrams are inserted in the cartoon in **Figure 75** d–f.^{109, 141}

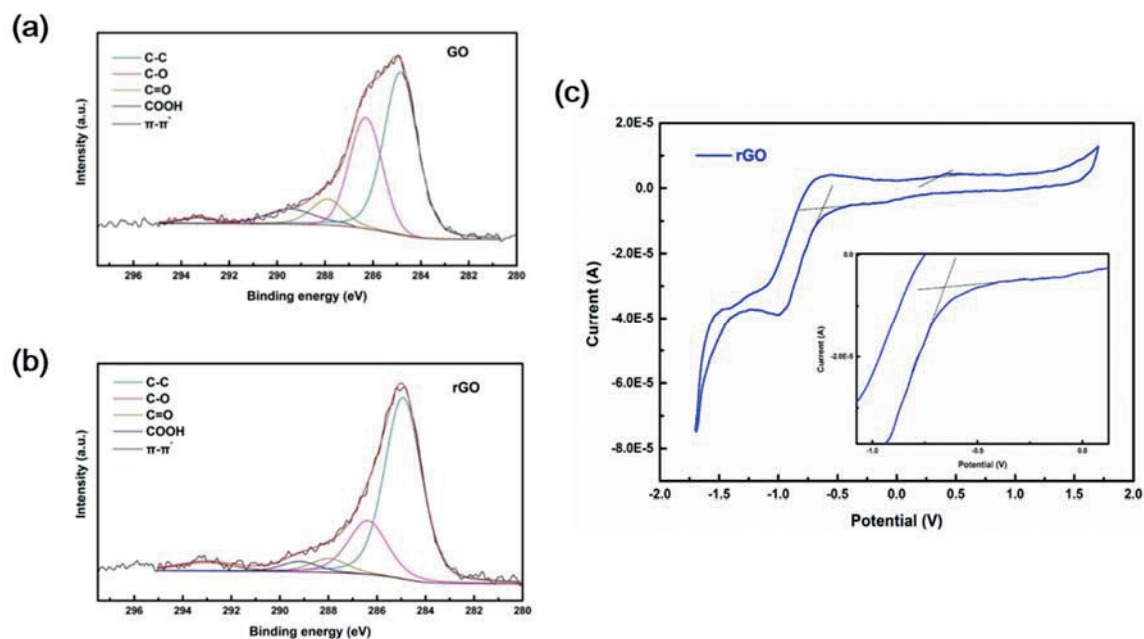


Figure 76 High-resolution XPS C1s spectra for (a) GO and (b) rGO. (c) Cyclic voltammetry curve of rGO, in CH₃CN using 0.1 M Tetrabutylammonium hexafluorophosphate (TBAPF₆) as the electrolyte, at a scan rate of 10 mVs⁻¹. Inset demonstrates the reduction peak onset of rGO.

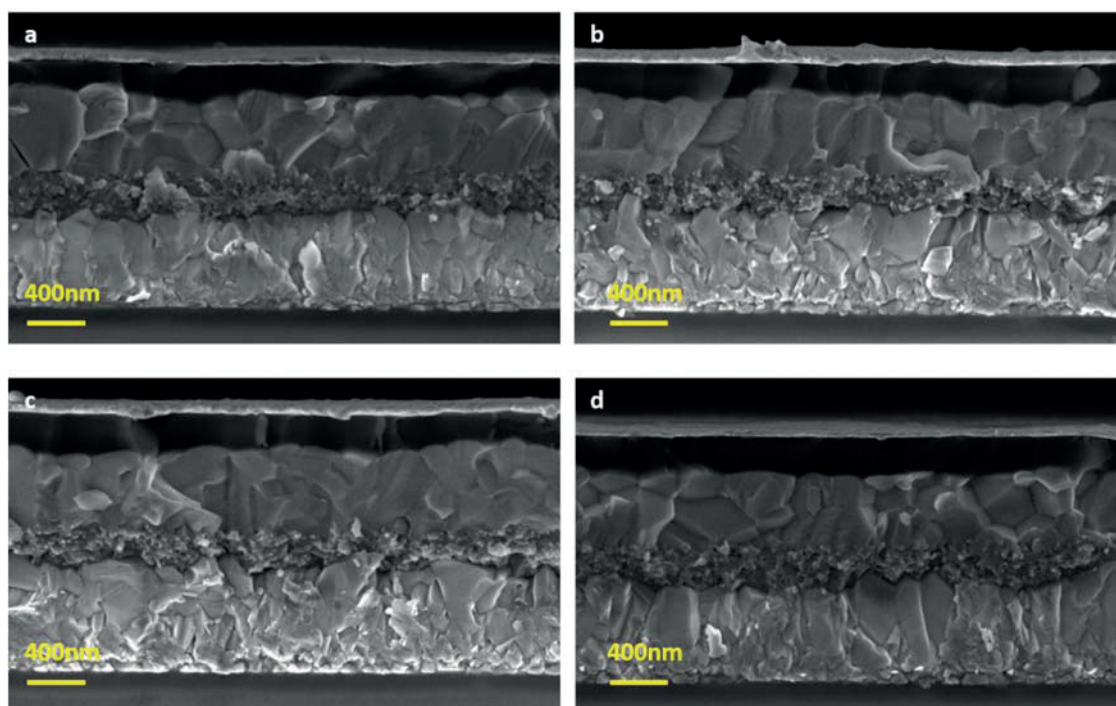


Figure 77. Cross-sectional field emission scanning electron microscopy (FESEM) of a) mpTiO₂, b) rGO/mp-TiO₂, c) rGO/(FAPbI₃)_{0.85}(MAPbBr₃)_{0.15}, d) rGO/spiro-OMeTAD based perovskite solar cell.

8.3.1. Preparation and characterization of rGO

The characterization of rGO, along with the calculations of the rGO HOMO/LUMO levels, being approximately $-4.96/-3.95$ eV, respectively, are explained in **Figures 76**. As the energy level of rGO is lower than the TiO_2 and mixed perovskite, we expect that a photoexcited electron can be extracted through the rGO plates. The cross-sectional scanning electron microscopy (SEM) images of the four studied PSC architectures are provided in **Figure 77**, showing the similar layered device structure. The current density–voltage (J – V) characteristics of the best devices for each architecture along with the device parameters are shown in **Figure 78**, respectively. Initially, these devices were fabricated with Li-treated TiO_2 layers. Depending on the rGO mixing layer, the performances vary dramatically. It is found that the presence of rGO in the m- TiO_2 layer has a strong positive impact on the device performances. Relative to the control cell (without rGO), which provides a PCE of 18.8 % (see Table in **Figure 78**), incorporation of rGO in the m- TiO_2 layer yields improved device performance with a PCE of 19.5 %.

8.3.2. Fabrication of PSCs with rGO/ and without Li treatment.

When the rGO is mixed in the spiro-OMeTAD or perovskite layers (**Figure 75b** and **c**), we observed no significant improvement in the device performance, and similar or lower PCEs were obtained (**Figure 78**). Interestingly, these results are in contrast to what was observed in the literature, where it is indicated that rGO always plays a positive role for improving the PCE of PSCs.^{154-156, 164, 165} The reduced photovoltaic performance when rGO is mixed either with the perovskite or with the spiro-

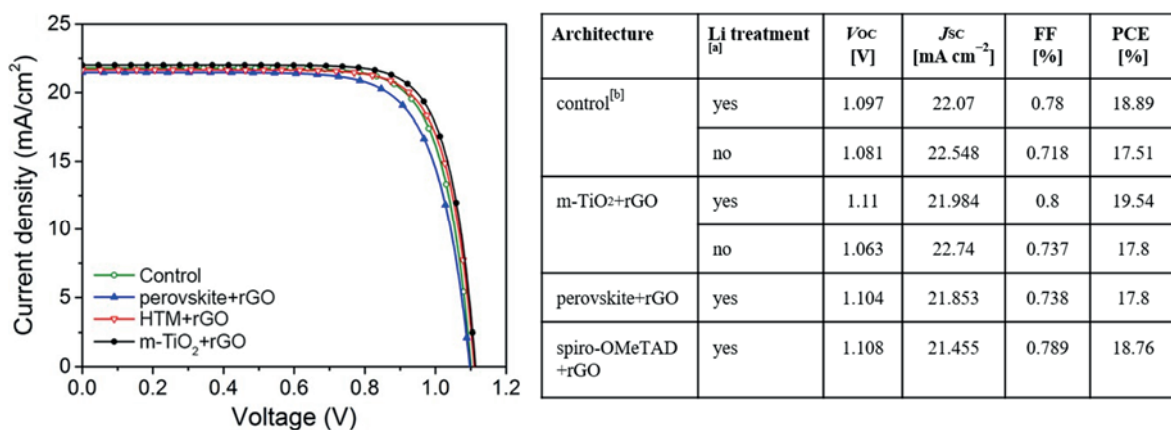


Figure 78. J – V curves of the best performing devices for each architecture described in Figure 74, measured under AM 1.5 G solar irradiation of 100 mW cm^{-2} . The solar cell parameters are summarized in Table.

[a] Li treatment: m- TiO_2 layer is treated with a solution of lithium bistrifluoromethanesulfonimide (Li-TFSI) in acetonitrile before deposition of the perovskite layer. [b] No rGO in the cell architecture.

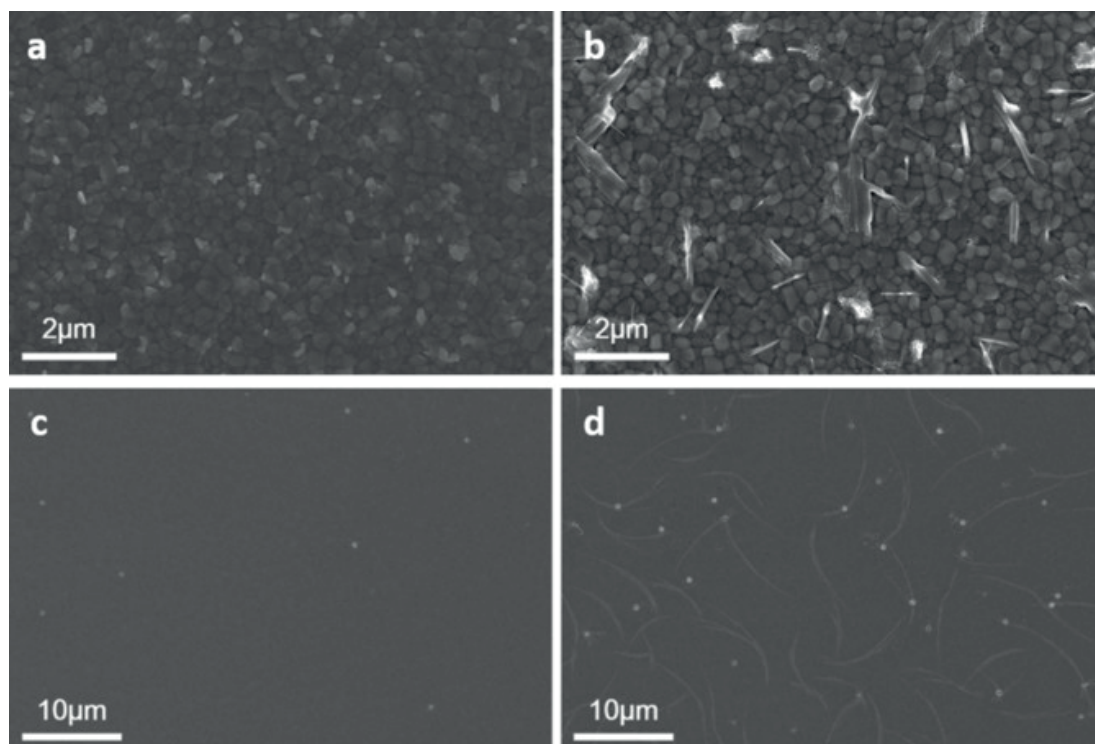


Figure 79. SEM top view of the layers (a, c) without and (b, d) with rGO: (a–b) perovskite and (c–d) spiro-OMeTAD. (b, d) Note the presence of aggregates on the surface in the samples with rGO, which can create shunt pathways between m-TiO₂, perovskite/spiro-OMeTAD, and gold.

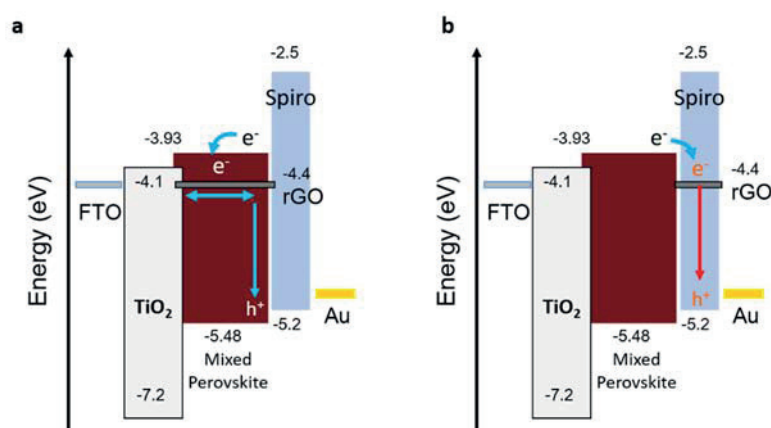


Figure 80. The schematic image for energy level alignment of the materials used in our devices and the assumed recombination mechanism in the a) perovskite and b) spiro HTM layer.

OMeTAD layers can be attributed to a detrimental effect of the rGO in the device structure. This observation comes from the analysis of SEM top-view (**Figure 79**). In **Figure 79a** and **c** the top-surface of the neat perovskite and spiro-OMeTAD layers are compared to the ones that include rGO (**Figure 79b** and **d**, respectively). When rGO is incorporated either within the perovskite or spiro-OMeTAD layer, the film is no longer homogeneous; incorporation of rGO is responsible for the formation of nanoflakes that disrupt the crystal quality. This leads to additional shunt pathways that

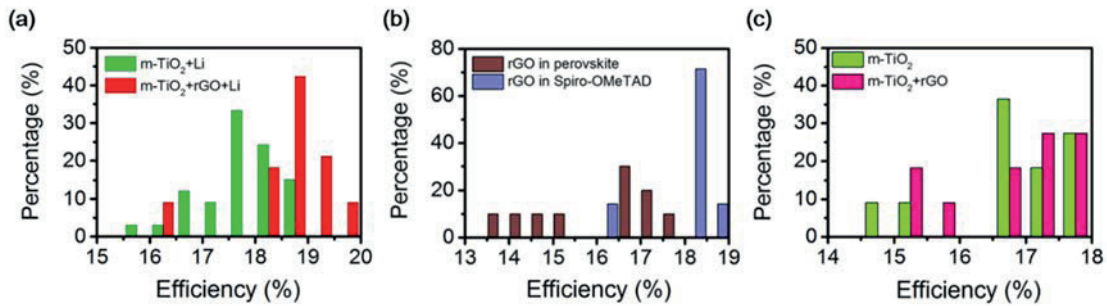


Figure 81. Statistics of the efficiency distribution for devices (a) with m-TiO₂ and m-TiO₂ including rGO (each 30 samples), (b) including rGO in perovskite and spiro-OMeTAD (16 samples), and (c) with un-doped m-TiO₂ layer (20 samples).

negatively affect the perovskite device performances. Direct pathways between the perovskite and the top Au electrode or the bottom TiO₂ and spiro-OMeTAD can be easily generated by the rGO flakes, increasing the possibility of charge recombination and leading to the reduced device performances observed. Note that this effect is amplified when the rGO is mixed within the perovskite, creating unwanted electron-leakage flow toward spiro-OMeTAD (**Figure 80**). On the contrary, when we added the rGO in the m-TiO₂ layer, the highest PCEs were obtained. Both the open-circuit voltage (V_{OC}) and fill factor (FF) were improved, resulting in the best performing device with PCE maximum of 19.54 %. We conclude that the addition of rGO only has a beneficial effect on the PSC performance when mixed with the m-TiO₂ layer. The statistics of the efficiency distribution shown in **Figure 81a** and **b** demonstrate the repeatability of the enhancement achieved by employing rGO in the m-TiO₂ layer.

8.3.2. Fabrication of PSCs with rGO/ and with Li treatment.

To further unveil the effects of the rGO incorporation in the m-TiO₂ layer, we also fabricated devices without the Li treatment on TiO₂ electrode. Li treatment is usually performed for the high-efficiency solar cells, because it has a beneficial role in passivating the surface traps and improving electron injection.^{22,166} We compare in **Figure 82a** the $J-V$ curves with and without Li-treated TiO₂ electrodes and/or rGO. Note that without the Li treatment the performances are overall reduced with PCE values of around 17 %, as shown in Table in Figure 77. The efficiency statistics of these devices is also depicted in **Figure 81 c**.

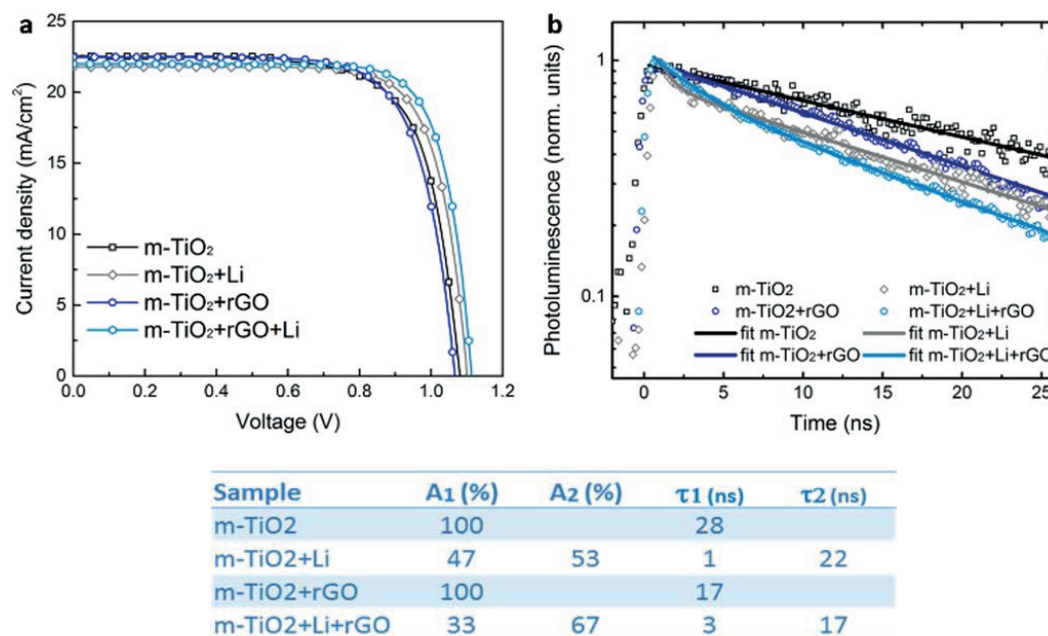


Figure 82. (a) J - V characteristics of the solar cells whose parameters are presented in Table of Figure 77. (b) Normalized PL decay measured at 770 nm upon excitation at 460 nm from the m-TiO₂ side for samples with and without rGO and/or Li doping in the HTM, as indicated in the legend. Solid lines represent the outcome of the exponential fitting. See below Table for fitting parameters. All the samples have been encapsulated to prevent oxygen or moisture degradation.

We note that the difference from insertion of rGO in the un-treated m-TiO₂ electrode is lower compared with the Li-treated m-TiO₂+rGO devices. Although the device using untreated m-TiO₂+rGO shows an increased FF and short-circuit current density (J_{sc}), suggesting an improved electron-injection pathway, the V_{oc} is reduced. From our results, it is clear that devices incorporating Li-treated m-TiO₂+rGO yield the best performance.

The role of the rGO was further studied by monitoring the photoluminescence (PL) decays of the devices with Li-treated m-TiO₂+rGO. The presence of rGO induces a quenching of the PL signal (see Figure 83a). Figure 82b shows the PL dynamics at 770 nm upon excitation at 460 nm. The control sample, containing untreated m-TiO₂ without rGO, shows a long-living decay out of our temporal window reflecting the intrinsic electron-hole recombination dynamic in the perovskite.¹⁶⁷ On the contrary, we observed that the presence of the rGO quenches the PL signal. This might indicate that, among other processes, electron transfer is facilitated in the presence of the rGO. The quenching happens on a time scale of a few tens of ns. Table in Figure 82 shows the parameters derived from exponential fitting of the PL decays. On the other side, when both rGO and Li-TFSI were mixed with the m-TiO₂, an even faster quenching component was observed, resulting in an initial PL decay within 1 ns, which corresponds to the resolution of our system. This can be attributed

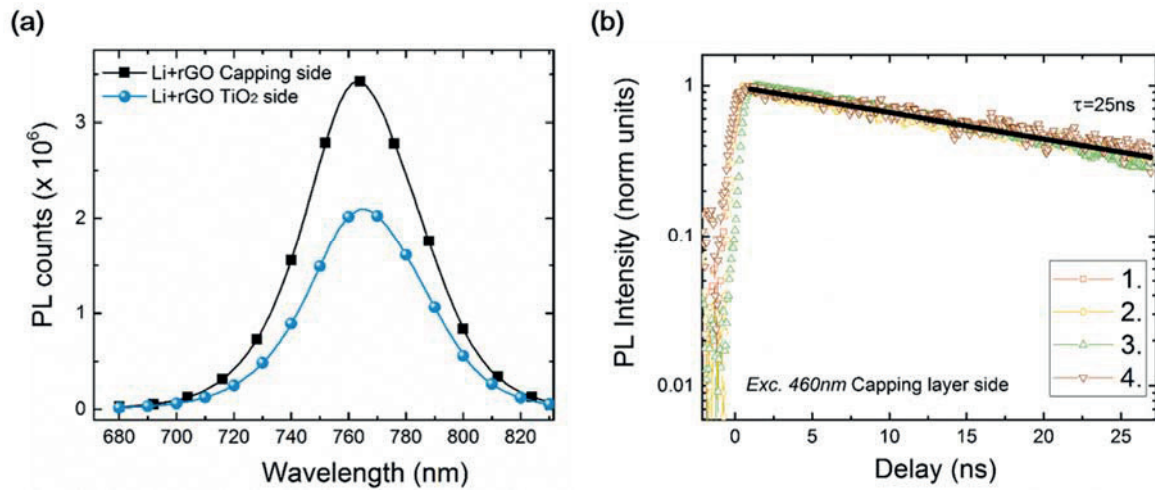


Figure 83. (a) PL spectra of the m-TiO₂ based sample treated with Li and with rGO in the TiO₂ matrix. To quantify the PL quenching due to electron transfer we measured the same sample upon excitation from the capping layer or from the TiO₂ layer. A quenching of about 45% is found. (b) PL decay upon excitation from the capping side at 460 nm. Sample 1. Perovskite/m-TiO₂; 2. Perovskite/m-TiO₂+Li; 3. Perovskite/rGO+m-TiO₂; 4. Perovskite/rGO+m-TiO₂+Li. Excitation density of ~ 10 nJ/cm². All the samples have been encapsulated to prevent degradation or any oxygen/moisture induced effects. The PL shows a monoexponential decay with a time constant beyond our temporal window. No difference is observed among the samples investigated, because we are mainly probing the properties of the capping layer side that are similar in all the cases.

to more efficient and faster electron injection at the treated interface owing to the synergic positive effects of improving the electron extraction. For the sake of completeness, note that no differences were observed when we probed the PL decay upon exciting selectively the perovskite capping layer (Figure 83b), supporting the role of rGO exclusively on the interfacial dynamics.

8.4. Conclusion.

The overall study presents a thorough analysis of the role of rGO integrated into PSCs, elucidating its main role in improving electron transport when mixed with the m-TiO₂ layer. In the other case, unwanted shunt resistance pathways are generated if the rGO is incorporated with the perovskite or spiro-OMeTAD layers, reducing the overall device performance. In addition, from the synergic effect of the rGO and Li treatment in the m-TiO₂ layer, the device yielded a superior PCE of 19.54 %, which is ascribed to the beneficial role of rGO in extracting electrons through the ETM. We believe that our combined system of rGO and Li treatment may pave the way for further developing and optimizing the electron transport and collection behind high efficient PSCs.

8.5. Experimental Section

8.4.1. Preparation of graphene oxide

Graphene oxide was prepared from graphite powder (Alfa Aesar, ~200 mesh) according to a modified Hummers' method. In more detail, graphite powder (0.5 g) was placed into a mixture of sulfuric acid (40 mL, 98 %) and sodium nitrate (0.375 g). The mixture was then stirred and cooled in an ice bath. While maintaining vigorous stirring, potassium permanganate (3.0 g) was added in portions over a period of 2 h. The reaction mixture was left for 4 h to reach room temperature before being heated at 35 °C for 30 min. It was then poured into a flask containing deionized water (50 mL) and further heated at 70 °C for 15 min. The mixture was then decanted into 250 mL of deionized water and the unreacted KMnO_4 was removed by adding 3 % hydrogen peroxide. The reaction mixture was then allowed to settle and decanted. The obtained graphite oxide was purified by repeated centrifugation and redispersed in deionized water until a neutralized pH was achieved. Finally, the resulting graphene oxide was dried at 60 °C in a vacuum oven for 48 h before use.

8.4.2. Preparation of rGO

The reduction of graphene oxide was performed using a mixture of hydriodic acid (55 %)/acetic acid. In detail, the as-prepared graphene oxide powder (0.1 g) was sonicated in acetic acid (37 mL) for 2 h. Hydroiodic acid (2 mL) was then added and the mixture was stirred at 40 °C for 40 h. After being isolated by filtration, the product was washed through a three-step procedure using saturated sodium bicarbonate (3×2.5 mL), distilled water (3×2.5 mL), and acetone (2×2.5 mL). Finally, the resulting rGO was dried at 60 °C in a vacuum oven overnight.

8.4.3. Device fabrication

FTO (NSG 10)-coated glass was used as a substrate and was cleaned in 2 % Hellmanex water solution by sonication, and then rinsed, first in water and finally in ethanol and acetone. A hole-blocking layer of compact TiO_2 was deposited on the cleaned FTO by using spray pyrolysis at 450 °C. The precursor spray solution was prepared by diluting titanium diisopropoxide (30 % in isopropanol, Sigma–Aldrich) in ethanol by the proportions 5:95 by volume. Oxygen was used as a carrier gas.

After spraying, the FTO was cooled to room temperature. On top of the compact TiO₂ layer, a m-TiO₂ layer was fabricated by first spin-coating TiO₂ nanoparticles at 2000 rpm for 10 s. TiO₂ paste (Dyesol 30 NR-D) was diluted in ethanol at a concentration of 125 mg mL⁻¹ and used for mesoporous layer. Then substrates were sintered at on a hot plate for 30 min and then slowly cooled down. For Li treatment on the TiO₂ layer, the substrates were re-heated to 450 °C and maintained at this temperature for 30 min after spin coating a 0.1 m lithium bistrifluoromethanesulfonimide (Li-TFSI, Sigma–Aldrich) in acetonitrile (Acros) at 3000 rpm for 10 s. After cooling, they were transferred directly into a nitrogen glovebox. A perovskite precursor solution was spin-coated in the glove box. The (FAPbI₃)_{0.85}(MAPbBr₃)_{0.15} precursor solution was composed of FAI (1 m), PbI₂ (1.1 m, Sigma–Aldrich), MABr (0.2 m), and PbBr₂ (0.2 m, Sigma–Aldrich) in anhydrous DMF/DMSO (Acros)=4:1 v/v. This composition contains a lead excess as reported previously. The solution was spin-coated at 1000 rpm for 10 s and continuously at 6000 rpm for 30 s. During the second step, when approximately 15 s left before finish, 100 µL of anhydrous chlorobenzene was added. After spin-coating, the films were annealed on a hotplate at 100 °C for 90 min. If the perovskite films were cooled to ambient temperature, a 70 nm solution of spiro-OMeTAD (Merck) dissolved in chlorobenzene (Acros) was spin-coated on top of the films at 4000 rpm for 20 s. Three different additives were added to the spiro-OMeTAD solution: 4-*tert*-butylpyridine (TBP), Li-TFSI in acetonitrile, and FK209 (Dyesol) in acetonitrile. The molar ratio of spiro-OMeTAD/FK209/Li-TFSI/TBP was 1:0.03:0.5:3.3. Lastly, the 70 nm thick Au counter electrode was deposited by thermal evaporation.

In this experiment, a specified concentration of rGO added to the spiro-OMeTAD or perovskite solutions was limited to 0.055 mg mL⁻¹ and 0.01 µg mL⁻¹, respectively, because rGO has limited solubility in each solvent. In a mixed solvent of DMF/DMSO (perovskite solution) and chlorobenzene (spiro-OMeTAD solution), these concentrations showed no precipitate after sonication for 2 h. In the case of TiO₂, we chose the concentration when a maximum efficiency was obtained from an incorporation of rGO in the m-TiO₂ layer.

8.4.4. Solar cell characterization

The solar cells were characterized using a 450 W xenon light source (Oriel) equipped with a Keithley 2400 source meter. The light intensity was measured by a certified reference Si cell equipped with an IR-cutoff filter, KG5 (Newport), and it was adjusted to 1000 W m⁻² during each measurement. A black metal mask of 0.16 cm² was used to fix the active area of the solar cells and a scan rate is 2.5

mV s^{-1} on forward and backward scans. A ZEISS Merlin high-resolution scanning electron microscope (HR-SEM) was performed for the morphology of the device cross-section and surface of films. X-ray powder diffraction (XRD) was recorded on a D8 advance (Bruker) equipped with a ceramic tube (Cu anode, $\lambda=1.54060 \text{ \AA}$) in an angle range of $2\theta=10\text{--}70^\circ$.

8.4.5. PL experiment

Steady state PL spectra were recorded using a spectrophotometer (Gilden Photonics) equipped with a cw Xenon lamp utilized for excitation. To detect the time-resolved PL trace, a pulsed source at 460 nm (Ps diode lasers BDS-SM, pulse with $<100 \text{ ps}$, from Photonic Solutions, approx. 1 mW power, 20 MHz repetition rate, approx. 500 μm spot radius) was used as excitation and the signal is recorded at 770 nm by the time-correlated single-photon counting detection technique with a time resolution of 1 ns. Excitation density of $\sim 10 \text{ nJ cm}^{-2}$. All the samples have been encapsulated to prevent degradation or any oxygen/moisture-induced effects. A monoexponential and bi-exponential fitting are used to analyze the background-corrected PL decay signal.

Chapter 9. Conclusion

Conclusion and future perspective.

In this thesis, my favorite research is the passivating perovskite layer and used it as a tool to increase V_{OC} in perovskite solar cells. (Chapter 3&4) However, before applying my ideas we need to fabricate proper working perovskite solar cells. It was consumed almost one year to optimize various conditions and surrounding environment after moving in new laboratory. And then, it was successfully obtained the optimized perovskite solar cells having comparable efficiency to other top groups. We employed mixed cations and halide perovskite for precursors of perovskite films and solvent engineering technique for fabricating devices. (Chapter 2) This optimized devices became the basement, from which we implemented various concepts and modification.

In Chapter 3 and 4, specifically, the passivation to perovskite layer is a main concept to enhance the performance. I obtained this idea from typical Si solar cells and one of engineering technique, back surface field. In Si solar cells, an introduction of additional layer between emitter and electrode has been used to prevent or reduce charge carrier recombination. The interface recombination at a position where two different materials contact accounts for degrading V_{OC} in the efficiency of devices. Thus, the inserting of similar precursor material but having wider bandgap at this position showed the improved PCE by increasing V_{OC} .

First, we utilized a FABr precursor to generate a new perovskite layer at the end of pristine $(FAPbI_3)_{0.85}(MAPbBr_3)_{0.15}$ perovskite layer, contacting a HTL (spiro-OMeTAD). We performed a post treatment by spincoating FABr precursor solution on the pre-formed perovskite film. Although we didn't figure out the distinct perovskite $(FAPbI_{3-x}Br_x)$, it is found that the efficiency by this engineered perovskite might be improved by the effect of passivating defects.

By upgrading this concept of FABr passivation, we focused on the development of 2D perovskite layer between the triple cation mixed perovskite $Cs_{0.1}FA_{0.74}MA_{0.13}PbI_{2.48}Br_{0.39}$ and spiro-OMeTAD. We followed the same skill of post spincoating precursor solution, here, of PEAI. We discovered a new low dimensional perovskite (eg. PEA_2PbI_4) was formed distinctly on top of $Cs_{0.1}FA_{0.74}MA_{0.13}PbI_{2.48}Br_{0.39}$ perovskite film and demonstrated the broad applicability of this post treatment engineering concept. In addition, this depositing 2D perovskite layer leads improvement on stability of devices, as well as the efficiency with the increase of V_{OC} and J_{SC} . The relatively strong low dimensional perovskite layer reduces the degradation of perovskite layer

I also investigated other application fields and tested the potential of lead free perovskite in solar cells. (Chapter 5) All of established perovskite kinds exhibiting high efficient performance on photovoltaics include the Pb in their composition. Although it is insisted that the amount included in final complete devices is quite low, it is still very dangerous and toxic for human because the perovskites used in PV researches are very soluble in water. As considering this fact, we have to move to lead free perovskite on the future. For lead free perovskite, we employed a double perovskite $\text{Cs}_2\text{AgBiBr}_6$ to overcome the toxicity and instability. However, the double perovskite has too wide bandgap for obtaining high efficient solar cells. We demonstrated the possibility that this lead free perovskite can work in photovoltaics. Further studies are needed for reducing the large bandgap with sustaining extraordinary photovoltaic properties of lead perovskites.

In Chapter 6 and 7, we took the challenge of testing the various hole transporting materials coming out from perovskite materials. Zinc phthalocyanines were used replacing spiro-OMeTAD and showed the outstanding 17.5% for tetra-5-hexylthiophene-based analogue. Worthy to highlight, widely used spiro-OMeTAD and PTAA are too expensive to become commercialization and weak to sustain under the harsh ambient environment. We expected the ZnPc-based HTM layer might be concluded as stable and economic hole-transport materials, opening new frontiers toward a realistic, efficient, and inexpensive energy production. Finally, we have also a trial of modification on ETL with graphene. Graphene is known well because of its outstanding electric conductivity. When inserting in perovskite layer and HTL, it is shown lower efficiencies because the large size of graphene flakes prevented perovskite from crystallization and make additional routes for multiplying charge carrier recombination in perovskite layer and HTL. Only in ETL we can take its advantage of high electric conductivity.

Consequently, I studied and touched all of parts in configuration of perovskite solar cells, ETL, perovskite, and HTMs. Although I did not synthesize and design the HTMs by myself, I think I helped well to figure out which HTMs are working without troubles about transporting charges and why the degraded performance was shown. Specially, in the aspect of perovskite film, I believe my thesis paves the way toward improving perovskite solar cells on efficiency and stability by passivating techniques, thus overcoming important limitations for commercialization. The success of these methods would need further research and improvement on various perovskite composition and configuration, as well as on other perovskite devices. With more optimization and tests, the future when we do not have any energy problems by perovskite solar cells will come soon.

Reference.

1. R. M. Hazen, L. W. Finger, R. J. Angel, C. T. Prewitt, N. L. Ross, H. K. Mao, C. G. Hadidiacos, P. H. Hor, R. L. Meng and C. W. Chu, *Physical Review B*, 1987, **35**, 7238-7241.
2. N. R. E. L. (NREL), *Research Cell Efficiency Records*.
3. M. V. Kovalenko, L. Protesescu and M. I. Bodnarchuk, *Science*, 2017, **358**, 745-750.
4. J. Hwang, R. R. Rao, L. Giordano, Y. Katayama, Y. Yu and Y. Shao-Horn, *Science*, 2017, **358**, 751-756.
5. V. M. Goldschmidt, *Naturwissenschaften*, 1926, **14**, 477-485.
6. H. Kronmüller and S. Parkin, *Handbook of magnetism and advanced magnetic materials: Spintronics and magnetoelectronics*, John Wiley & Sons, 2007.
7. D. A. Neamen, *Semiconductor Physics and Devices (SIE)*, McGraw-Hill Higher Education, 2012.
8. A. Polman, M. Knight, E. C. Garnett, B. Ehrler and W. C. Sinke, *Science*, 2016, **352**.
9. J.-P. Correa-Baena, M. Saliba, T. Buonassisi, M. Grätzel, A. Abate, W. Tress and A. Hagfeldt, *Science*, 2017, **358**, 739-744.
10. Q. Dong, Y. Fang, Y. Shao, P. Mulligan, J. Qiu, L. Cao and J. Huang, *Science*, 2015, **347**, 967-970.
11. W. S. Yang, B.-W. Park, E. H. Jung, N. J. Jeon, Y. C. Kim, D. U. Lee, S. S. Shin, J. Seo, E. K. Kim, J. H. Noh and S. I. Seok, *Science*, 2017, **356**, 1376-1379.
12. M. I. Saidaminov, A. L. Abdelhady, B. Murali, E. Alarousu, V. M. Burlakov, W. Peng, I. Dursun, L. Wang, Y. He, G. Maculan, A. Goriely, T. Wu, O. F. Mohammed and O. M. Bakr, *Nat Commun*, 2015, **6**, 7586.
13. Q. Han, S.-H. Bae, P. Sun, Y.-T. Hsieh, Y. Yang, Y. S. Rim, H. Zhao, Q. Chen, W. Shi, G. Li and Y. Yang, *Advanced Materials*, 2016, **28**, 2253-2258.
14. J. Seo, J. H. Noh and S. I. Seok, *Accounts of Chemical Research*, 2016, **49**, 562-572.
15. D. P. McMeekin, G. Sadoughi, W. Rehman, G. E. Eperon, M. Saliba, M. T. Hörantner, A. Haghighirad, N. Sakai, L. Korte, B. Rech, M. B. Johnston, L. M. Herz and H. J. Snaith, *Science*, 2016, **351**, 151-155.
16. G. E. Eperon, S. D. Stranks, C. Menelaou, M. B. Johnston, L. M. Herz and H. J. Snaith, *Energy & Environmental Science*, 2014, **7**, 982-988.
17. H. J. Snaith, *The Journal of Physical Chemistry Letters*, 2013, **4**, 3623-3630.
18. P. Saint-Cast, J. Benick, D. Kania, L. Weiss, M. Hofmann, J. Rentsch, R. Preu and S. W. Glunz, *IEEE Electron Device Letters*, 2010, **31**, 695-697.
19. S. K. Hau, H.-L. Yip, O. Acton, N. S. Baek, H. Ma and A. K. Y. Jen, *Journal of Materials Chemistry*, 2008, **18**, 5113-5119.

20. L. Cattin, F. Dahou, Y. Lare, M. Morsli, R. Tricot, S. Houari, A. Mokrani, K. Jondo, A. Khelil, K. Napo and J. C. Bernède, *Journal of Applied Physics*, 2009, **105**, 034507.
21. Y. H. Lee, J. Luo, M.-K. Son, P. Gao, K. T. Cho, J. Seo, S. M. Zakeeruddin, M. Grätzel and M. K. Nazeeruddin, *Advanced Materials*, 2016, **28**, 3966-3972.
22. F. Giordano, A. Abate, J. P. Correa Baena, M. Saliba, T. Matsui, S. H. Im, S. M. Zakeeruddin, M. K. Nazeeruddin, A. Hagfeldt and M. Graetzel, *Nat Commun*, 2016, **7**, 10379.
23. Y. Shao, Z. Xiao, C. Bi, Y. Yuan and J. Huang, *Nat Commun*, 2014, **5**.
24. J. H. Heo, S. H. Im, J. H. Noh, T. N. Mandal, C.-S. Lim, J. A. Chang, Y. H. Lee, H.-j. Kim, A. Sarkar, K. NazeeruddinMd, M. Gratzel and S. I. Seok, *Nat Photon*, 2013, **7**, 486-491.
25. E. Edri, S. Kirmayer, S. Mukhopadhyay, K. Gartsman, G. Hodes and D. Cahen, *Nat Commun*, 2014, **5**.
26. C. Roldan-Carmona, P. Gratia, I. Zimmermann, G. Grancini, P. Gao, M. Graetzel and M. K. Nazeeruddin, *Energy & Environmental Science*, 2015, **8**, 3550-3556.
27. O. von Roos, *Journal of Applied Physics*, 1978, **49**, 3503-3511.
28. K. Masuko, M. Shigematsu, T. Hashiguchi, D. Fujishima, M. Kai, N. Yoshimura, T. Yamaguchi, Y. Ichihashi, T. Mishima, N. Matsubara, T. Yamanishi, T. Takahama, M. Taguchi, E. Maruyama and S. Okamoto, *IEEE Journal of Photovoltaics*, 2014, **4**, 1433-1435.
29. I. J. Kramer, L. Levina, R. Debnath, D. Zhitomirsky and E. H. Sargent, *Nano Letters*, 2011, **11**, 3701-3706.
30. J. Y. Kim, V. Adinolfi, B. R. Sutherland, O. Voznyy, S. J. Kwon, T. W. Kim, J. Kim, H. Ihee, K. Kemp, M. Adachi, M. Yuan, I. Kramer, D. Zhitomirsky, S. Hoogland and E. H. Sargent, *Nat Commun*, 2015, **6**.
31. N. J. Jeon, J. H. Noh, W. S. Yang, Y. C. Kim, S. Ryu, J. Seo and S. I. Seok, *Nature*, 2015, **517**, 476-480.
32. Y. C. Kim, N. J. Jeon, J. H. Noh, W. S. Yang, J. Seo, J. S. Yun, A. Ho-Baillie, S. Huang, M. A. Green, J. Seidel, T. K. Ahn and S. I. Seok, *Advanced Energy Materials*, 2015, **6**.
33. A. A. Zhumekenov, M. I. Saidaminov, M. A. Haque, E. Alarousu, S. P. Sarmah, B. Murali, I. Dursun, X.-H. Miao, A. L. Abdelhady, T. Wu, O. F. Mohammed and O. M. Bakr, *ACS Energy Letters*, 2016, DOI: 10.1021/acsenergylett.6b00002, 32-37.
34. S. Ryu, J. H. Noh, N. J. Jeon, Y. Chan Kim, W. S. Yang, J. Seo and S. I. Seok, *Energy & Environmental Science*, 2014, **7**, 2614-2618.
35. Y. H. Lee, S. H. Im, J. A. Chang, J.-H. Lee and S. I. Seok, *Organic Electronics*, 2012, **13**, 975-979.

36. Q. Chen, H. Zhou, T.-B. Song, S. Luo, Z. Hong, H.-S. Duan, L. Dou, Y. Liu and Y. Yang, *Nano Letters*, 2014, **14**, 4158-4163.
37. T. Supasai, N. Rujisamphan, K. Ullrich, A. Chemseddine and T. Dittrich, *Appl Phys Lett*, 2013, **103**, 183906.
38. C. C. Stoumpos, C. D. Malliakas and M. G. Kanatzidis, *Inorganic Chemistry*, 2013, **52**, 9019-9038.
39. T. M. Koh, K. Fu, Y. Fang, S. Chen, T. C. Sum, N. Mathews, S. G. Mhaisalkar, P. P. Boix and T. Baikie, *The Journal of Physical Chemistry C*, 2014, **118**, 16458-16462.
40. A. Binek, F. C. Hanusch, P. Docampo and T. Bein, *The Journal of Physical Chemistry Letters*, 2015, **6**, 1249-1253.
41. Z. Li, M. Yang, J.-S. Park, S.-H. Wei, J. J. Berry and K. Zhu, *Chemistry of Materials*, 2016, **28**, 284-292.
42. R. López and R. Gómez, *Journal of Sol-Gel Science and Technology*, 2012, **61**, 1-7.
43. D. Bi, W. Tress, M. I. Dar, P. Gao, J. Luo, C. Renevier, K. Schenk, A. Abate, F. Giordano, J. P. Correa Baena, J. D. Decoppet, S. M. Zakeeruddin, M. K. Nazeeruddin, M. Grätzel and A. Hagfeldt, *Sci Adv*, 2016, **2**, e1501170.
44. B. Obama, *Science*, 2017, **355**, 126-129.
45. N.-G. Park, M. Grätzel, T. Miyasaka, K. Zhu and K. Emery, *Nature Energy*, 2016, **1**, 16152.
46. B. Conings, J. Drijkoningen, N. Gauquelin, A. Babayigit, J. D'Haen, L. D'Olieslaeger, A. Ethirajan, J. Verbeeck, J. Manca, E. Mosconi, F. D. Angelis and H.-G. Boyen, *Advanced Energy Materials*, 2015, **5**, 1500477.
47. W. Nie, J. C. Blancon, A. J. Neukirch, K. Appavoo, H. Tsai, M. Chhowalla, M. A. Alam, M. Y. Sfeir, C. Katan, J. Even, S. Tretiak, J. J. Crochet, G. Gupta and A. D. Mohite, *Nat Commun*, 2016, **7**, 11574.
48. Y. Han, S. Meyer, Y. Dkhissi, K. Weber, J. M. Pringle, U. Bach, L. Spiccia and Y.-B. Cheng, *Journal of Materials Chemistry A*, 2015, **3**, 8139-8147.
49. X. Li, D. Bi, C. Yi, J.-D. Décoppet, J. Luo, S. M. Zakeeruddin, A. Hagfeldt and M. Grätzel, *Science*, 2016, **353**, 58-62.
50. Z. Wang, D. P. McMeekin, N. Sakai, S. van Reenen, K. Wojciechowski, J. B. Patel, M. B. Johnston and H. J. Snaith, *Advanced Materials*, 2016, **29**, 164186.
51. J. W. Lee, D. H. Kim, H. S. Kim, S. W. Seo, S. M. Cho and N. G. Park, *Advanced Energy Materials*, 2015, **5**.
52. M. Saliba, T. Matsui, K. Domanski, J.-Y. Seo, A. Ummadisingu, S. M. Zakeeruddin, J.-P. Correa-Baena, W. R. Tress, A. Abate, A. Hagfeldt and M. Grätzel, *Science*, 2016, **354**, 206-209.
53. I. C. Smith, E. T. Hoke, D. Solis-Ibarra, M. D. McGehee and H. I. Karunadasa, *Angewandte Chemie International Edition*, 2014, **53**, 11232-11235.
54. D. H. Cao, C. C. Stoumpos, O. K.

- Farha, J. T. Hupp and M. G. Kanatzidis, *Journal of the American Chemical Society*, 2015, **137**, 7843-7850.
55. H. Tsai, W. Nie, J. C. Blancon, C. C. Stoumpos, R. Asadpour, B. Harutyunyan, A. J. Neukirch, R. Verduzco, J. J. Crochet, S. Tretiak, L. Pedesseau, J. Even, M. A. Alam, G. Gupta, J. Lou, P. M. Ajayan, M. J. Bedzyk and M. G. Kanatzidis, *Nature*, 2016, **536**, 312-316.
56. S. S. Shin, E. J. Yeom, W. S. Yang, S. Hur, M. G. Kim, J. Im, J. Seo, J. H. Noh and S. I. Seok, *Science*, 2017, **356**, 167-171.
57. H. Tan, A. Jain, O. Voznyy, X. Lan, F. P. García de Arquer, J. Z. Fan, R. Quintero-Bermudez, M. Yuan, B. Zhang, Y. Zhao, F. Fan, P. Li, L. N. Quan, Y. Zhao, Z.-H. Lu, Z. Yang, S. Hoogland and E. H. Sargent, *Science*, 2017, **355**, 722-726.
58. G. Grancini, C. Roldán-Carmona, I. Zimmermann, E. Mosconi, X. Lee, D. Martineau, S. Narbey, F. Oswald, F. De Angelis, M. Graetzel and M. K. Nazeeruddin, *Nat Commun*, 2017, **8**, 15684.
59. D. Bi, P. Gao, R. Scopelliti, E. Oveisi, J. Luo, M. Grätzel, A. Hagfeldt and M. K. Nazeeruddin, *Advanced Materials*, 2016, **28**, 2910-2915.
60. X. Gan, O. Wang, K. Liu, X. Du, L. Guo and H. Liu, *Solar Energy Materials and Solar Cells*, 2017, **162**, 93-102.
61. Z. Wang, Q. Lin, F. P. Chmiel, N. Sakai, L. M. Herz and H. J. Snaith, *Nature Energy*, 2017, **2**, 17135.
62. L. N. Quan, M. Yuan, R. Comin, O. Voznyy, E. M. Bearegard, S. Hoogland, A. Buin, A. R. Kirmani, K. Zhao, A. Amassian, D. H. Kim and E. H. Sargent, *Journal of the American Chemical Society*, 2016, **138**, 2649-2655.
63. B.-E. Cohen, M. Wierzbowska and L. Etgar, *Advanced Functional Materials*, 2017, **27**, 1604733.
64. N. Li, Z. Zhu, C.-C. Chueh, H. Liu, B. Peng, A. Petrone, X. Li, L. Wang and A. K. Y. Jen, *Advanced Energy Materials*, 2016, **7**, 1601307.
65. M. Yuan, L. N. Quan, R. Comin, G. Walters, R. Sabatini, O. Voznyy, S. Hoogland, Y. Zhao, E. M. Bearegard, P. Kanjanaboos, Z. Lu, D. H. Kim and E. H. Sargent, *Nat Nanotechnol*, 2016, **11**, 872-877.
66. J. J. van Franeker, K. H. Hendriks, B. J. Bruijnaers, M. W. G. M. Verhoeven, M. M. Wienk and R. A. J. Janssen, *Advanced Energy Materials*, 2017, **7**, 1601822.
67. G. Grancini, S. Marras, M. Prato, C. Giannini, C. Quarti, F. De Angelis, M. De Bastiani, G. E. Eperon, H. J. Snaith, L. Manna and A. Petrozza, *The Journal of Physical Chemistry Letters*, 2014, **5**, 3836-3842.
68. K.-z. Du, Q. Tu, X. Zhang, Q. Han, J. Liu, S. Zauscher and D. B. Mitzi, *Inorganic Chemistry*, 2017, **56**, 9291-9302.
69. K. T. Cho, S. Paek, G. Grancini, C.

- Roldan-Carmona, P. Gao, Y. Lee and M. K. Nazeeruddin, *Energy & Environmental Science*, 2017, **10**, 621-627.
70. O. Almora, C. Aranda, E. Mas-Marzá and G. Garcia-Belmonte, *Appl Phys Lett*, 2016, **109**, 173903.
71. A. Guerrero, G. Garcia-Belmonte, I. Mora-Sero, J. Bisquert, Y. S. Kang, T. J. Jacobsson, J.-P. Correa-Baena and A. Hagfeldt, *The Journal of Physical Chemistry C*, 2016, **120**, 8023-8032.
72. M. Saba, M. Cadelano, D. Marongiu, F. Chen, V. Sarritzu, N. Sestu, C. Figus, M. Aresti, R. Piras, A. Geddo Lehmann, C. Cannas, A. Musinu, F. Quochi, A. Mura and G. Bongiovanni, 2014, **5**, 5049.
73. W. Chen, Y. Wu, Y. Yue, J. Liu, W. Zhang, X. Yang, H. Chen, E. Bi, I. Ashraful, M. Grätzel and L. Han, *Science*, 2015, **350**, 944-948.
74. Y. Lee, S. Paek, K. T. Cho, E. Oveisi, P. Gao, S. Lee, J. S. Park, Y. Zhang, R. Humphry-Baker, A. M. Asiri and M. K. Nazeeruddin, *Journal of Materials Chemistry A*, 2017, **5**, 12729-12734.
75. K. Domanski, J.-P. Correa-Baena, N. Mine, M. K. Nazeeruddin, A. Abate, M. Saliba, W. Tress, A. Hagfeldt and M. Grätzel, *ACS Nano*, 2016, **10**, 6306-6314.
76. T. A. Berhe, W.-N. Su, C.-H. Chen, C.-J. Pan, J.-H. Cheng, H.-M. Chen, M.-C. Tsai, L.-Y. Chen, A. A. Dubale and B.-J. Hwang, *Energy & Environmental Science*, 2016, **9**, 323-356.
77. G. E. Eperon, S. N. Habisreutinger, T. Leijtens, B. J. Bruijnaers, J. J. van Franeker, D. W. deQuilettes, S. Pathak, R. J. Sutton, G. Grancini, D. S. Ginger, R. A. J. Janssen, A. Petrozza and H. J. Snaith, *ACS Nano*, 2015, **9**, 9380-9393.
78. D. Wang, M. Wright, N. K. Elumalai and A. Uddin, *Solar Energy Materials and Solar Cells*, 2016, **147**, 255-275.
79. A. Abate, *Joule*, 2017, **1**, 659-664.
80. A. Babayigit, D. Duy Thanh, A. Ethirajan, J. Manca, M. Muller, H.-G. Boyen and B. Conings, *Scientific Reports*, 2016, **6**, 18721.
81. L. Li, F. Zhang, Y. Hao, Q. Sun, Z. Li, H. Wang, Y. Cui and F. Zhu, *Journal of Materials Chemistry C*, 2017, **5**, 2360-2367.
82. Y. Jiang, H. Zhang, X. Qiu and B. Cao, *Materials Letters*, 2017, **199**, 50-52.
83. X. Qiu, B. Cao, S. Yuan, X. Chen, Z. Qiu, Y. Jiang, Q. Ye, H. Wang, H. Zeng, J. Liu and M. G. Kanatzidis, *Solar Energy Materials and Solar Cells*, 2017, **159**, 227-234.
84. F. Giustino and H. J. Snaith, *ACS Energy Letters*, 2016, DOI: 10.1021/acsenergylett.6b00499, 1233-1240.
85. Y. Liao, H. Liu, W. Zhou, D. Yang, Y. Shang, Z. Shi, B. Li, X. Jiang, L. Zhang, L. N. Quan, R. Quintero-Bermudez, B. R. Sutherland, Q. Mi, E. H. Sargent and Z. Ning, *Journal of the American Chemical Society*, 2017, **139**, 6693-6699.

86. D. H. Cao, C. C. Stoumpos, T. Yokoyama, J. L. Logsdon, T.-B. Song, O. K. Farha, M. R. Wasielewski, J. T. Hupp and M. G. Kanatzidis, *ACS Energy Letters*, 2017, **2**, 982-990.
87. L. R. Morss, M. Siegal, L. Stenger and N. Edelstein, *Inorganic Chemistry*, 1970, **9**, 1771-1775.
88. W. M. A. Smit, G. J. Dirksen and D. J. Stufkens, *Journal of Physics and Chemistry of Solids*, 1990, **51**, 189-196.
89. W. Urland, *Chemical Physics Letters*, 1981, **83**, 116-119.
90. P. Barbier, M. Drache, G. Mairesse and J. Ravez, *Journal of Solid State Chemistry*, 1982, **42**, 130-135.
91. F. Benachenhou, G. Mairesse, G. Nowogrocki and D. Thomas, *Journal of Solid State Chemistry*, 1986, **65**, 13-26.
92. E. T. McClure, M. R. Ball, W. Windl and P. M. Woodward, *Chemistry of Materials*, 2016, **28**, 1348-1354.
93. A. H. Slavney, T. Hu, A. M. Lindenberg and H. I. Karunadasa, *Journal of the American Chemical Society*, 2016, **138**, 2138-2141.
94. G. Volonakis, M. R. Filip, A. A. Haghighirad, N. Sakai, B. Wenger, H. J. Snaith and F. Giustino, *The Journal of Physical Chemistry Letters*, 2016, **7**, 1254-1259.
95. E. Greul, M. Petrus, A. Binek, P. Docampo and T. Bein, *Journal of Materials Chemistry A*, 2017, **5**, 19972-19981.
96. X.-G. Zhao, J.-H. Yang, Y. Fu, D. Yang, Q. Xu, L. Yu, S.-H. Wei and L. Zhang, *Journal of the American Chemical Society*, 2017, **139**, 2630-2638.
97. K. T. Cho, G. Grancini, Y. Lee, E. Oveisi, J. Ryu, O. Almora, M. Tschumi, P. A. Schouwink, G. Seo, S. Heo, J. Park, J. Jang, S. Paek, G. Garcia-Belmonte and M. K. Nazeeruddin, *Energy & Environmental Science*, 2018, DOI: 10.1039/C7EE03513F.
98. T. Singh and T. Miyasaka, *Advanced Energy Materials*, 2018, **8**, 1700677-n/a.
99. C. Laura, K. Samrana, G. Michael and A. Shahzada, *Angewandte Chemie International Edition*, 2016, **55**, 14522-14545.
100. J. Jiménez-López, W. Cambarau, L. Cabau and E. Palomares, *Scientific Reports*, 2017, **7**, 6101.
101. Z. Tang, J. Wang, A. Melianas, Y. Wu, R. Kroon, W. Li, W. Ma, M. R. Andersson, Z. Ma, W. Cai, W. Tress and O. Inganäs, *Journal of Materials Chemistry A*, 2018, **6**, 12574-12581.
102. S. Ravishankar, S. Gharibzadeh, C. Roldán-Carmona, G. Grancini, Y. Lee, M. Ralaiarisoa, A. M. Asiri, N. Koch, J. Bisquert and M. K. Nazeeruddin, *Joule*, 2018, **2**, 788-798.
103. J. M. Frost and A. Walsh, *Accounts of Chemical Research*, 2016, **49**, 528-535.
104. E. Bi, H. Chen, F. Xie, Y. Wu, W. Chen, Y. Su, A. Islam, M. Grätzel, X. Yang and L. Han, *Nature Communications*,

- 2017, **8**, 15330.
105. H.-S. Kim, I.-H. Jang, N. Ahn, M. Choi, A. Guerrero, J. Bisquert and N.-G. Park, *The Journal of Physical Chemistry Letters*, 2015, **6**, 4633-4639.
106. N. Ahn, D.-Y. Son, I.-H. Jang, S. M. Kang, M. Choi and N.-G. Park, *Journal of the American Chemical Society*, 2015, DOI: 10.1021/jacs.5b04930.
107. A. Kojima, K. Teshima, Y. Shirai and T. Miyasaka, *Journal of the American Chemical Society*, 2009, **131**, 6050-6051.
108. L. Etgar, P. Gao, Z. Xue, Q. Peng, A. K. Chandiran, B. Liu, M. K. Nazeeruddin and M. Grätzel, *Journal of the American Chemical Society*, 2012, **134**, 17396-17399.
109. J. Seo, N. J. Jeon, W. S. Yang, H.-W. Shin, T. K. Ahn, J. Lee, J. H. Noh and S. I. Seok, *Advanced Energy Materials*, 2015, **5**.
110. H. Zhou, Q. Chen, G. Li, S. Luo, T.-b. Song, H.-S. Duan, Z. Hong, J. You, Y. Liu and Y. Yang, *Science*, 2014, **345**, 542-546.
111. Q. Chen, H. Zhou, Y. Fang, A. Z. Stieg, T.-B. Song, H.-H. Wang, X. Xu, Y. Liu, S. Lu, J. You, P. Sun, J. McKay, M. S. Goorsky and Y. Yang, *Nat Commun*, 2015, **6**.
112. H. Lee, H. C. Leventis, S.-J. Moon, P. Chen, S. Ito, S. A. Haque, T. Torres, F. Nüesch, T. Geiger, S. M. Zakeeruddin, M. Grätzel and M. K. Nazeeruddin, *Advanced Functional Materials*, 2009, **19**, 2735-2742.
113. L. Martin-Gomis, F. Fernandez-Lazaro and A. Sastre-Santos, *Journal of Materials Chemistry A*, 2014, **2**, 15672-15682.
114. G. Sfyri, C. V. Kumar, G. Sabapathi, L. Giribabu, K. S. Andrikopoulos, E. Stathatos and P. Lianos, *RSC Advances*, 2015, **5**, 69813-69818.
115. W. Ke, D. Zhao, C. R. Grice, A. J. Cimaroli, G. Fang and Y. Yan, *Journal of Materials Chemistry A*, 2015, **3**, 23888-23894.
116. F. Javier Ramos, M. Ince, M. Urbani, A. Abate, M. Grätzel, S. Ahmad, T. Torres and M. K. Nazeeruddin, *Dalton Transactions*, 2015, **44**, 10847-10851.
117. L. Yang, L. Guo, Q. Chen, H. Sun, H. Yan, Q. Zeng, X. Zhang, X. Pan and S. Dai, *Journal of Molecular Graphics and Modelling*, 2012, **38**, 82-89.
118. C. Linares-Flores, F. Mendizabal, R. Arratia-Pérez, N. Inostroza and C. Orellana, *Chemical Physics Letters*, 2015, **639**, 172-177.
119. D. González-Rodríguez and T. Torres, *European Journal of Organic Chemistry*, 2009, **2009**, 1871-1879.
120. D. Maiti, B. P. Fors, J. L. Henderson, Y. Nakamura and S. L. Buchwald, *Chemical Science*, 2011, **2**, 57-68.
121. N. J. Jeon, J. H. Noh, Y. C. Kim, W. S. Yang, S. Ryu and S. I. Seok, *Nat Mater*, 2014, **13**, 897-903.
122. D.-Y. Son, J.-W. Lee, Y. J. Choi, I.-H.

- Jang, S. Lee, P. J. Yoo, H. Shin, N. Ahn, M. Choi, D. Kim and N.-G. Park, *Nature Energy*, 2016, **1**, 16081.
123. H.-S. Kim, C.-R. Lee, J.-H. Im, K.-B. Lee, T. Moehl, A. Marchioro, S.-J. Moon, R. Humphry-Baker, J.-H. Yum, J. E. Moser, M. Gratzel and N.-G. Park, *Sci. Rep.*, 2012, **2**.
124. P. Gao, M. Gratzel and M. K. Nazeeruddin, *Energy & Environmental Science*, 2014, **7**, 2448-2463.
125. M. Saliba, S. Orlandi, T. Matsui, S. Aghazada, M. Cavazzini, J.-P. Correa-Baena, P. Gao, R. Scopelliti, E. Mosconi, K.-H. Dahmen, F. De Angelis, A. Abate, A. Hagfeldt, G. Pozzi, M. Graetzel and M. K. Nazeeruddin, *Nature Energy*, 2016, **1**, 15017.
126. M. Saliba, T. Matsui, J.-Y. Seo, K. Domanski, J.-P. Correa-Baena, M. K. Nazeeruddin, S. M. Zakeeruddin, W. Tress, A. Abate, A. Hagfeldt and M. Gratzel, *Energy & Environmental Science*, 2016, DOI: 10.1039/C5EE03874J.
127. M. M. Lee, J. Teuscher, T. Miyasaka, T. N. Murakami and H. J. Snaith, *Science*, 2012, **338**, 643-647.
128. G. Yang, H. Tao, P. Qin, W. Ke and G. Fang, *Journal of Materials Chemistry A*, 2016, **4**, 3970-3990.
129. W. S. Yang, J. H. Noh, N. J. Jeon, Y. C. Kim, S. Ryu, J. Seo and S. I. Seok, *Science*, 2015, **348**, 1234-1237.
130. *Journal of Applied Physics*, 2016, **119**, 145502.
131. O. Langmar, C. R. Ganivet, A. Lennert, R. D. Costa, G. de la Torre, T. Torres and D. M. Guldi, *Angewandte Chemie International Edition*, 2015, **54**, 7688-7692.
132. M.-E. Ragoussi, J.-J. Cid, J.-H. Yum, G. de la Torre, D. DiCenso, M. Grätzel, M. K. Nazeeruddin and T. Torres, *Angewandte Chemie International Edition*, 2012, **51**, 4375-4378.
133. M.-E. Ragoussi, J.-H. Yum, A. K. Chandiran, M. Ince, G. de la Torre, M. Grätzel, M. K. Nazeeruddin and T. Torres, *ChemPhysChem*, 2014, **15**, 1033-1036.
134. G. de la Torre, G. Bottari, M. Sekita, A. Hausmann, D. M. Guldi and T. Torres, *Chemical Society Reviews*, 2013, **42**, 8049-8105.
135. G. Bottari, G. de la Torre, D. M. Guldi and T. Torres, *Chemical Reviews*, 2010, **110**, 6768-6816.
136. L. Sosa-Vargas, F. Nekelson, D. Okuda, M. Takahashi, Y. Matsuda, Q.-D. Dao, Y. Hiroyuki, A. Fujii, M. Ozaki and Y. Shimizu, *Journal of Materials Chemistry C*, 2015, **3**, 1757-1765.
137. K. B. Ørnsø, J. M. Garcia-Lastra, G. De La Torre, F. J. Himpsel, A. Rubio and K. S. Thygesen, *Chemical Science*, 2015, **6**, 3018-3025.
138. H. Ali, N. Cauchon and J. E. van Lier, *Photochemical & Photobiological Sciences*, 2009, **8**, 868-874.
139. P. Gao, K. T. Cho, A. Abate, G. Grancini, P. Y. Reddy, M. Srivasu, M.

- Adachi, A. Suzuki, K. Tsuchimoto, M. Grätzel and M. K. Nazeeruddin, *Physical Chemistry Chemical Physics*, 2016, **18**, 27083-27089.
140. A. W. Snow, in *The Porphyrin Handbook*, eds. K. M. Kadish, K. M. Smith and R. Guilard, Academic Press, Amsterdam, 2003, pp. 129-176.
141. J. P. Correa Baena, L. Steier, W. Tress, M. Saliba, S. Neutzner, T. Matsui, F. Giordano, T. J. Jacobsson, A. R. Srimath Kandada, S. M. Zakeeruddin, A. Petrozza, A. Abate, M. K. Nazeeruddin, M. Grätzel and A. Hagfeldt, *Energy & Environmental Science*, 2015, DOI: 10.1039/C5EE02608C.
142. S. Kazim, M. K. Nazeeruddin, M. Grätzel and S. Ahmad, *Angewandte Chemie International Edition*, 2014, **53**, 2812-2824.
143. A. C. Cruickshank, C. J. Dotzler, S. Din, S. Heutz, M. F. Toney and M. P. Ryan, *Journal of the American Chemical Society*, 2012, **134**, 14302-14305.
144. P. Gargiani, A. Calabrese, C. Mariani and M. G. Betti, *The Journal of Physical Chemistry C*, 2010, **114**, 12258-12264.
145. W. J. Pietro, T. J. Marks and M. A. Ratner, *Journal of the American Chemical Society*, 1985, **107**, 5387-5391.
146. P. Gratia, A. Magomedov, T. Malinauskas, M. Daskeviciene, A. Abate, S. Ahmad, M. Grätzel, V. Getautis and M. K. Nazeeruddin, *Angewandte Chemie International Edition*, 2015, **54**, 11409-11413.
147. K. S. Novoselov, A. K. Geim, S. V. Morozov, D. Jiang, Y. Zhang, S. V. Dubonos, I. V. Grigorieva and A. A. Firsov, *Science*, 2004, **306**, 666-669.
148. H.-X. Wang, Q. Wang, K.-G. Zhou and H.-L. Zhang, *Small*, 2013, **9**, 1266-1283.
149. T.-F. Yeh, C.-Y. Teng, L.-C. Chen, S.-J. Chen and H. Teng, *Journal of Materials Chemistry A*, 2016, **4**, 2014-2048.
150. Z. Chen, W. Ren, L. Gao, B. Liu, S. Pei and H.-M. Cheng, *Nat Mater*, 2011, **10**, 424-428.
151. S. Park and R. S. Ruoff, *Nat Nanotechnol*, 2009, **4**, 217-224.
152. Z. Yin, J. Zhu, Q. He, X. Cao, C. Tan, H. Chen, Q. Yan and H. Zhang, *Advanced Energy Materials*, 2013, **4**.
153. N. Balis, E. Stratakis and E. Kymakis, *Materials Today*, DOI: <http://dx.doi.org/10.1016/j.mattod.2016.03.018>.
154. J. T.-W. Wang, J. M. Ball, E. M. Barea, A. Abate, J. A. Alexander-Webber, J. Huang, M. Saliba, I. Mora-Sero, J. Bisquert, H. J. Snaith and R. J. Nicholas, *Nano Letters*, 2013, **14**, 724-730.
155. W. Li, H. Dong, X. Guo, N. Li, J. Li, G. Niu and L. Wang, *Journal of Materials Chemistry A*, 2014, **2**, 20105-20111.
156. G. S. Han, Y. H. Song, Y. U. Jin, J.-W.

- Lee, N.-G. Park, B. K. Kang, J.-K. Lee, I. S. Cho, D. H. Yoon and H. S. Jung, *ACS Applied Materials & Interfaces*, 2015, **7**, 23521-23526.
157. M. Batmunkh, C. J. Shearer, M. J. Biggs and J. G. Shapter, *Journal of Materials Chemistry A*, 2016, **4**, 2605-2616.
158. J.-S. Yeo, R. Kang, S. Lee, Y.-J. Jeon, N. Myoung, C.-L. Lee, D.-Y. Kim, J.-M. Yun, Y.-H. Seo, S.-S. Kim and S.-I. Na, *Nano Energy*, 2015, **12**, 96-104.
159. E. Stratakis, K. Savva, D. Konios, C. Petridis and E. Kymakis, *Nanoscale*, 2014, **6**, 6925-6931.
160. D. Konios, G. Kakavelakis, C. Petridis, K. Savva, E. Stratakis and E. Kymakis, *Journal of Materials Chemistry A*, 2016, **4**, 1612-1623.
161. G. Kakavelakis, D. Konios, E. Stratakis and E. Kymakis, *Chemistry of Materials*, 2014, **26**, 5988-5993.
162. A. Agresti, S. Pescetelli, L. Cinà, D. Konios, G. Kakavelakis, E. Kymakis and A. D. Carlo, *Advanced Functional Materials*, 2016, DOI: 10.1002/adfm.201504949, 2686-2694.
163. K. Aitola, K. Sveinbjornsson, J. P. Correa-Baena, A. Kaskela, A. Abate, Y. Tian, E. M. J. Johansson, M. Gratzel, E. I. Kauppinen, A. Hagfeldt and G. Boschloo, *Energy & Environmental Science*, 2016, **9**, 461-466.
164. M. Acik and S. B. Darling, *Journal of Materials Chemistry A*, 2016, DOI: 10.1039/C5TA09911K.
165. M. Hadadian, J.-P. Correa-Baena, E. K. Goharshadi, A. Ummadisingu, J.-Y. Seo, J. Luo, S. Gholipour, S. M. Zakeeruddin, M. Saliba, A. Abate, M. Grätzel and A. Hagfeldt, *Advanced Materials*, 2016, DOI: 10.1002/adma.201602785, n/a-n/a.
166. J. H. Heo, M. S. You, M. H. Chang, W. Yin, T. K. Ahn, S.-J. Lee, S.-J. Sung, D. H. Kim and S. H. Im, *Nano Energy*, 2015, **15**, 530-539.
167. S. D. Stranks, G. E. Eperon, G. Grancini, C. Menelaou, M. J. P. Alcocer, T. Leijtens, L. M. Herz, A. Petrozza and H. J. Snaith, *Science*, 2013, **342**, 341-344.

Curriculum Vitae

Kyung Taek Cho

ÉCOLE POLYTECHNIQUE FÉDÉRALE DE LAUSANNE (EPFL),

Rue de l'Industrie 17, Sion, 1950, Valais, Switzerland.

+41 78 786 67 46

kyungtaek.cho@epfl.ch or <https://www.linkedin.com/in/kyungtaek-cho-111225149/>

EDUCATION

2014.8 - present

Ph.D candidate

ÉCOLE POLYTECHNIQUE FÉDÉRALE DE LAUSANNE (EPFL), Switzerland

Doctoral Program in Chemistry and Chemical Engineering

Thesis: Composition and Interface Engineering of Organic-Inorganic Hybrid Perovskites to Improve Photovoltaic Performance and Stability

2012.9 - 2014.6

Master of Chemical and Biomolecular Engineering

Korea Advanced Institute of Science and Technology (KAIST), KOREA

Thesis: Developing methodology for heteroatoms doped porous carbons using polymers and graphene for high-performance electrode of supercapacitors.

2006.2 - 2012.8

Bachelor of Chemical Engineering

Hanyang University, KOREA

Graduated *Summa Cum Laude*

AWARDS or Scholarship

Top scholarships 2006, 2010 Hanyang University

Honor scholarships 2007, 2011, 2012 Hanyang University,

PUBLICATIONS

Research information (Google scholar)

https://scholar.google.com/citations?hl=en&user=9mx9ZlgAAAAJ&view_op=list_works&sortby=pubdate

A. As the 1st author

- 1) Kyung Taek Cho, Yi Zhang, Simonetta Orlandi, Marco Cavazzini, Iwan Zimmermann, Andreas Lesch, Nouar Tabet, Gianluca Pozzi, Giulia Grancini and Mohammad Khaja Nazeeruddin. **A water repellent low dimensional fluorinated perovskite as interfacial coating for 20% efficient solar cells.** Nano letter, 2018.

- 2) Martina Pantaler, Kyung Taek Cho, Valentin I. E. Queloz, Inés GarcíaBenito, Christian Fettkenhauer, Irina Anusca, Mohammad K. Nazeeruddin, Doru C. Lupascu, Giulia Grancini. **Hysteresis-Free Lead-Free Double Perovskite Solar Cells by Interface Engineering** *ACS Energy Letters*. 2018
- 3) Kyung Taek Cho, Giulia Grancini, Yonghui Lee, Emad Oveisi, Jaehoon Ryu, Osbel Almora, Manuel Tschumi, Pascal Alexander Schouwink, Gabseok Seo, Sung Heo, Jucheol Park, Jyongsik Jang, Sanghyun Paek, Germà Garcia-Belmonte, Mohammad Khaja Nazeeruddina **Selective growth of layered perovskite for stable and efficient photovoltaics** *Energy & Environmental Science*, 2018.
- 4) Kyung Taek Cho, Sanghyun Paek, Giulia Grancini, Cristina Roldán-Carmona, Peng Gao, Yonghui Lee, Mohammad Khaja Nazeeruddin **Highly efficient perovskite solar cells with a compositionally engineered perovskite/hole transporting material interface** *Energy & Environmental Science*, 2017
- 5) Kyung Teak Cho, Olga Trukhina, Cristina Roldán-Carmona, Mine Ince, Paul Gratia, Giulia Grancini, Peng Gao, *et al.* **Molecularly engineered phthalocyanines as hole-transporting materials in perovskite solar cells reaching power conversion efficiency of 17.5%**. *Advanced Energy Materials*, 2017.
- 6) Kyung Teak Cho, Grancini G, Lee Y, Konios D, Paek S, Kymakis E, *et al.* **Beneficial Role of Reduced Graphene Oxide for Electron Extraction in Highly Efficient Perovskite Solar Cells.** *ChemSusChem*, 2016.
- 7) Kyung Teak Cho, Rakstys K, Cavazzini M, Orlandi S, Pozzi G, Nazeeruddin MK. **Perovskite Solar Cells Employing Molecularly Engineered Zn(II) Phthalocyanines as Hole-transporting Materials.** *Nano Energy*, 2016.
- 8) Kyung Taek Cho, Sang Bok Lee and Jae W Lee **Facile Synthesis of Highly Electrocapacitive Nitrogen-doped Graphitic Porous Carbons**, *The Journal of Physical Chemistry C, The Journal of Physical Chemistry C*, 2014.

B. As a next author

- 1) Hyo Joong Lee, Kyung Taek Cho, Sanghyun Paek, Yonghui Lee, Aron J Huckaba, Valentin IE Queloz, Iwan Zimmermann, Giulia Grancini, *et al.* **A Facile Preparative Route of Nanoscale Perovskites over Mesoporous Metal Oxide Films and Their Applications to Photosensitizers and Light Emitters** *Advanced Functional Materials* 2018
- 2) Yi Zhang, Sanghyun Paek, Maxence Urbani, María Medel, Iwan Zimmermann, Kyung Taek Cho, Mine Ince, Mohammad Khaja Nazeeruddin, Tomás Torres **Unsymmetrical and Symmetrical Zn**

(II) Phthalocyanines as Hole-Transporting Materials for Perovskite Solar Cells ACS Applied Energy Materials 2018

- 3) Yonghui Lee, Seunghwan Lee, Gabseok Seo, Sanghyun Paek, Kyung Taek Cho, *et al.* **Efficient Planar Perovskite Solar Cells Using Passivated Tin Oxide as an Electron Transport Layer.** Advanced Science, 2018
- 4) N ria F Montcada, Maria M ndez, Kyung Taek Cho, Mohammad Khaja Nazeeruddin, Emilio Palomares **Photo-induced dynamic processes in perovskite solar cells: the influence of perovskite composition in the charge extraction and the carrier recombination** Nanoscale, 2018
- 5) Osbel Almora, Kyung Taek Cho, Sadig Aghazada, Iwan Zimmermann, Gebhard J Matt, Christoph J Brabec, Mohammad Khaja Nazeeruddin, Germ  Garcia-Belmonte **Discerning recombination mechanisms and ideality factors through impedance analysis of high-efficiency perovskite solar cells** Nano Energy, 2018
- 6) Aron J Huckaba, Maryline Ralaizarisoa, Kyung Taek Cho, Emad Oveisi, Norbert Koch, Mohammad Khaja Nazeeruddin, **Intercalation makes the difference with TiS 2: Boosting electrocatalytic water oxidation activity through Co intercalation** Journal of Materials Research, 2017
- 7) Giulia Grancini, Daniele Viola, Yonghui Lee, Michael Saliba, Sanghyun Paek, Kyung Taek Cho *et al.*, **Femtosecond Charge Injection Dynamics at Hybrid Perovskite Interfaces** ChemPhysChem, 2017
- 8) Sanghyun Paek, Peng Qin, Yonghui Lee, Kyung Taek Cho, *et al.* **Dopant-Free Hole-Transporting Materials for Stable and Efficient Perovskite Solar Cells** Advanced Materials, 2017
- 9) S Paek, P Schouwink, E Nefeli Athanasopoulou, KT Cho, G Grancini, Y Lee, Y Zhang, F Stellacci, Mohammad Khaja Nazeeruddin, P Gao. **From Nano-to Micrometer Scale: The Role of Antisolvent Treatment on High Performance Perovskite Solar Cells** Chemistry of Materials, 2017
- 10) Maryte Daskeviciene, Sanghyun Paek, Zhiping Wang, Tadas Malinauskas, Gabriele Jokubauskaite, Kasparas Rakstys, Kyung Taek Cho et al. **Carbazole-based enamine: Low-cost and efficient hole transporting material for perovskite solar cells**, Nano Energy, 2017
- 11) Yong Hui Lee, Sanghyun Paek, Kyung Taek Cho, Emad Oveisi, Peng Gao *et al.* **Enhanced charge collection with passivation of the tin oxide layer in planar perovskite solar cells** Journal of Materials Chemistry A, 2017
- 12) Kasparas Rakstys, Sanghyun Paek, Peng Gao, Paul Gratia, Tomasz Marszalek, Giulia Grancini, Kyung Taek Cho, Kristijonas Genevicius, Vygintas Jankauskas, Wojciech Pisula, Mohammad Khaja Nazeeruddin. **Molecular engineering of face-on oriented dopant-free hole transporting material**

for perovskite solar cells with 19% PCE Journal of Materials Chemistry A, 2017

- 13) Nria F Montcada, Jos Manuel Marn-Beloqui, Werther Cambarau, Jess Jimnez-Lpez, Lydia Cabau, Kyung Taek Cho, Mohammad Khaja Nazeeruddin, Emilio Palomares **Analysis of Photoinduced Carrier Recombination Kinetics in Flat and Mesoporous Lead Perovskite Solar Cells**. ACS Energy Letters, 2016
- 14) Kasparas Rakstys, Sanghyun Paek, Muhammad Sohail, Peng Gao, Kyung Taek Cho, *et al.* **A highly hindered bithiophene-functionalized dispiro-oxepine derivative as an efficient hole transporting material for perovskite solar cells**. Journal of Materials Chemistry A, 2016
- 15) Huckaba AJ, Sanghyun P, Grancini G, Bastola E, Taek CK, Younghui L, Cho KT, *et al.* **Exceedingly Cheap Perovskite Solar Cells Using Iron Pyrite Hole Transport Materials**. *ChemistrySelect*, 2016, **1**(16): 5316-5319.
- 16) Gao P, Cho KT, Abate A, Grancini G, Reddy PY, Srivasu M, *et al.* **An efficient perovskite solar cell with symmetrical Zn(ii) phthalocyanine infiltrated buffering porous Al₂O₃ as the hybrid interfacial hole-transporting layer**. *Physical Chemistry Chemical Physics*, 2016, **18**(39): 27083-27089.
- 17) Lee YH, Luo J, Son M-K, Gao P, Cho KT, Seo J, *et al.* **Enhanced Charge Collection with Passivation Layers in Perovskite Solar Cells**. *Advanced Materials*, 2016, **28**(20): 3966-3972.

Conference and Seminal Presentations

1. Kyung Taek Cho and Jae W Lee (2013), Oral presentation, WCCE9 & APCCHE 2013 (9th World Congress of Chemical Engineering incorporating 15th Asian Pacific Confederation of Chemical Engineering Congress, August 18-23, 2013, Seoul, Korea, "Transformation of CO₂ to Boron-doped Porous Carbons".
2. Kyung Taek Cho, Grancini Giulia, and Mohammad Khaja Nazeeruddin, Postal presentation, Hybrid & Organic Photovoltaics 2017, Lausanne, Switzerland, "Highly efficient perovskite solar cells with a compositionally engineered perovskite/hole transporting material interface"
3. Kyung Taek Cho, Grancini Giulia, and Mohammad Khaja Nazeeruddin, Postal presentation, Materials Research Society 2017, Boston, USA, "Highly Efficient and Stable Perovskite Solar Cells via Engineering the Interface Perovskite/Hole Transporting Material"

RESEARCH EXPERIENCE

2012.9 – 2014.7 KAIST, Department of Chemical and Biomolecular Engineering

Advisor: Jae Woo Lee

- Developed and constructed experimental technique to porous carbons with high specific surface area and heteroatoms-doped graphene.
- Analyzed the elements, specific surface area, and the morphology of samples.

- Determined the capacitance of the samples and estimated the effect of heteroatoms doped into carbons.
- Performed the electrochemical experiment.

2014.8 – present **EPFL, Doctoral Program in Chemistry and Chemical Engineering**

Advisor: Mohammad Khaja Nazeeruddin

- Developed and constructed experimental technique to homogeneous dense films on substrates.
- Analyzed the morphology and the elements of films.
- Performed the solar cells experiment and found the improvement.
- Determined the solvent effect on uniform films and the elements effect on forming perovskite structure.

TECHNICAL SKILLS

Instruments

Scanning electron microscope (SEM), Raman, Powder X-ray Diffraction, Furnace, Electro- chemical measurements, control of glovebox, X-ray photoelectron spectroscopy, Surface characterization (BET specific surface area and pore size distribution).

Others

3D MAX, Microsoft office, Origin Pro, etc.

EXTRACURRICULAR ACTIVITIES

Military Service as a Medic, Korea 2007.7 ~ 2009.6

Voluntary, tutoring foreigner students in Hanyang University 2010.3 ~ 2010.8